IAEA-TECDOC-1466

Physics and technology of inertial fusion energy targets, chambers and drivers

Proceedings of a technical meeting held in Daejon, Republic of Korea, 11–13 October 2004

IAEA
International Atomic Energy Agency

September 2005

IAEA-TECDOC-1466

Physics and technology of inertial fusion energy targets, chambers and drivers

Proceedings of a technical meeting held in Daejon, Republic of Korea, 11–13 October 2004

IAEA
International Atomic Energy Agency

September 2005

The originating Section of this publication in the IAEA was:

Physics Section
International Atomic Energy Agency
Wagramer Strasse 5
P.O. Box 100
A-1400 Vienna, Austria

PHYSICS AND TECHNOLOGY OF INERTIAL FUSION ENERGY TARGETS,
CHAMBERS AND DRIVERS
IAEA, VIENNA, 2005
IAEA-TECDOC-1466
ISBN 92–0–108405–6
ISSN 1011–4289

Printed by the IAEA in Austria
September 2005

FOREWORD

The third IAEA Technical Meeting on Physics and Technology of Inertial Fusion Energy Targets and Chambers took place 11–13 October 2004 in the Yousung Hotel Daejon, Republic of Korea. The first meeting was held in Madrid, Spain, 7–9 June 2000, and the second one in San Diego, California, 17–19 June 2002.

Nuclear fusion has the promise of becoming an abundant energy source with good environmental compatibility. Excellent progress has been made in controlled nuclear fusion research on both magnetic and inertial approaches for plasma confinement. The IAEA plays a pro-active role to catalyze innovation and enhance worldwide commitment to fusion. This is done by creating awareness of the different concepts of magnetic as well as inertial confinement. The International Fusion Research Council (IFRC) supports the IAEA in the development of strategies to enhance fusion research in Member States. As part of the recommendations, a technical meeting on the physics and technology of inertial fusion energy (IFE) was proposed in one of the council meetings.

The objective of the technical meeting was to contribute to advancing the understanding of targets and chambers for all proposed inertial fusion energy power plant designs. The topics to be covered were: Target design and physics, chamber design and physics, target fabrication injection and Tritium handling, assessment of safety, environment and economy aspect of IFE. It was recognized by the International Advisory Committee that the scope of the meeting should also include fusion drivers. The presentations of the meeting included target and chamber physics and technology for all proposed IFE plant concepts (laser driven, heavy-ion driven, Z-pinches, etc.). The final Research Coordination Meeting of the Coordinated Research Project on Elements of Power Plant Design for Inertial Fusion Energy, including further new results and achievements, followed the technical meeting.

Twenty-nine participants from 12 countries participated in this meeting. Twenty-four presentations on the topics of plant design, drivers, targets and chambers were given. The topic of drivers, including heavy ion drivers, has been added to the outline of the programme. Five presentations were given on this topic. One of these presentations was accepted and presented as an overview paper during the 20th Fusion Energy Conference in Vilamoura, Portugal.

The International Advisory Committee consisted of S. Nakai, T. Norimatsu, E. Koresheva, W. Meier, J.M. Perlado, R. Khardekar, P. Joyer, and H.J. Kong. Acknowledgements should be directed to the local organizer, H.-J. Kong, who ensured that the technical work was supported by great hospitality.

The IAEA officer responsible for the preparation of this publication was G. Mank of the Division of Physical and Chemical Sciences.

EDITORIAL NOTE

The papers in these proceedings are reproduced as submitted by the authors and have not undergone rigorous editorial review by the IAEA.

The views expressed do not necessarily reflect those of the IAEA, the governments of the nominating Member States or the nominating organizations.

The use of particular designations of countries or territories does not imply any judgement by the publisher, the IAEA, as to the legal status of such countries or territories, of their authorities and institutions or of the delimitation of their boundaries.

The mention of names of specific companies or products (whether or not indicated as registered) does not imply any intention to infringe proprietary rights, nor should it be construed as an endorsement or recommendation on the part of the IAEA.

The authors are responsible for having obtained the necessary permission for the IAEA to reproduce, translate or use material from sources already protected by copyrights.

CONTENTS

TARGET, FABRICATION

CHAMBER

SUMMARY

It is expected that new megajoule laser facilities which are under construction in the US and France will demonstrate fusion ignition and burn, and, around 2010~2015, gain of energy. This will be an epoch-making achievement in the history of fusion energy development, which will give us the real means to solve the future energy and environmental problems of the world.

Now the strategic approach toward the final goal, namely fusion energy production on a commercial basis, is required. An inertial fusion energy (IFE) power plant and its development are based on a large number of advanced concepts and technologies, such as drivers, target fabrication and injection, reaction chamber, and remaining system.

The separability of IFE power plant systems means that these concepts and technologies can be developed somewhat independently and later assembled to form a system. Therefore, worldwide efforts in IFE research and engineering development could be organized to be very effective, provided that sharing of information is timely and complete. The contribution and auspices of IAEA in organizing the IAEA-TM (before TCM: Technical Committee Meeting) on IFE-related topics have worked effectively in gathering the scientific and technical informations on IFE and in coordinating the worldwide collaboration.

The outline of the issues which have been discussed at the Third IAEA-TM on Physics and Technology of Initial Fusion Energy Target, Chamber, and Driver are summarized as follows:

1. The progress of the Z-pinch IFE and a new concept of power plant for fast ignition heavy ion fusion have been reported and discussed with much attention. The efforts at the Instituto de Fusión Nuclear - Universidad Politécnica de Madrid (DENIM) on the IFE modeling include safety and environmental issues of IFE together with the target and chamber dynamics. It presents new challenges toward the real evaluation of IFE power plant.
2. The Diode Pumped Solid State Laser (DPSSL) is becoming the most feasible candidate as IFE driver for a power plant. Two most advanced programmes, Mercury at Lawrence Livermore National Laboratory (LLNL) and high average power laser for nuclear fusion application (HALNA) at the Institute of Laser Engineering (ILE) at Osaka University, have been reported and discussed. Multi-beam combining with stimulated Brillouin scattering (SBS) phase conjugation is an essential technique to form a large laser IFE driver with well-configured elemental modules. Excellent results at the Korea Advanced Institute of Science & Technology (KAIST) on this technique have been reported and showed the possibility of practical use of this technology.
3. Interaction physics is still an important issue for improving the target design aiming at more efficient and robust implosion with higher gain, and also for developing an advanced concept such as fast ignition. Many interesting and meaningful results came from GSI-Darmstadt on Intense Heavy Ion and Laser Beams interaction and the Vinca Institute of Nuclear Science in Belgrade. The Institute of Plasma Physics and Laser Micro Fusion in Warsaw and the Czech Technical University in Prague, both of which are investigating the fundamental process of the new field on high energy density physics, have reported on the interaction of intense short pulse laser with plasmas. The hydrodynamic instability problem is an essential issue in designing the efficient implosion of fusion pellet. Theoretical investigation and an advanced concept to stabilize the surface instability have been presented by the National Research Institute for Applied Mathematics (NRIAM) in Bangalore, India.

4. Target fabrication and injection have been discussed mainly focusing on the technical aspect of the repetitive operation, which is essential for a power plant.
5. Chamber wall response against high flux pulsed energy, and chamber dynamics and clearing study are key issues in designing the IFE reaction chamber. Material studies on SiC and PbMg by using a laser mass-spectrometer were reported from Scientific-Research of Applied Physics at the National University of Uzbekistan. Intensive research works on chamber wall ablation and on chamber clearing were reported from the Technical Institute of Tokyo and UCLA respectively.

Finally it can be concluded that the IAEA-TM on specific topics has been very effective for the promotion of the worldwide activity on IFE-related research and development because of the openness of the discussion and the timeliness of the issues in the process of fusion energy development.

POWER PLANT DESIGN

Progress on Z-pinch inertial fusion energy*

C.L. Olson, The Z-Pinch IFE Team**
Sandia National Laboratories, Albuquerque, New Mexico, United States of America

Abstract. The long-range goal of the Z-Pinch IFE programme is to produce an economically attractive power plant using high-yield z-pinch-driven targets (~3 GJ) with low rep-rate per chamber (~0.1 Hz). The present mainline choice for a Z-Pinch IFE power plant uses an LTD (Linear Transformer Driver) repetitive pulsed power driver, a Recyclable Transmission Line (RTL), a dynamic hohlraum z-pinch-driven target, and a thick-liquid wall chamber. The RTL connects the pulsed power driver directly to the z-pinch-driven target, and is made from frozen coolant or a material that is easily separable from the coolant (such as carbon steel). The RTL is destroyed by the fusion explosion, but the RTL materials are recycled, and a new RTL is inserted on each shot. The RTL concept eliminates the problems of a final optic, high-speed target injection, and pointing and tracking N beams (N~100). Instead, the RTL concept must be shown to be feasible and economically attractive. Results of z-pinch IFE studies over the last three years are discussed, including RTL experiments at the 10 MA level on Saturn, RTL structural studies, RTL manufacturing/cost studies, RTL activation analysis, power plant studies, high-yield IFE target studies, etc. Recent funding by a U.S. Congressional initiative of $4M for FY04 is supporting research on (1) RTLs, (2) repetitive pulsed power drivers, (3) shock mitigation [because of the high-yield targets], (4) planning for a proof-of-principle full RTL cycle demonstration [with a 1 MA, 1 MV, 100 ns, 0.1 Hz driver], (5) IFE target studies for multi-GJ yield targets, and (6) z-pinch IFE power plant engineering and technology development.

1. Introduction

Z-Pinch Inertial Fusion Energy (IFE) extends the single-shot z-pinch inertial confinement fusion results on Z to a repetitive basis with high-yield fusion targets for the purpose of producing an attractive and economical power plant [1]. Z-Pinch IFE is relatively new, and has become part of the IFE community over the last five years. Z-Pinch IFE has been part of the 1999 Snowmass Fusion Summer Study, the IAEA Cooperative Research Project on IFE Power Plants, the 2002 Snowmass Fusion Summer Study, the FESAC 35-year Plan Panel (2003) [2], and the FESAC IFE Panel (2004) [3].

Z-Pinch IFE has an attractive potential based on what has already been accomplished with pulsed power driven z-pinches:

---

* Sandia is a multiprogramme laboratory operated by Sandia Corporation, a Lockheed Martin Company, for the U.S. Dept. of Energy under contract No. DE-AC04-94AL85000.

** G. Rochau, S. Slutz, C. Morrow, R. Olson, A. Parker, M. Cuneo, D. Hanson, G. Bennett, T. Sanford, J. Bailey, W. Stygar, R. Vesey, T. Mehlhorn, K. Struve, M. Mazarakis, M. Savage, A. Owen, T. Pointon, M. Kiefer, S. Rosenthal, L. Schneider, S. Glover, K. Reed, G. Benevides, D. Schroen, W. Krych, C. Farnum, M. Modesto, D. Oscar, L. Chhabildas, J. Boyes, V. Vigil, R. Keith, M. Turgeon, B. Smith, B. Cipiti, E. Lindgren, D. Smith, K. Peterson, V. Dandini, D. McDaniel, J. Quintenz, M. Matzen, J.P. VanDevender, W. Gauster, L. Shephard, M. Walck, T. Renk, T. Tanaka, M. Ulrickson, P. Peterson, J. De Groot, N. Jensen, R. Peterson, G. Pollock, P. Ottinger, J. Schumer, D. Kammer, I. Golovkin, G. Kulcinski, L. El-Guebaly, G. Moses, E. Mogahed, I. Sviatoslavsky, M. Sawan, M. Anderson, R. Gallix, N. Alexander, W. Rickman, H. Tran, P. Panchuk, W. Meier, J. Latkowski, R. Moir, R. Schmitt, R. Abbot, M. Abdou, A. Ying, P. Calderoni, N. Morley, S. Abdel-Khalik, D. Welch, D. Rose, W. Szaroletta, R. Curry, K. McDonald, D. Louie, S. Dean, A. Kim, S. Nedoseev, E. Grabovsky, A. Kingsep, V. Smirnov.

- 1.8 MJ of x-rays are routinely produced on Z
- pulsed power has low demonstrated cost (~$30/J)
- pulsed power drivers have high efficiency –15% for wall plug to x-rays on Z, and this can be optimized to an even higher value
- capsule compression ratios of 14–21 have been achieved with the double-pinch target, and up to 8×0^{10} DD neutrons have been demonstrated with the dynamic hohlraum target — this is almost an order of magnitude larger than that demonstrated with any other indirect-drive target with any other driver
- repetitive pulsed power using RHEPP magnetic switching technology has been demonstrated at 2.5 kJ @ 120 Hz (300 kW average power)

In the following, the Z-Pinch IFE system is described, the Recyclable Transmission Line (RTL) concept is discussed, and the status of current research is presented.

2. Z-Pinch IFE concept

The goal of Z-Pinch Inertial Fusion Energy (IFE) is to produce an economically attractive power plant using a repetitive pulsed power driver and z-pinch-driven fusion targets. While many schemes have been proposed [1], the most enduring appears to use the Recyclable Transmission Line (RTL) concept [4], in which an RTL connects the repetitive driver directly to the target, and the fusion explosions are contained in a thick-liquid wall chamber. A unique feature is that high-yield fusion targets (~3GJ) would be used at the low rep-rate of 0.1 Hz per chamber. The matrix of choices available for a Z-Pinch IFE power plant is summarized in Figure 1.

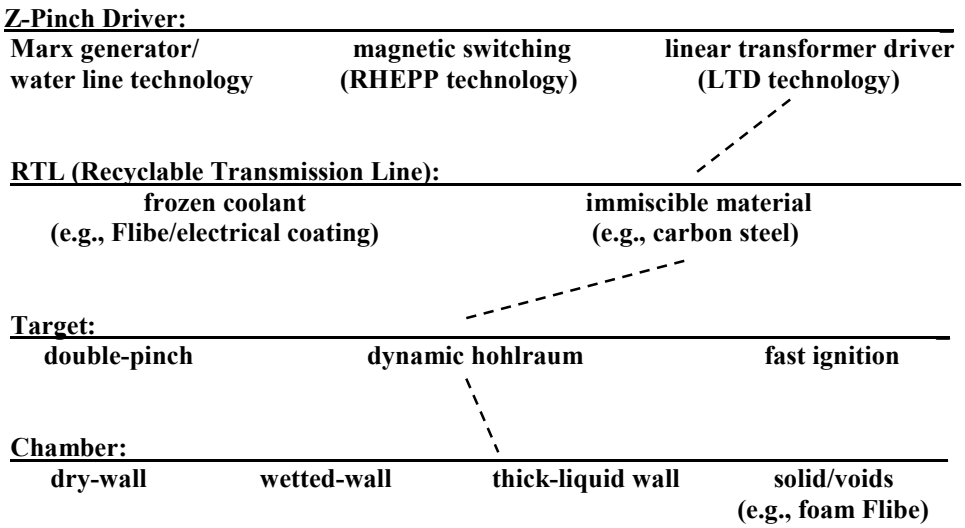

Figure 1. Z-Pinch IFE Power Plant – matrix of choices (dashed line shows preferred choices).

Note that several options are available for each part of the power plant – the driver, the RTL, the target, and the chamber type:

- Three possible repetitive driver technologies include Marx generator/water line technology, RHEPP magnetic switching technology, and Linear Transformer Driver

(LTD) voltage-adder technology. The LTD approach is compact, requires no oil or water storage tanks, and is the present preferred choice for z-pinch IFE.
- The RTL can be made of frozen coolant (e.g., Flibe) or a material that is immiscible in the coolant (e.g., carbon steel). The latter is the present preferred choice for z-pinch IFE.
- Of several z-pinch target options (double-pinch, dynamic hohlraum, fast ignition, etc.), the dynamic hohlraum target is the present preferred choice for z-pinch IFE.
- The chamber may be dry-wall, wetted-wall, thick-liquid wall, or solid/voids (e.g., foam Flibe). The thick-liquid wall chamber is the preferred chamber for z-pinch IFE.

3. Recyclable Transmission Line (RTL)

The RTL concept, as shown schematically in Figure 2, is to make a low-mass RTL that connects the pulsed power driver to the z-pinch-driven target. The RTL would enter the chamber through a single hole at the top of the chamber (~1 meter radius), and extend into the chamber a distance of two or more meters. Note that the RTL would bend at the top of the chamber, and upper shielding would be placed above it. The RTL concept alleviates the usual problems of a final optic, pointing and track N beams (N~100), and high-speed target injection. In contrast to those problems, the RTL concept must be shown to be viable and economically attractive. Issues associated with the RTL include movement (required accelerations are low); RTL electrical current initiation; RTL low-mass limit and electrical conductivity; structural properties; mass handling; shrapnel; vacuum/electrical connections; activation; waste stream analysis; shock disruption to liquid walls; manufacturing/cost; optimum configuration (inductance, shape, etc.); power flow limits for magnetic insulation; effects of post-shot EMP, debris, and shrapnel up the RTL; and shielding of sensitive accelerator parts. Initial experiments at the 10 MA level on Saturn have been successfully used to study the electrical current initiation in the RTL, the RTL low-mass limit, and the RTL electrical conductivity [4].

4. Z-Pinch IFE development areas

The development of Z-Pinch IFE has been organized into six research areas as follows:

1. RTL: The present approach is to use a carbon steel RTL, with a total mass of about 50 kg, in a chamber with a pressure of 10–20 Torr. The structural properties of the RTL set the pressure limit. Power flow properties of the RTL are being investigated. The major concern involves electrode heating, the formation of surface plasmas, accurate determination of the electrical conductivity, magnetic field diffusion into the electrode material, and motion of the electrode material during the power pulse. 2D and 3D codes are being used to evaluate these effects.

2. Repetitive pulsed power drivers: Although other potential repetitive pulsed power technologies are being assessed, the present approach is to use a Linear Transformer Driver (LTD) voltage adder accelerator. In the LTD concept, a series of compact low-inductance capacitors are charged directly in parallel, in cylindrical formation. A series of switches next to the capacitors, and in the same cylindrical formation, switch the charged capacitors to directly apply voltage to a single, inductively-isolated gap. Several such cells are combined in a voltage-adder formation to reach high voltage. Progress is being made on an LTD PoP (Proof-of-Principle) accelerator at 1MA, 1MV, 100 ns, 0.1 Hz. Individual cells at the 100 kV, 1MA, 100 ns level are being designed and constructed.

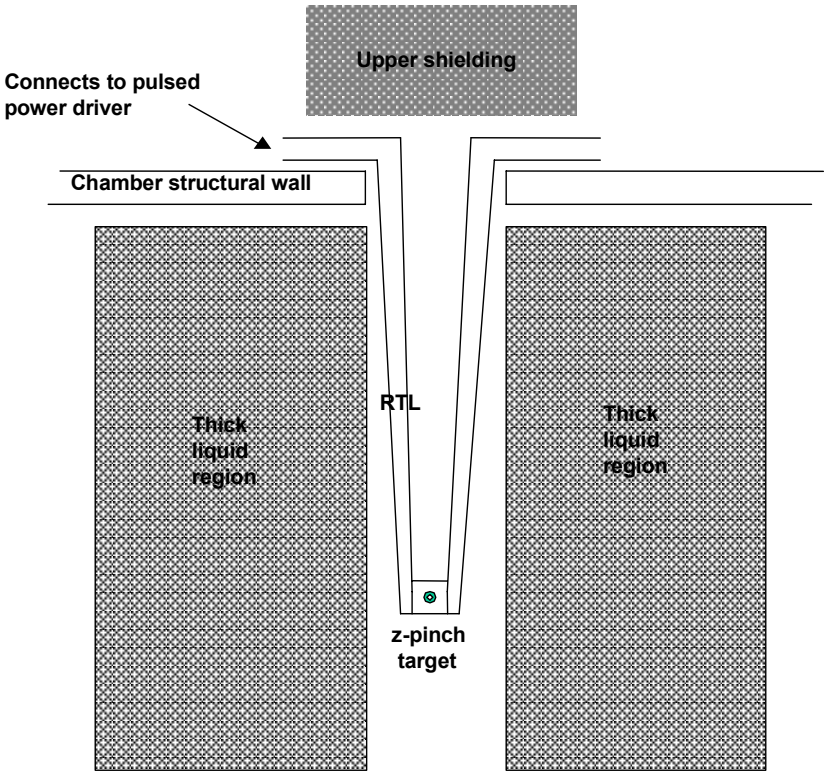

Figure 2. The RTL (Recyclable Transmission Line) concept.

3. Shock mitigation: The fusion yields envisioned for Z-Pinch IFE are large (~3GJ) compared to the other IFE approaches that typically use yields ≤0.4 GJ. Therefore, shock mitigation (in the thick liquid walls) to protect the structural chamber walls is an issue that must be addressed. This is being modeled in scaled experiments with a shock tube and water layers, and with explosives and water jets. Code calculations are being performed with the goal of validating the codes with the experiments, and then using the codes to predict effects for a full-scale Z-Pinch IFE power plant.

4. PoP Experiment Planning: The Z-PoP experiment is in the planning stages. It is based on a 1 MA, 1 MV, 100 ns, 0.1 Hz LTD accelerator, as mentioned above, that is under development. Z-PoP would use this driver, together with an RTL and a z-pinch load (~5 kJ), and would be automated to run at 0.1 Hz. The procedure would be to insert an RTL and a z-pinch load, fire, remove the remnant, reload, and repeat the process. Robotic systems are being investigated to perform these functions for Z-PoP.

5. Targets for Z-Pinch IFE: The dynamic hohlraum target is the preferred target for Z-Pinch IFE, although other targets (double pinch, fast igniter, etc.) are also being considered. Based on Lasnex simulations and analytic scaling studies, fusion yields of 3 GJ may be obtained with this target with gains G of 50–100. This gain, coupled with a driver efficiency (η) that is already 15% (and might be optimized to 25% or more in the future), gives a favorable $\eta G \sim 15$ or more. This high value of ηG ensures a favorable power plant operating scenario.

6. Z-Pinch power plant technologies: An initial multi-chamber Z-Pinch power plant study named ZP-3 was completed to establish one complete (but non-optimized) 1000 MW_e power plant scenario [5]. This concept assumed Marx generator/ water line technology for the

pulsed power driver, an RTL to connect the driver to the target, a dynamic hohlraum target, and a thick-liquid wall chamber. If each RTL is ~50 kg, then a one-day supply would be 5,000 tons. This is the inventory needed for the power plant, and it would be recycled constantly. (For comparison, the one-day *waste* from a coal-fired power plant is about 5,000 tons.) Activation studies indicate that a one-day supply of RTLs should permit a sufficient cool-down time for the RTL material. Further studies regarding activation, waste stream analysis and chamber clearing are in progress.

4. Conclusions

A Z-Pinch IFE program is underway, and substantial progress is being made in all research areas (RTLs, repetitive pulsed power LTD drivers, shock mitigation, PoP experiment planning, target designs for high yield, and thick-liquid wall power plant design).

REFERENCES

[1] OLSON, C.L., "Z-Pinch Inertial Fusion Energy," in the Landholt-Boernstein Handbook on Energy Technologies (Editor in chief: W. Martienssen), Volume VIII/3, Fusion Technologies (Edited by K. Heinloth), Springer-Verlag (Berlin-Heidelberg) in press (2004). [Includes an extensive list of references.]

[2] US DOE FESAC Report, "A Plan for the Development of Fusion Energy," DOE/SC-0074, March 2003.

[3] US DOE FESAC Report, "A Review of the Inertial Fusion Energy Program," DOE/SC-0087, March 2004.

[4] SLUTZ, S.A., OLSON, C.L., and PETERSON, P., "Low Mass Recyclable Transmission Line for Z-Pinch Driven Inertial Fusion," Phys. Plasmas **10**, 429 (2003).

[5] ROCHAU, G.E., et al., "ZP-3, a Power Plant Utilizing Z-Pinch Fusion Technology," IFSA 2001 (Editors: K. Tanaka, D. Meyerhofer, J. Meyer-ter-Vehn), Elsevier, 706 (2002).

Evaluation of a concept of power plant for fast ignition heavy ion fusion

S.A. Medin[1], M.M. Basko[2], M.D. Churazov[2], P. Ivanov[1], D.G. Koshkarev[2], Yu.N. Orlov[3], A.N. Parshikov[1], B.Yu. Sharkov[2], V.M. Suslinc[3]

[1] Institute for High Energy Densities, Moscow, Russian Federation
[2] Institute for Theoretical and Experimental Physics, Moscow, Russian Federation
[3] Keldysh Institute for Applied Mathematics, Moscow, Russian Federation

Abstract. The requirements of the heavy ion fusion power plant concept are based on the fast ignition principle for fusion targets. The cylindrical target is irradiated by a hollow beam in a compression phase and subsequently by a powerful ignition beam for initiation of the burning phase. The ignition is provided by the high energy 100 GeV Pt ions of different masses and charge states accelerated in RF-linac. The efficiency of the driver is evaluated as 0.25. The main beam delivers 7.1 MJ energy and the ignition beam ~0.4 MJ to the target. A cylindrical DT filled target provides 750 MJ fusion yield, of which 17 MJ appear in X-rays, 187 MJ in ionized debris and 546 MJ in neutrons. The multiplication blanket coefficient is calculated as 1.117, so the total energy release is estimated by the value of 814 MJ per one shot. The repetition rate is taken as 2 Hz per reactor chamber. The first wall of the reactor chamber employs a thin liquid wall design, particularly the wetted porous design. The lithium-lead eutectic is used as a coolant, with an initial surface temperature of 550^{o}C. Evaporation of liquid film under X-ray irradiation, revaporisation under debris impact and vapor condensation are computed. The computation of neutronics results in a blanket energy deposition with a maximum density of 20 MJ/m^3. Pulsations of stresses in the blanket tubing and of pressure in the coolant are evaluated. The heat conversion system consisting of three coolant loops provides the net efficiency of the power plant of 0.37.

1. INTRODUCTION

Principal aspects of DT-fusion by the use of a heavy ion driver are determined mainly by two design factors: the type of target drive and the blanket structure. At the moment the most advanced concept, HYLIFE-II [1, 2], is based on the indirect drive of the target and the thick liquid wall of the blanket structure. The advantages of this concept are the mitigation of problems of driver–reactor chamber interface and reactor chamber materials.

The difficulties involved are the organization of radiation-proof pockets of liquid jets and the demand of higher gains in target burn. In ref. [3, 4] an alternative concept of heavy ion fusion has been proposed. In this concept the direct drive of a cylindrical target in fast ignition mode and a thin liquid wall design of the blanket are accepted. This approach is characterized by a simple driver–reactor chamber interface and a moderate value of gain demanded. The problems of the FIHIF concept (fast ignition heavy ion fusion) are connected to the rigid physical conditions of fast ignition scenario implementation and the heavy ion driver length.

In this paper new data on the target energy release and the reactor chamber response are given by using developed numerical codes. The output parameters of the FIHIF power plant are corrected.

2. GROUND PLAN AND HIGH-POWER DRIVER

The ground plan of the FIHIF power plant is outlined in Fig. 1. The length of the main linac is of the order of 10 km. The diameter of storage and compression rings is equal to 1 km. The area occupied by the reactor and turbo generator building, as well as by the cooling towers, is of the same order of magnitude.

The driver is composed of the following major parts [4]. Ion sources for four Pt isotopes with plus and minus charge states are arranged in 8 groups of 4 devices each.

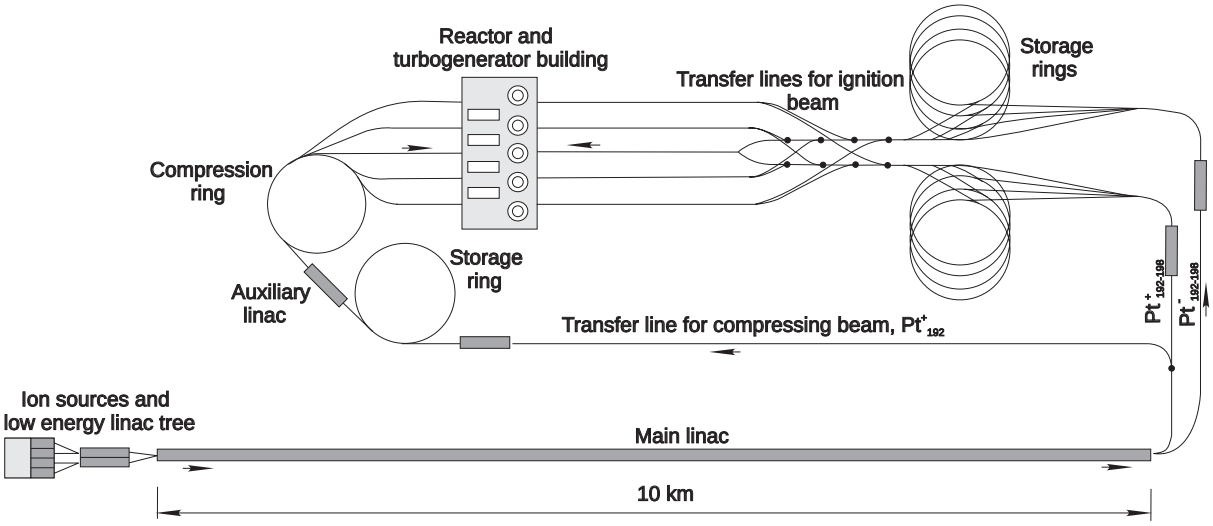

Figure 1. Ground plan outline for FIHIF power plan.

In the main linac the ion energy is increased to 100 GeV. After this the ions with different charges and masses are separated into 8 beams, which are compressed in two stages: in storage rings and in exit sections by the time-of-flight method. The final summation of 8 beams in an individual transfer line results in a single bunch of 0.2-ns-duration delivered to the compressed target. The preliminary compression of the target is accomplished by the hollow beam which carries only Pt^{+}_{192} ions. This beam is temporally profiled over a duration of 75 ns with a maximum current of 1,6 kA. The general parameters of the FIHIF driver are given in Table 1.

Table 1. General parameters of FIHIF driver

Ions	$Pt^{+,-}_{192,194,196,198}$
Ion energy , GeV	100
Hollow compressing beam	
Energy, MJ	7.1
Duration , ns	75 (profiled)
Maximum current, kA	1.6
Rotation frequency, GHz	1
Rotation radius, mm	1,33-1,89
Focal spot radius, mm	0,65-1,33
Ignition beam	
Energy, MJ	0.4
Duration, ns	0.2
Maximum current, kA	20
Spot radius, μm	50
Linac	
Main linac length, km	10
Repetition rate, Hz	8
Driver efficiency	0.25

The repetition rate of the FIHIF driver is taken as 8 Hz, which provides 2 shots per second in each of 4 reactor chambers. The evaluated nominal driver efficiency is equal to 0.25. The operational characteristics of the driver equipment are feasible on the basis of today's developments in acceleration technologies.

3. CYLINDRICAL TARGET

In the present consideration the target has a simple design. The DT fuel cylinder with a radius of 0.112 cm and a length of 0.71 cm is surrounded by a lead shell with a radius of 0.4 cm and a length of 0.8 cm (see Fig. 2). The length of the target is matched to the stopping range of 100-GeV Pt^{+}_{192} ions deposited by the compressing hollow beam. The masses of DT fuel and lead are equal to 5.6 mg and 4.44 g, respectively.

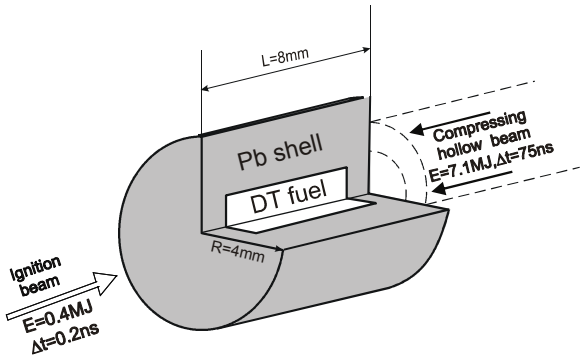

Figure 2. Cylindrical target for FIHIF concept.

The parameters of target compression and burn were determined successively in separate simulations [5]. The burn fraction amounts to 0.39, providing a fusion energy of 750 MJ and a gain of 100. This energy is partitioned among 580 MJ in neutrons, 153 MJ in debris and 17 MJ in X-rays.

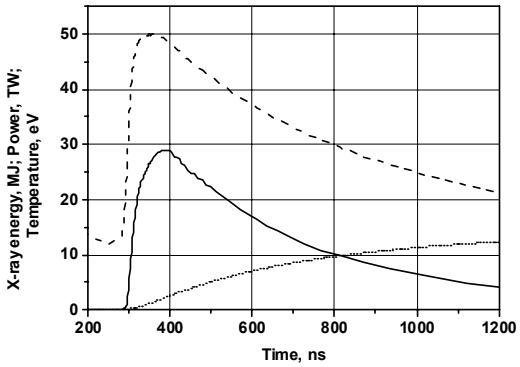

Figure 3. Temporal profiles of X-ray characteristics for an FIHIF cylindrical target. Dashed line: temperature, solid line: power, dotted line: energy.

X-ray radiation is originally absorbed by target material and then reradiated by lead plasma. This causes the decrease of X-ray temperature and delay and lengthening of the X-ray pulse. In Fig. 3 the profile of an X-ray pulse is drawn according to [5]. The duration of the pulse is very long and exceeds 0.7 ms, the mean X-ray temperature is equal to 30 eV.

4. REACTOR CHAMBER DESIGN

The general design of the reactor chamber is shown in Figure 4. The chamber consists of two cylindrical sections: the upper smaller section in which the target explosion takes place and the lower section into which sprayed jets of coolant are injected. The diameters of the sections are 8 m and 16 m respectively. Such a configuration prevents an over-pressurization after the micro-explosion and provides a high rate of vapour condensation on sprayed jets.

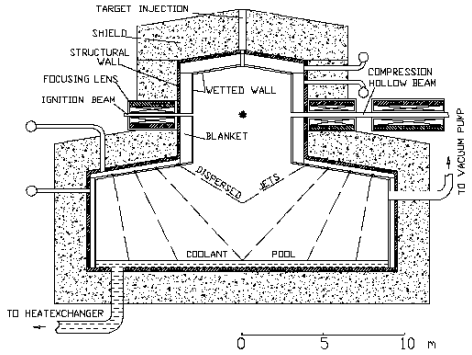

Figure 4. Reactor chamber for an FIHIF power plant.

The coolant is eutectic $Li_{17}Pb_{83}$ with a temperature of 823K. The saturation density of vapour corresponding to this temperature is equal to $10^{18}m^{-3}$, according to [6]. Under this condition the Pt ion beam is not deteriorated by an atmosphere in the reactor chamber.

The first wall and the blanket are of conventional design. The liquid film is formed at an SiC porous wall. In the blanket the tubing is made of vanadium alloy. The structural wall is manufactured of HT-9 steel.

5. CHAMBER RESPONSE TO X-RAYS AND ION DEBRIS

We suppose that X-ray radiation is described by Plank distribution, with temperature and power, depending on time, as shown in Fig. 3. The response of a thin liquid protected layer to X-ray radiation is simulated numerically by the Lagrangian 1D hydrodynamic code in cylindrical geometry. This code solves equations of conservation of mass, momentum and energy with viscosity dissipation and heat transfer in the film. The energy deposition of X-ray radiation in the film is computed by means of a mass attenuation coefficient for eutectic $Li_{17}Pb_{83}$ determined by way of individual substance data, depending on photon energy, given in ref. [7]. The wide-range equation of state is taken from ref. [8] only for lead, because the presence of lithium is neglected in thermodynamic properties. In this equation of state the vaporization and the first ionization of lead is taken into account.

The energy deposition of X-ray radiation occurs immediately in thin liquid layers and later in the vapour which expands from the liquid surface.

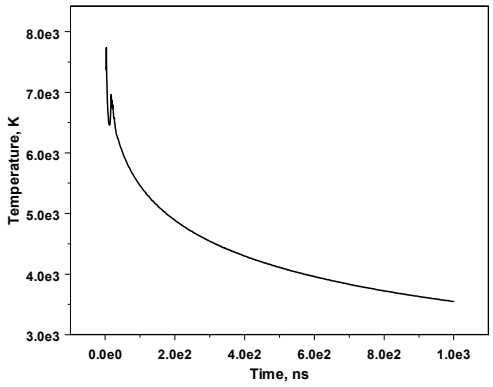

Figure 5. Vaporization front temperature versus time.

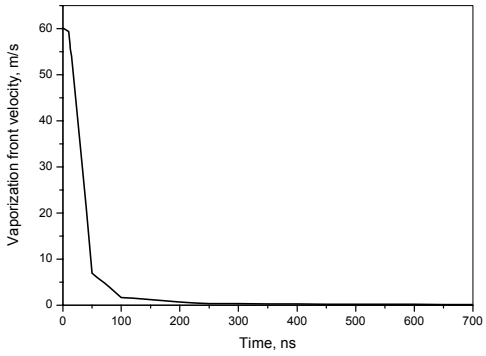

Figure 6. Velocity of vaporization front propagation in the liquid film versus time.

The rate of vaporization depends on X-ray intensity and is strongly influenced by X-ray absorption in this vapour layer. In Figs 5 and 6 the temporal variations of the temperature and the velocity of the vaporization front are presented. After 100ns the vaporization rate begins to decrease despite of the fact that the X-ray intensity continues to rise. This is caused by the intensive absorption of X-ray radiation by vapour and demonstrates a screening effect of the vapour layer. The total mass vaporized by the end of the X-ray pulse is some 1.42 kg (see Fig. 7).

Temperature and density of this vapour are extremely non-uniform. There is a rarefied ionized external zone with a temperature of 3×10^6 K (see Fig. 8) and a density of 10^{-6} kg/m^3. The inner layer, adjacent to the liquid film, has a temperature of 3000 K. The average temperature of vaporized coolant is 1.6×10^5 K, the average density is 0.07 kg/m^3.

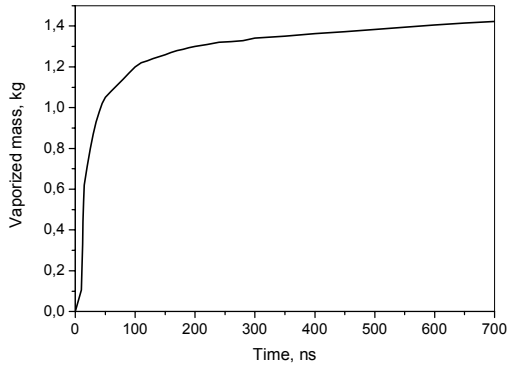

Figure 7. Temporal variation of vaporized mass in the reactor chamber during X-ray exposion.

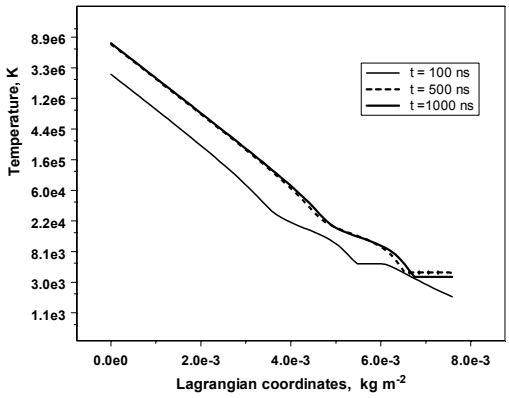

Figure 8. The temperature distribution in the vaporized coolant at various times.

The vaporization process is accompanied by shock wave generation in the liquid film. This shock wave travels across the film, with the sound velocity approximately equal to 2000 m/s (see Fig. 9). It crosses the 2 mm wide film in 1 μs and comes to the first wall with an amplitude of 250 MPa. The pressure in the tail of the pressure profile is equal to the saturation pressure at the vaporization front. It can be seen that the saturation pressure decreases in the time following the power variation of X-rays. The displacement of the vaporization front is rather small and not noticeable in Fig. 9 due to the fact that the front velocity (Fig. 6) is much smaller than the velocity of sound.

The pressure at the vaporization front, calculated according to the equation of state, enables us to numerically determine the impulse transmitted to the first wall during the time interval τ =1000 ns. It turns out to be equal to I = 64 Pa·s. Thus the loading for the first wall is estimated to be $P_1 = I/\tau = 64$ MPa. Taking the first wall to be a thin spherical shell, deformed by this loading, we calculated the corresponding displacement of the porous first SiC wall, which is equal to 4×10^{-6} m. Then we could calculate the maximal pressure on its external surface on contact with coolant. It is equal to P_{10} = 14 MPa. We took the elasticity limit of the porous SiC wall to be equal to Y_0 = 35 MPa. Since the radial stress P_{10} of this radial stress value turned out to be below the elasticity limit Y_0 (the so-called von Mises criterion), we conclude that the first wall remained in the elasticity deformation region under this loading.
The target debris approaches the vapour layer at 10 microseconds.

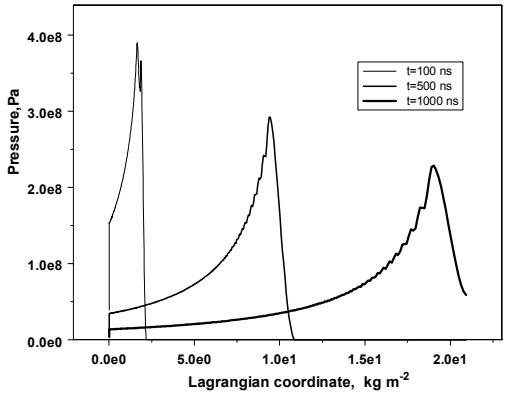

Figure 9. Shock wave propagation in liquid film.

Further interaction of the debris flow and the vapour layer is determined by the stopping range of 80 keV ions of lead, which is equal to 6×10^{-6} g/cm^2 according to the Bethe-Bloch formula of the Coulomb energy losses [9]. Thus the stopping range is much smaller then the vapour layer. Therefore it can be assumed that evaporated coolant is additionally superheated by debris ions. The evaluated resulting temperature of vapor amounts to 230 eV (approximately equal to 2.5×10^6K). The process of additional vaporization and condensation is considered to start at this initial temperature of vapour (see Figs 10, 11).

We describe the evaporation-condensation processes by kinetic relationships [10] in the same way as in ref. [4].

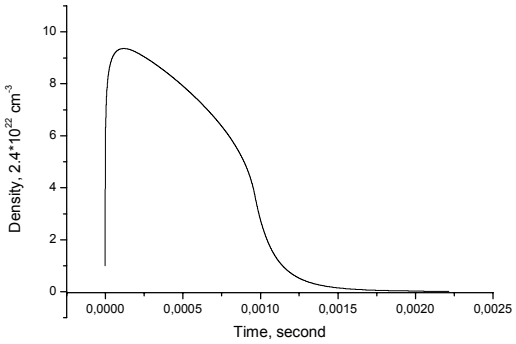

Figure 10. Temporal variation in vapour density in the reactor chamber after the shot.

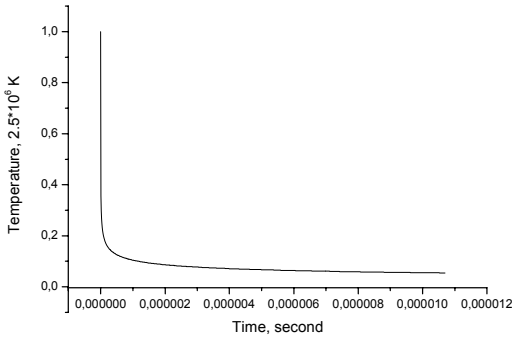

Figure 11. Temporal variation in vapour temperature in the reactor chamber after the shot.

After a time of 10 μs the pattern of vapour cooling changes. Condensation prevails over vaporization and the rate of temperature decrease slows down. Revaporization results in a density rise of one order of magnitude. The maximum mass of evaporated coolant is 14 kg. The droplets of dispersed jets in the lower chamber section (see Fig. 4) provide the needed condensation surface (4.5×10^4 m^2 for droplets with a total mass of 7,000 kg per shot). The change to a decreasing rate of condensation after 1 ms is due to the additional condensation of vapour on the dispersed jets after that time, which is needed for the uniform spreading of ionized vapour all over the chamber.

Vapour density practically reaches its saturation value at 0.01 s. This indicates that the condensation process would not limit a repetition rate of shots. Apparently, the actual limitation will be the rate of clean-up of liquid droplets. In the case of gravity-free precipitation the repetition rate does not exceed 2 Hz

6. NEUTRON HEATING OF BLANKET

The neutron source generated in a DT-reaction is presented in Figure 12, in accord with Ref. 5. The duration of the effective burning is equal to approximately 1 ns, so that we can consider the heating of the blanket instantaneous.

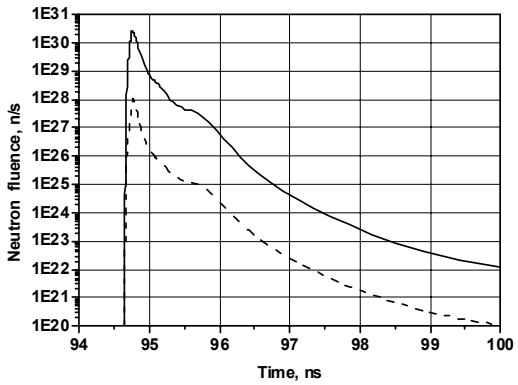

Figure 12. Neutron pulse of the FIHIF target micro-explosion. Solid line: 14 MeV; dotted line: 2.45 MeV.

The neutron spectrum is evaluated in stationary calculations using the MCNP code [12] in spherical approximation to the moment of the central peak of the neutron pulse. The average neutron energy is equal to 12.2 MeV. Two-dimensional calculations of neutron transport in the blanket by using the MCNP code arrived at a high energy release in the materials (see Table 2). The tritium-breeding ratio (TBR) for this blanket is equal to 1.112, and the blanket multiplication factor is evaluated at the value of 1.117. The neutron energy of 546 MJ is multiplied in the blanket up to a value of 610 MJ. Thus the total energy release per one shot is equal to 814 MJ.

The blanket is presented as a multi-layer cylinder the structure of which is given in Table 2. The total blanket and the structural wall thickness is equal to 52 cm. We enumerated blanket zones and inner radii from the surface of the liquid protecting layer. The scheme of coolant motion through the vanadium tubes is presented in Figure 13.

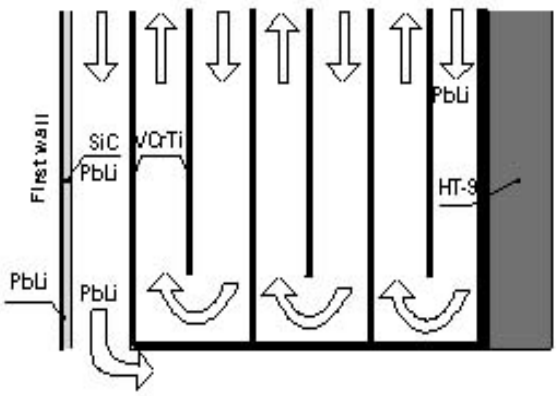

Figure 13. Scheme of coolant motion through the vanadium tubes.

Table 2. Blanket structure and energy deposition in the zones

Zone	Matter	Radius, cm	Energy density, MJ/m^3	Temperature rise, K
1	PbLi	400.0	23.8	13.0
2	SiC+PbLi	400.2	20.7	5.1
3	PbLi	401.0	18.5	11.1
4	V4Cr4Ti	407.0	8.9	2.8
5	PbLi	407.4	12.2	7.3
6	V4Cr4Ti	413.4	6.1	1.7
7	PbLi	413.8	6.5	4.0
8	V4Cr4Ti	419.8	2.8	0.9
9	PbLi	420.2	4.1	2.0
10	V4Cr4Ti	426.2	1.1	0.5
11	PbLi	426.6	1.5	0.9
12	V4Cr4Ti	432.6	0.8	0.2
13	PbLi	433.0	0.9	0.4
14	V4Cr4Ti	439.0	0.2	0.1
15	PbLi	439.4	0.3	0.2
16	V4Cr4Ti	445.4	0.1	0.05
17	HT-9	446.4	0.07	0.01
18	Concrete	452.0	-	-

Neutron heating generates a pressure/stress pulse which travels across the blanket and refracts at the contact surfaces. For evaluation of material loading we solve 1D hydrodynamic equations in cylindrical geometry. The computational interval includes blanket, structural wall and concrete shield. Free adiabatic boundary conditions were used. Initial distributions were uniform for all the parameters except for internal energy which was determined from neutronics computations. The data for solid materials, silicon carbide, vanadium alloy and stainless steel are given by Zinkle in ref. [12]. The eutectic $Li_{17}Pb_{83}$ properties are taken from Ref. [13]. The equation of state is taken in the Mie-Gruneisen form. The Gruneisen coefficient Γ is projected as 2 for the SiC porous wall, stainless steel and concrete. In Figs 14 the pressure distribution in the blanket and the structural wall is drawn for different moments of time. The right boundary is the contact interface between stainless steel and concrete. The main pulsations are modulated by low frequency which can be caused by refracted pulse reflection

in concrete. Small-amplitude high-frequency pulsations are produced by the tubing walls reverberations.

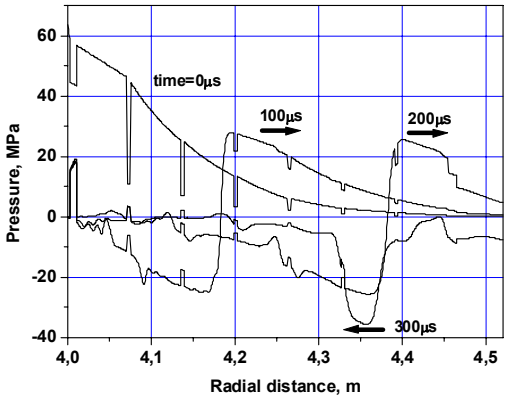

Figure 14. Pressure distribution in the FIHIF reactor chamber blanket and the structural wall at various times.

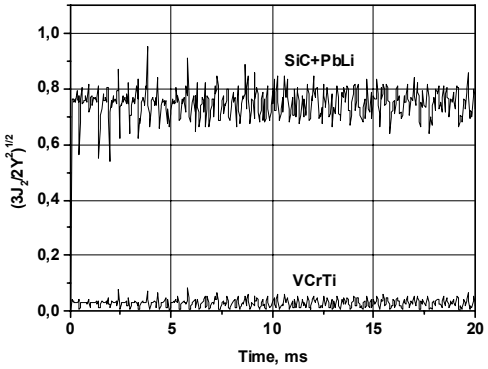

Figure 15. Temporal variation of equivalent stress normalized by yield stress Y (Y= 35 MPa for SiC/PbLi and 280 MPa for V-Cr-Ti). The von Mises criterion ($\sigma_e \leq Y$) determines elastic/plastic material behaviour.

In the walls a control of stresses with respect to the strength material behaviour is needed. In Figure 15 the equivalent stress $\sigma_e = (3J_2/2)^{1/2}$, normalized by the yield stress *Y,* is plotted versus time for two construction walls: the first wall of SiC+PbLi and adjacent to it a V-Cr-Ti wall. The equivalent stress σ_e in the first wall is quite near to the yield stress *Y*, while in the vanadium alloy wall σ_e is substantially less than *Y*. According to the von Mises criterion $\sigma_e \leq Y$ both materials are in the elastic mode of loading.

7. ENERGY CONVERSION AND BALANCE OF PLANT SYSTEM

The energy conversion system consists of three loops. The coolant of the second loop is sodium. The third loop is a steam turbine cycle. The key parameter of the system is the maximum temperature of $Li_{17}Pb_{83}$ at the outlet of the reactor chamber. It is taken as 823K. The inlet temperature of the eutectic is equal to 623K. The inlet and outlet temperatures of sodium in the intermediate heat exchanger are 573K and 773K, respectively. In Table 3 the mass flow rate and the pump power for liquid metal coolants are given.

Table 3. Parameters of thermal loops of an FHIF power plant

First loop	
Coolant	LiPb
Mass flow rate, kg/s	13063
Pump power, kW	11584
Second loop	
Coolant	Na
Mass flow rate, kg/s	6402
Pump power, kW	3768
Steam Cycle	
Mass flow rate, kg/s	548.7
Inlet pressure, MPa	18
Superheat pressure, MPa	3
Condenser pressure, MPa	0.009
Turbine efficiency	0.875
Steam cycle efficiency	0.417
Reactor	
Fusion power, MW	1500
Driver power, MW	60
Neutron power ratio	0.773
Blanket multiplication	1.117
Power plant	
Thermal efficiency	0.407
Net efficiency	0.374
Net power output, MW	626

The steam cycle is configured with a reheat. The initial steam temperature and the reheat temperature are equal to 743 K. The temperature of feeding water is computed as 450 K. The efficiency of the steam cycle equals 0.407. Taking into account the driver efficiency, the target gain and the blanket multiplication for the fusion power of 1500 MW, we obtain the net efficiency of the plant of 0.373 and the net power per one reactor of 626 MW.

The thermal scheme of an FIHIF power plant is presented in Figure 16.

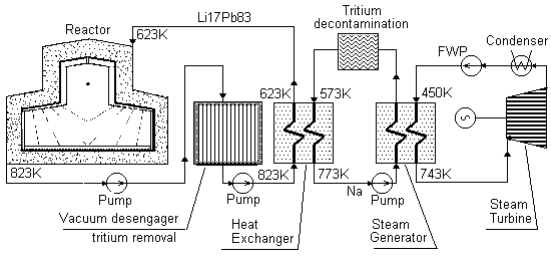

Figure16. Thermal scheme of an FIHIF power plant.

8. CONCLUSIONS

The FIHIF physical scenario based on the high-energy ion beams drive of a cylindrical target involves a realistic acceleration technology and a simple target design. The configuring of the reactor of two sections gives a possibility to increase the rate of vapour condensation and to reduce the vapour pressure loading. The problems of vapour fog in the chamber and pressure-stress pulsations in the blanket are a major concern of the reactor. The material limitations and tritium contamination of coolant determine the thermodynamics of the thermal scheme. The balance of the plant is highly influenced by the driver energy consumption. An improvement in material characteristics and the driver–target performance are needed to increase the efficiency of the power plant.

ACKNOWLEDGEMENTS

This work is sponsored by the Human Capital Foundation under contract N32. It is supported in part by the Programme of the Mathematical Department of the Russian Academy of Sciences N3.

REFERENCES

[1] J.D. LINDL et al., Plasma Phys. Contr. Fusion 45 (2003) A217.
[2] W.R. MEIER et al., Fusion Eng. Des. 62–63 (2003) 577.
[3] S.A. MEDIN et al., Laser Part. Beams 20 (2002) 419.
[4] S.A. MEDIN et al., Fusion Sci. Technol. 43 (2003) 437.
[5] M.M. BASKO et al., Laser Part. Beams 20 (2002) 411.
[6] R.W. MOIR, Fusion Eng. Des. 32–33 (1996) 93.
[7] HUBBELL J.H., SELTZER S.M. Tables of X-Ray Mass Attenuation Coefficients. NIST (1996).
[8] V.P. KOPYSHEV, A.B. MEDVEDEV. Thermodynamic model of compressing covolume. Sarov: VNIIEF (1995) (in Russian).
[9] B. ROSSI, High Energy Particles, Prentice-Hall, Englewood Cliffs, New Jersey (1952).
[10] V.P. ISACHENKO, Heat Transfer in Condensation Processes, Energia, Moscow (1977) (In Russian).
[11] GROUP-6, “MCNP – A General Monte Carlo Code for Neutron and Photon Transport”, LA-7396-m revised, Los Alamos National Laboratory (Apr. 1981).
[12] S.J. ZINKLE, Status of Recent Activities by the APEX Material Group, APEX Study Meeting, Sandia National Laboratories (1998) 18.
[13] V.N. MIKHAILOV et al., Lithium in fusion and space power in the 21st century, Nauka, Moscow (1999) (in Russian).

The Mercury Laser, a gas cooled 10 Hz diode pumped Yb:S-FAP system for inertial fusion energy

C. Bibeau, A.J. Bayramian, P. Armstrong, R.J. Beach, R. Campbell, C.A. Ebbers, B.L. Freitas, T. Ladran, J. Menapace, S.A. Payne, N. Peterson, K.I. Schaffers, C. Stolz, S. Telford, J.B. Tassano, E. Utterback

Lawrence Livermore National Laboratory, Livermore, California, United States of America

Abstract. The Mercury laser project is part of a national inertial fusion energy programme in which four driver technologies are being considered, including solid-state lasers, krypton fluoride gas lasers, Z-Pinch and heavy ions. These drivers will be evaluated on several important criteria including: scalability, efficiency, reliability, cost, and beam quality. Mercury's operational goals of 100 J, 10 Hz, 10% efficiency in a 5 times diffraction limited spot will demonstrate the critical technologies before scaling the system to the multi-kilojoule level. Operation of the Mercury laser with two amplifiers has yielded 30 Joules at 1 Hz and 12 Joules at 10 Hz with over 8 10^4 shots on the system. Static distortions in the Yb:S-FAP amplifiers were corrected by a magneto-rheological finishing technique.

1. INTRODUCTION

The Mercury laser was initially commissioned with a single amplifier module to test the basic architecture and assess the performance of several component technologies: high-power diode arrays, Yb:S-FAP crystals, gas cooling, and a high average power Pockels cell [1]. In this paper we report on the first integrated operation of the system with two amplifiers in an upgraded facility that includes Class 100 clean room systems, enhanced controls and several diagnostic stations (Figure 1). The primary focus has been on energy and average power operation at 1.047 um, but there will be added active wavefront control and average power frequency conversion capabilities to meet our requirements for a scalable inertial fusion driver.

The Mercury laser project is part of a national inertial fusion energy programme in which four driver technologies are being considered, including solid-state lasers, krypton fluoride gas lasers, Z-Pinch and heavy ions. These drivers will be evaluated on several important criteria including: scalability, efficiency, reliability, cost, and beam quality. Mercury's operational goals of 100 J, 10 Hz, 10% efficiency in a 5 times diffraction limited spot will demonstrate the critical technologies before scaling the system to the multi-kilojoule level.

2. CRYSTALS AND GAS COOLING

In the process of down-selecting the optimum gain medium, we explored numerous gain materials and architectural options to best fit the design space of a fusion energy class laser. Yb^{3+}:$Sr_5(PO_4)_3F$ or Yb:S-FAP was chosen as the gain medium, based on its long energy storage lifetime, suitable absorption and emission cross sections, and good thermal conductivity. Although the fabrication of full aperture Yb:S-FAP slabs of $4 \times 6 \times 0.75$ cm^3 has been quite challenging, we have made good progress towards growing large enough boules to produce full-size slabs. Successful growth techniques by Northrop Grumman Inc. have yielded 6.5 cm diameter by 10 cm long boules from which 2 full-size amplifier slabs can be fabricated. The next challenge has been cutting the boules without fracturing, since the growth techniques employed to eliminate or reduce crystalline defects have produced boules

that are difficult to cut due to the high residual stress from the growth process. We have found that water jet cutting of the material is gentle compared to other cutting techniques and is now the standard process for cutting Yb:S-FAP.

a) 

Figure 1. A picture of the Mercury laboratory showing dual amplifiers and Class 1000 clean room enclosures which minimize air turbulence and decrease optical damage due to contaminants.

After cutting the boule, the crudely shaped slabs are polished into their final form. If the transmitted wavefront does not meet the $\lambda/10$ peak-to-valley or $\lambda/90$ cm^{-1} gradient specification, the slab is re-polished by magneto-rheological finishing (MRF), which is a method of deterministically removing material from the surface. The MRF technique is capable of removing features down to the 1 mm scale and to several waves in amplitude. An example of a slab polished by the MRF technique is shown in Fig. 2, where the stress-induced distortion is removed from the bonding process. In addition to the wavefront distortion, we are also concerned with the optical lifetime of the slabs. Employing established polishing technology adapted to the Yb:S-FAP material, subsurface damage is removed and the surface micro-roughness can be reduced to less than 3nm. The measured damage threshold at 1047 nm of conventionally or MRF polished Yb:S-FAP substrates has increased to 18 J/cm^2 at 3 ns. The slabs are mounted with a compliant urethane compound into aerodynamic aluminum structures called “vanes”. The faces of the two crystals are separated by 1 mm in helium gas cooling channels where the typical gas velocity exceeds Mach 0.1 at four atmospheres of helium pressure.

3. LASER DIODES AND ARCHITECTURE

The laser diodes emit at 900 nm to overlap the 4.6 nm wide Yb:S-FAP absorption line. The diodes are precision-mounted onto etched silicon heatsinks with microlenses to increase brightness by 10×, then secured onto large copper cooling blocks [2]. Each amplifier assembly is pumped by four 80 kW diode arrays. The diode arrays are separated to allow for the passage of the 1047 nm extraction beam through the center. The diode array light is guided to the amplifier through multiple reflections within a hollow, highly reflective metal lens duct and a parallel plate homogenizing structure.

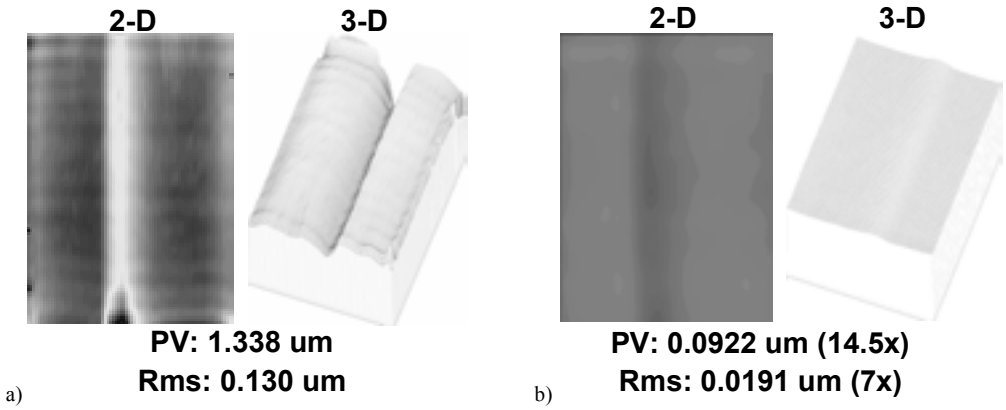

Figure 2. a) Initial phase of bonded slab showing 1.338 micron wavefront distortion, and b) Final phase of amplifier slab after MRF treatment showing 0.0922 micron wavefront distortion.

The overall architecture employs a 5 mrad angularly multiplexed, four-pass beam layout. Image relaying of the laser beam with telescopes between the amplifiers helps to greatly reduce the intensity modulation at the crystalline amplifiers. An average-power, birefringence-compensated Pockels cell [3] is inserted after two passes at low fluence (<1 J/cm^2) to help suppress the energy buildup of any parasitic beams.

The laser system, diode laser power conditioning, and utilities are all computer-controlled. A full suite of sensor packages has been fielded to diagnose the beam after each pass. The most important diagnostic is the dark field which allows rapid detection of 100 um size damage in the amplifier relay plane at 10 Hz. When the computer software algorithm detects a change in the dark field image, a signal is sent to the control system to shut down the laser.

4. LASER EXPERIMENTS

During the first commissioning of the amplifier seven Yb:S-FAP slabs were utilized. The multipass architecture was still incorporated to test the 4-pass architecture concept [1]. These tests were performed before MRF had been utilized on bonded Yb:S-FAP slabs. To compensate for the distortions, a static phase plate was made with MRF technology to correct collective distortions of all the slabs. We measured a factor-of-three improvement in the energy within a diffraction-limited spot (Figure 3a). The energetics data curve for the single amplifier system was mapped by keeping the front-end energy constant and increasing the diode pump pulsewidth to increase the gain. The data shows reasonable overlap with our energetics model with no adjustable parameters (Figure 3b). Utilizing 360 mJ of front energy and pumping for up to 1 millisecond, we were able to extract up to 33.4 joules of energy at 1047 nm, which corresponds to a 4.6% electrical to optical efficiency. Increasing the pump repetition rate to 5 Hz, 114 W of average power was achieved with <0.5% rms energy fluctuation (Figure 3c) for 20 minutes. The single amplifier activation campaign had an accumulation of greater than 3.8×10^4 shots. The beam quality or M^2 of the output beam was captured at this highest power level and was found to be 2.8×6.3 times diffraction limited, with the larger divergence associated with the bond distortion.

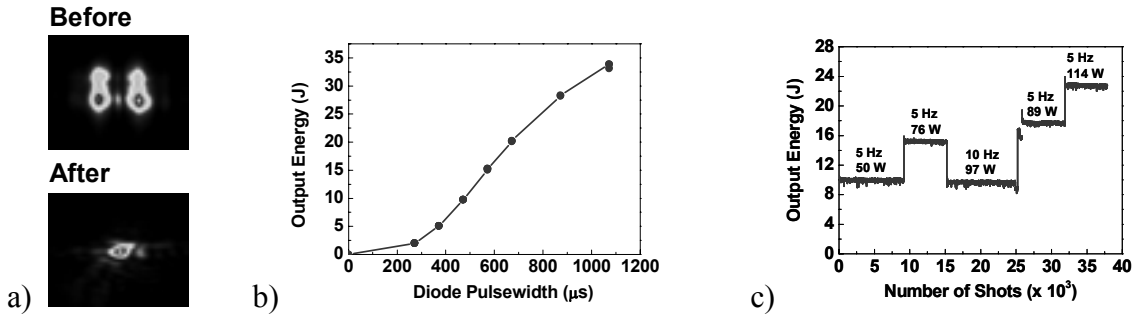

Figure 3 a) Far field image of the amplifier head ~ 15 times diffraction limited, and with the additional wavefront corrector ~5 times diffraction limited, b) Single-shot energetics showing peak energies of 33.5 J, c) Mercury energetics operation for several repetition rates up to 114 W, 23.5 J at 5 Hz for 20 ns pulsewidths

The single amplifier tests allowed us to test many of the key components in the system while additional slabs were undergoing fabrication. Adjustments to the control and diagnostics were made to enhance speed and resolution. Operation protocols and code benchmarking were some of the activities fine-tuned during this campaign.

The second set of laser experiments utilized two amplifiers with four Yb:S-FAP slabs mounted in each amplifier. Of the eight slabs installed, four of the Yb:S-FAP slabs had an MRF correction for transmitted wavefront, and were placed in the last and highest fluence amplifier. Energetics of the 8-slab system were performed with peak energies of 40 J (Fig. 4a). The output near field shows <1.33 peak compared to average modulation (Fig. 4b) and the output far field (Fig. 4c). Energetics and beam modulation agree with our predictions.

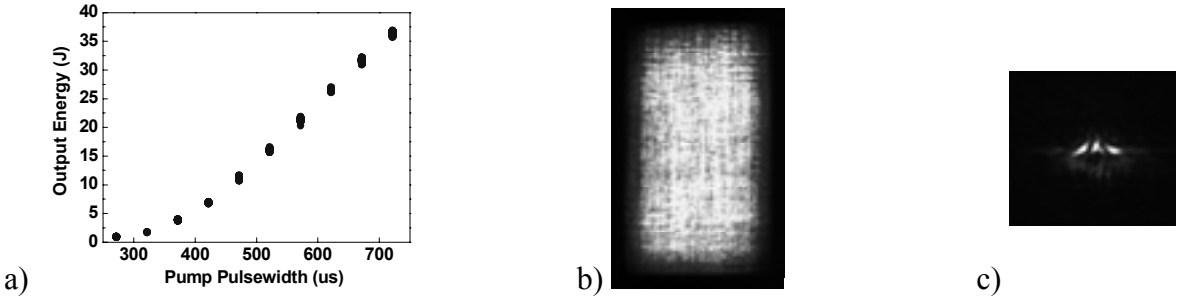

Figure 4 a) Energetics of 8 slab, two amplifier system, b) Output near field, c) Output far field.

In the coming months four additional slabs will be installed in the system, increasing the extracted energy to more than 70 J. The system will be operated at 10 Hz at 1–2 hour run times. In addition, an average power frequency conversion module will be commissioned. The predicted output of the harmonic converter should exceed 20 J or 40% of conversion efficiency. A temporal pulse-shaping upgrade to the front end will allow the generation of shorter pulses, which will further enhance the performance and bring us closer to our system milestones. We also plan to incorporate active wavefront control to allow for wavefront correction of thermal distortions.

ACKNOWLEDGEMENTS

This work was performed under the auspices of the U.S. Department of Energy by the University of California Lawrence Livermore National Laboratory under contract No. W-7405-Eng-48.

REFERENCES

[1] A.J. Bayramian, R.J. Beach, C. Bibeau, et al., "Operation of the Mercury Laser; testbed for DPSSL IFE driver technology", Proc. Inertial Fusion Sciences and Applications, pp. 563–567 (2003).

[2] J.A. SKIDMORE, B.L. FREITAS, J. CRAWFORD, J. SATARIANO, E. UTTERBACK, L. DIMERCURIO, K. CUTTER, S. SUTTON, "Silicon monolithic microchannel-cooled laser diode array," Appl. Phys. Lett., 77, 10–12 (2000).

[3] C.A. EBBERS, K. KANZ, H. NAKANO, "A thermally compensated, deuterated KDP Q-switch for high-average power lasers". Paper presented at the Conference for Lasers and Electro Optics, Baltimore, Maryland, 2002.

Progress in inertial fusion energy modelling at DENIM

G. Velarde[1], O. Cabellos[1], M.J. Caturla[4,5], R. Florido[3], J.M. Gil[3], P.T. León[1], R. Mancini[6], J. Marian[5], P. Martel[3], J.M. Martínez-Val [1], E. Mínguez[1], F. Mota[1], F. Ogando[1,2], J. M. Perlado[1], M. Piera[1,2], R. Rodríguez[3], J.G. Rubiano[3], M. Salvador[1], J. Sanz[1,2], P. Sauvan[1,2], M. Velarde[1], P. Velarde[1]

[1] Instituto de Fusión Nuclear - DENIM, Universidad Politécnica de Madrid, Spain
[2] Departamento de Ingeniería Energética, Univ. Nac. Educación a Distancia, Spain
[3] Departamento de Física, Universidad de Las Palmas de Gran Canaria, Spain
[4] Dpto. Física Aplicada, Universidad de Alicante, Spain
[5] Lawrence Livermore National Laboratory, California, United States of America
[6] Physics Department, University of Nevada, Reno, Nevada, United States of America

Abstract. New results of the jet-driven ignition target are presented, both with direct and indirect drive. This target is based on the conical guided target used in fast ignition but uses only one laser pulse. The ignition of the target is started by the impact of a jet produced in the guiding cone, instead of using charged particles generated by another high-power laser. We have shown that a laser or X-ray pulse could be used to produce a high-velocity jet of several hundred km/s by an accumulative effect, and we use these ideas to design this new kind of targets. In order to increase the efficiency of the process, we scan in simulations different materials, cone profiles and laser intensities. ANALOP is a code developed to calculate opacities for hot plasmas, using analytical potentials including density and temperature effects. It has been recently updated to include the radiative transport into rate equations by means of escape factors; in parallel, a line transport code has been developed which solves self-consistently the rate equation and radiative transfer equation in 1D planar geometry. We have developed a comprehensive methodology to compute uncertainties in activation calculations. First we developed a sensitivity-uncertainty analysis method providing the uncertainties of the different inventory response functions based on the individual uncertainty of each of the reaction cross sections. Lately we have developed and proved the excellent behaviour of a Monte Carlo-based methodology in assessing the synergetic/global effect of the complete set of cross-section uncertainties in calculated radiological quantities. The methods have been applied to the activation analysis of the National Ignition Facility (NIF) and to different IFE concepts (HYLIFE and Sombrero). Research on multiscale modelling of radiation damage in metals will be presented in comparison with "*ad hoc*" experiments. Research on SiC composites is being pursued at a macroscopic level. Results from theory and simulation show that physics is being slowly progressing. The systematic identification of the type of stable defects is the first goal that will be presented after verification of a new tightly binding MD technique. The different level of knowledge between simulation and experiments will be emphasized. Our research on the simulation of Silica Irradiation Damage will also be presented. In addition, we will present the role of ingestion of tritiated foods, where the most important chemical forms of tritium, elemental tritium (HT) and tritiated water (HTO), are derived in a special form of tritium: Organically Bound Tritium (OBT).

1. TARGET DESIGN AND FLUID DYNAMIC SIMULATIONS

A new target design for ICF has been proposed and simulated in search for a new and simpler way to achieve ignition by using fast ignition [1]. The fast ignition concepts so far designed were based on a conventional implosion scheme combined with a secondary energy drive which imparts an ultra-fast pulse of energy that ignites a spark on the compressed target, starting a burning wave that spreads to the rest of the nuclear fuel. That secondary drive has been proposed to be either laser or ions, but in any case different from the primary energy drive, which increases the complexity and costs of the needed facilities.

The new proposed design contains the main ideas of fast ignition, while using a single energy drive that produces both fuel compression and ultra-fast energy deposition on it. The deposition of energy is produced by the impact of a hyper-velocity jet onto the compressed core, converting thereby kinetic energy into thermal energy that produces a hot spot. The

hyper-velocity jet is produced simultaneously fuel compression by the ablationally driven collapse of a conically shaped system, which absorbs energy from the same energy source that produces fuel compression. The design (see Figure 1) includes a spherical conventional target for fast ignition (i.e., not a full sphere) coupled to one or two cones pointing inwards in such a way that they, if properly designed, produce hyper-velocity jets arriving at the center of the system at the precise moment of highest compression and temperature of the nuclear fuel. Between the fuel and the conical system, there are conical shapes facing outwards, with the objective of preventing interaction between the two above-mentioned target zones.

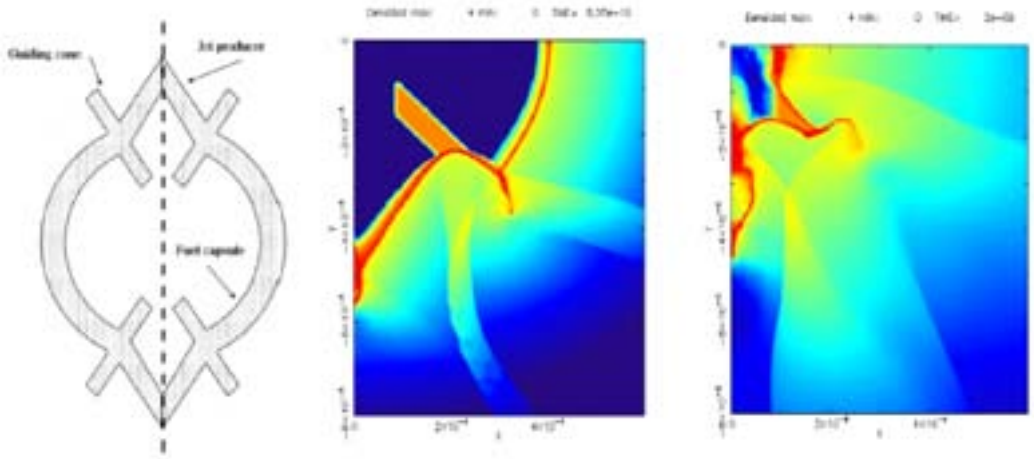

Figure 1. Schematics (a), density plots at 835ps (b) and 2000ps (c).

This design has been simulated using the ARWEN code [2], achieving acceptable results [1]. The simulations performed so far used one material for the whole system, showing in spite of that an appreciable temperature rise in the collision zone of the fuel core. In order to predict the propagation of the burning wave, conditions had to be established and proved which could be achieved by the system in the simulations. The ARWEN code is being adapted to perform multi-material calculations, which will show a better performance of the system. Other designs have been proposed [3] based on the idea of fast ignition by impact of high-speed matter, which are still in the stage of simulation and optimization.

The system has been simulated as being inside a hohlraum with a radiation temperature equivalent to 300eV, thus using indirect radiation. In the first instance an ablation process is started, producing along the whole contour shock waves travelling inwards. These shock waves produce two different effects in both the fuel shell and the conical regions. On the spherical shell, due to the guiding effect of the outward-facing cones, matter is compressed in a uniform way, as was first shown in [4]. At the same time, the shock waves on the conical region produce a jet that grows in time on speed and mass (Figure 1b shows a density map in log scale).

In a precise design stating selected angles and thickness, it was shown in [1] that an appropriate synchronisation could be achieved leading to a collision of the compressed fuel during the first stages of expansion, when its core was in the most compressed state. The collision produced a hot spot in the lowest part of the compressed fuel (Figure 1c shows a density map in log scale).

2. INERTIAL FUSION FEATURES IN DEGENERATE PLASMAS

Very high plasma densities can be obtained at the end of the implosion phase in Inertial Fusion targets, particularly in the so-called fast-ignition scheme, where a central hot spark is not sought at all. By properly tailoring the fuel compression stage, degenerate states can be reached. In that case, most of the relevant energy transfer mechanisms involving electrons are affected. For instance, bremsstrahlung emission is strongly suppressed [5]. In fact, a low ignition-temperature regime appears at very high plasma densities, due to radiation leakage reduction [6]. In this case, stopping power and ion-electron coulomb collisions are also changed, which are important mechanisms to trigger ignition by the incoming fast jet and to launch the fusion wave from the igniting region into the colder, degenerate plasma. All these points were reviewed in a recent paper [7]. Although degenerate states would not be easy to obtain by target implosion, they present a very interesting upper limit that deserves more attention in order to complete the understanding on the different domains for Inertial Confinement Fusion. A programme F.I.N.E. (fast ignition nodal energy) has been developed.

In the programme, the equations defined are valid for the degenerate and classical region, taking into account the possibility that the plasmas pass from a degenerate state to a classical state during the heating process. The results of the programme are only valid for studying the possibility of ignition of plasmas in the fast ignition concept, not the burn-up phase of the target. Ions have been the choice for ignitor heating until ignition conditions are reached. The optimisation of the compression phase in fast ignition inertial fusion, to obtain low temperature and high-density plasmas, can lead to degenerate plasma. The equations that govern these plasmas are different from the classical ones. The decrease in bremsstrahlung emission permits a decrease in ignition temperature for high-density plasmas. This assumption has been demonstrated. The high energy needed to obtain these high-density degenerate plasmas decreases the gain as compared to the results obtained in more moderate densities (see Figure 2*)*.

3. ATOMIC PHYSICS

Optical properties of plasmas are a powerful tool for plasma diagnosis. As it is known, optical properties depend strongly on the level populations in the plasma, applying both to plasmas in LTE and NLTE conditions. Up to now the model proposed by us, the ANALOP code [8], was only able to model optically thin plasmas, i.e., assuming that the self-absorption was negligible. For optically thick plasmas the rate equations and the radiation transfer equation are coupled and should be resolved simultaneously, since under these conditions the self-absorption of the radiation in the plasma has a considerable influence on the level populations.

Recently we proposed two different models in order to provide level populations for this kind of plasmas. The first one is based on the solution of the radiation transfer equation (LTNEP code) and the second one on the escape factor formalism (M3R-EF code). In the LTNEP model a 1D plasma divided into N cells is considered, wach cell having a different density and temperature. The profiles of density and temperature are provided by hydrodynamic calculations as input for the model. Subsequently, the atomic kinetics and the radiation transfer equation are solved self-consistently for the whole plasma. The rate equations are solved in the Collisional-Radiative Steady State (CRSS) model, and the atomic processes included are the following: spontaneous emission, resonant emission and stimulated emission, photoionization and radiative recombination, collisional excitation and de-excitation, collisional ionization, and 3-body and dielectronic recombination.

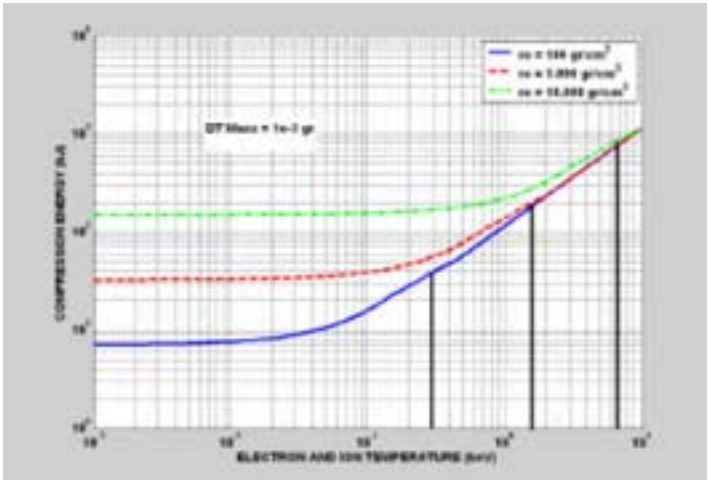

Figure 2. Electron compression (kJ) vs. electron and ion temperature for three different densities of compression from 100 (lower) to 10 000 g.cm^{-3} (upper).

The other model, the M3R-EF code, introduces reabsorption of the radiation through the escape factor formulism. The escape factor q denotes the mean probability that a photon emitted anywhere in the source will travel directly to the surface of the source in any direction and escape. In this work we have assumed a uniform distribution of emitting atoms and isotopic emission and a slab geometry [9]. The rate equations are also solved in the CRSS model, including the same atomic processes except resonant emission and photoionization. In both codes, the atomic data required for the calculations are provided as an input file, and the Stark profile is calculated by the Code Pim Pam Poum [10]. The source function is then obtained from the calculated line opacity, while the bound-free opacity is provided by hydrogenic formulas. Finally, the specific intensity is determined by solving the transfer equation with the known source function.

By using these two models we studied uniform aluminium plasmas with a length of 100 μm with regard to fixed electronic density (10^{23} cm^{-3}) and several temperatures (from 200 to 500 eV). It has been seen that for these plasmas self-absorption must be included because it introduces relevant changes in the level populations. For example, for the Lyman series we established that the ratio of the level populations calculated assuming optically thick and thin plasma, P_{thin}/P_{thick} , was equal to 10 for the ground states and 10^2 for the excited states, while for the Helium series it was equal to 1 and 10 respectively. Taking into account the results of the ratios of populations shown above and according to the relations between the populations and the source function, we established that the source function for optically thick plasmas was ten times greater than for the optically thin ones. We also verified that the escape factor formulism was a good alternative to these methods, based on the resolution of the rate equations coupled to the radiation transport equation for uniform plasmas, since LTNEP and M3R-EF codes provided similar results.

4. ACTIVATION OF MATERIALS: SAFETY AND ENVIRONMENTAL ISSUES

In the field of computational modelling for S&E analysis our main contribution refers to the computational system ACAB [11] which is able to compute the inventory evolution as well as a number of related inventory response functions useful for safety and waste management assessments. The ACAB system has been used by Lawrence Livermore National Laboratory (LLNL) for the activation calculation of the National Ignition Facility (NIF) design [12] as

well as for most of the activation calculations, S&E studies of the HYLIFE-II and Sombrero IFE power plants, with severe experimental testing at RTNS-II of the University of Berkeley [13] (see Figure 3). Pulsed activation regimes can be modelled (key in inertial confinement fusion devices test/experimental facilities and power plants), and uncertainties are computed in activation calculations according to cross section uncertainties. In establishing an updated methodology for IFE safety analysis, we also introduced time heat transfer and thermohydraulic calculations to obtain better estimates of radionuclide release fractions. Off-site doses and health effects are dealt with by using MACSS2 and developing an appropriate methodology to generate a dose conversion factor (DCF) for a number of significant radionuclides which cannot be dealt with by way of the current MACSS2 system. We performed LOCA and LOFA analyses for the HYLIFE-II design. The inherent radiological safety of the HYLIFE-II design relative to the use of Flibe was demonstrated. Assuming typical weather conditions, total off-site doses would remain below the 10-mSv limit. The dominant dose comes from the tritium in HTO form. In the Sombrero design, a severe accident, consisting of a total LOFA with simultaneous LOVA, was analysed. Key safety issues are the tritium retention in the C/C composite, and the oxidation of graphite with air, which should be prevented. The activation products from the Xe gas in the chamber are the source mainly contributing to the final dose leading to 47 mSv. We also analysed the radiological consequences and the chemical toxicity effects of accidental releases associated with the use of Hg, Pb, and Be, as IFE materials under the HYLIFE-II framework scenario. For those three materials, the chemical safety requirements dominate strongly over radiological considerations. Also, the role of clearance as waste management option for HYLIFE-II was explored. As regards the confinement building, which dominates the total volume of the waste stream, all material could be released from regulatory control for unconditional re-use after about one year of cooling following the plant shutdown.

We also explored liquid wall options for tritium-lean fast ignition IFE power plants. Many single, binary, and ternary molten-salts were evaluated for their S&E characteristics, as well as for the required pumping power. In analysing the impact of cross-section uncertainties in the contact dose rate from the activated concrete-gunite outer shell of the NIF reaction chamber, it was shown that current cross sections allow for reasonable confidence in the results.

Regarding IFE, uncertainties in the prediction of the neutron-induced long-lived activity in all natural elements showed that for the HYLIFE vessel a significant error was estimated in the activation of several elements, while the estimated errors in the Sombrero case were much less significant.

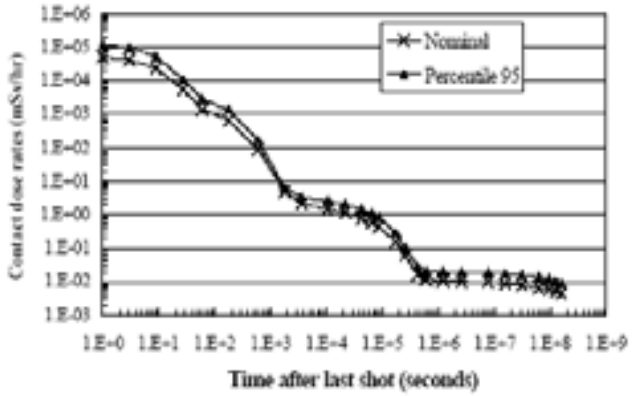

Figure 3. Nominal (without uncertainties) and 95% confidence interval in the contact dose rate from the activated NIF gunite shielding after thirty years of operation.

5. RADIATION DAMAGE OF FUSION MATERIALS

Ferritic-Martensitic steels (in their more advanced type using the experimentally tested Oxide Dispersion Strength, ODS, technique), composites, namely those based on SiC, and Vanadium alloys are the materials presently under discussion as structural materials, together with C, Be, W, as first wall materials and some ceramics (silica, alumina) as optical and insulator elements. A systematic experimental programme is being partially pursued in different countries to assess their performance under the specific conditions they will be working in. It is certain that a large and new irradiation facility is critically needed, and the International Fusion Materials Irradiation Facility (IFMIF) will cover this role. At present also Multiscale Modelling (MM) is playing a large role in obtaining predictive characteristic and defining the needed experiments. A common methodology work appeared not only on fusion programmes but also on other nuclear systems, such as fission (advanced Fission Reactors/Generation IV and Accelerator Driven Systems for Transmutation), with coincidents in some of the analysed materials. Of key value are the validation of MM against specific step-by-step experiments at the microscopic and macroscopic levels and the real understanding of damage processes and the effects of alloying and impurity elements. Microscopic parameters (using Molecular Dynamics, MD and DENIM models), which identify the effect of irradiation through the formation and diffusion of new defects, are being generated for some specific metallic materials (Fe, binary alloys FeCr, FeCu, V...), and their diffusion is being conducted by way of MonteCarlo [14]. The next step is their interaction with dislocations (Dislocation Dynamics) and the study of nucleation in the presence of He. That effect of He in FeCr alloys is certainly critical. We also derive macroscopic magnitudes, using small-scale MM models in short simulation times by using MD defect-dislocation studies under stress [15]. We modelled pulse radiation damage, and we progressed in the microscopic validation of Multiscale Modelling with experiments using pure and ultra-high pure Fe (effect of impurities) in a National Simulation-Experimental Programme using ion irradiation [14]. Our work is also concentrated on two IFE key materials (SiO_2/optics, SiC/low activation advance material). An MD *tight binding* scheme has been fully developed for β-SiC to understand the microscopic phenomena of its native defects and its diffusion at different temperatures. We reached an extraordinarily good agreement between our calculated energetic defects and the results obtained, using sophisticated and expensive methods such as *ab-initio* at 2000K. We observed that the β-SiC crystal remained perfectly in its typical cubic structure at that temperature, and we showed that the carbon atoms did not diffuse into the crystal. The self-interstitial silicon atom prefers the relation with atoms of the same species due to the fact that the repulsive force of silicon atoms is stronger than that of carbon atoms [16]. MD is also being used to study the defects produced in fused silica by energetic atoms and neutron and gamma irradiation.

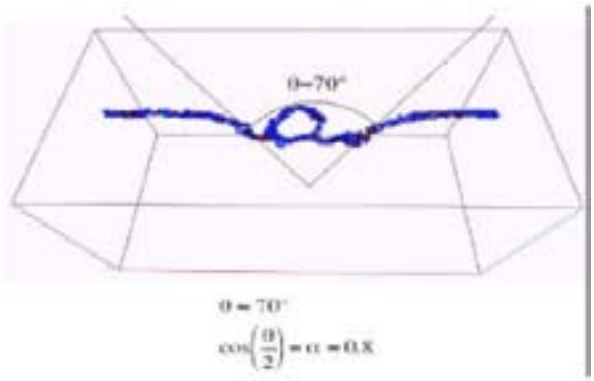

Figure 4. Molecular Dynamics: last temporal view before dislocation overpass of defect loop [100] with an angle of $\theta = 70°$*, which is the critical value to estimate the resistance of such an obstacle, set up to determine stress-strain characteristics of the material.*

We determined the structure factor, the bond angle distribution, co-ordination and ring statistics, and we concluded it to be in very good agreement with the measurements of the generation of fused silica glass [17] (see Figure 4). Threshold displacement energies were computed as a function of the direction of movement of the PKA, and cascades of 5 keV were actually extended to 10 keV. Two experimental modeling programmes have been started with CIEMAT for silica analysis and will in future be extended to alumina as first-wall and ceramics insulators.

6. ATMOSPHERIC DIFFUSION OF TRITIUM AND ENVIRONMENTAL PATHWAYS TO THE HUMAN CHAIN

A comprehensive and completely new work has been performed in the analysis of consequences of Tritium release relating to expected source emissions from IFE Conceptual Reactors and other nuclear systems [18]. The key aspect here is to consider all chemical forms of Tritium (HT and HTO), their conversion to Organically Bound Tritium (OBT) with soil processes, and the consequences of re-emission into the atmosphere. We reported several important conclusions on the primary and, in particular, secondary phases of Tritium transport in the environment, with a final consideration of different time-dependent phases in dosimetry. Our new approach allows a more realistic simulation and sets a significantly more restrictive limit on Tritium handling than traditionally assumed in conceptual systems. This methodology has been successfully applied in the work performed for establishing the Vandellós site for ITER (contract under EFDA). The entire study of secondary phase drives arrived at the conclusion that the behaviour of Tritium should be simulated using as a basis two well-differentiated methods, a deterministic and a probabilistic one.

Deterministic calculations are based on *a priori* fixed meteorological data giving wind speed and direction, the class of atmospheric stability and rain intensity, as well as the boundary conditions of the surroundings of the atmospheric discharge (soil type, air humidity, temperature and solar intensity). The probabilistic study is based on real meteorological analysis as measured every hour, and taking into consideration the probability that individuals can represent a dose for internal irradiation of the Tritium. It is our conclusion that these probabilistic studies provide the real dynamics of the processes, which are different from the deterministic aspect. The effect of the formation of OBT is considered to be of key importance.

ACKNOWLEDGEMENTS

Work was performed under the Spanish National Programme on Thermonuclear Fusion Projects FTN2001-3886-C02-01 and FTN2001-3886-C02-02, the European Union Keep-in-touch Program on IFE, and EFDA Tasks in Multiscale Modeling for Fusion (2003, 2004). There is good collaboration on IFE activities with the Lawrence Livermore National Laboratory and the University of Berkeley (USA), SCK-CEN Mol (Belgium), Edf and CEA (France), and the University of Cagliari (Italy). Work was also performed in collaboration with CIEMAT in CSN/UNESA VENUS-II (2000-2003) and the Spanish REVE Project (2004–2007).

REFERENCES

[1] P. VELARDE, F. OGANDO, S. ELIEZER, M. SAULE, *Proc 3rd IFSA* (2004) 88.
[2] F. OGANDO, P. VELARDE, JQSRT 71 (2001).
[3] M. MURAKAMI, HIF 2004 Conference, paper MI14 (2004).
[4] R. KODAMA et al., Nature **412** (2001) 798.
[5] S. ELIEZER, P.T. LEÓN, J.M. MARTÍNEZ-VAL, D. FISHER, Laser and Particle Beams, **21**, 599 (2003).
[6] P.T. LEÓN, S. ELIEZER, J.M. MARTÍNEZ-VAL, M. PIERA, Physics Letters A, **289**, 135 (2001).
[7] P.T. LEÓN, S. ELIEZER. J.M. MARTÍNEZ-VAL. M. PIERA, submitted to Laser and Particle Beams (2004).
[8] E. MÍNGUEZ, J.M. GIL, P. MARTEL, J.G. RUBIANO, R. RODRÍGUEZ & L. DORESTE (1998), Nucl. Instr. and Meth. in Phys. Res. A **415**, 539-542.
[9] R. MANCINI, R.F. JOYCE & C.F. HOOPER JR., (1987), J. Phys. B: At. Mol. Phys. **20**, 2975–2987.
[10] A. CALISTI, F. KHELFAOUI, R. STAMM, B. TALIN & R.W. LEE (1990), Phys. Rev. **42**, 5433–54440.
[11] J. SANZ, *ACAB, Activation Code for Fusion Applications: User's Manual V5.0*, Univ. Nacional Edu. Distancia (UNED). Inst. Fusión Nuclear DENIM 490, Feb. 2000; Lawrence Livermore National Laboratory, UCRL-MA-143238, Feb. 2000.
[12] J. SANZ et al., Fusion Science and Technology, **43** (2003) 473–477.
[13] J.F. LATKOWSKI, S. REYES, L.C. CADWALLADER, J.P. SHARPE, T.D. MARSHALL, B.J. MERRILL, R.L. MOORE, D.A. PETTI, R. FALQUINA, A. RODRIGUEZ, J. SANZ, O. CABELLOS, Fusion Science and Technology, **44** (2003) 34–40.
[14] J.M. PERLADO et al., Assessment of structural and silica materials under irradiation in inertial fusion reactors: comparison of multiscale modeling and microscopy, IFSA 2003, Elsevier Pub (2004).
[15] J. MARIAN, B. WIRTH, B. ODETTE, R. SCHAUBLIN, J.M. PERLADO, J. Nucl. Mat. **323** (2003) 181–191.
[16] M. SALVADOR, J.M. PERLADO, A. MATTONI, F. BERNARDINI COLOMBO, J. Nucl. Mat. **329-333** (2004) 1219–1222.
[17] F. MOTA, M.J. CATURLA, J.M. PERLADO, E. DOMÍNGUEZ, A. KUBOTA, J. Nucl. Mat. **329-333** (2004) 1190–1193.
[18] M. VELARDE, J.M. PERLADO, L. SEDANO, The role of organically bound Tritium after ingestion in normal and accidental scenarios caused by releases from inertial fusion reactors, IFSA 2003, Elsevier Pub (2004).

DRIVERS FOR IFE

HALNA DPSSL for inertial fusion energy driver

O. Matsumoto[1,2], T. Kanabe[4], R. Yasuhara[1,2], T. Sekine[1,2], T. Kurita[1,2], M. Miyamoto[1,2], T. Kawashima[1,2], H. Furukawa[3], H. Kan[2], T. Kanzaki[2], M. Yamanaka[1], T. Norimatsu[1], N. Miyanaga[1], M. Nakatsuka[1], Y. Izawa[1], S. Nakai[5]

[1] Institute of Laser Engineering, Osaka University, Osaka, Japan
[2] Hamamatsu Photonics K.K., Shizuoka, Japan
[3] Institute for Laser Technology, Osaka, Japan
[4] Graduate School of Engineering, University of Fukui, Fukui, Japan
[5] Kochi National College of Technology, Kochi, Japan

Abstract. We are developing a laser-diode-pumped Nd:glass water-cooled slab laser amplifier for an inertial fusion energy driver. A laser beam is propagated through a zig-zag slab four times on different optical paths on a round trip and is amplified. The laser system and optical elements, such as the laser glass with sol-gel anti-reflection coating and a serrated aperture, are described. The output of 10.6 J was attained at a rep. rate of 1 Hz. We evaluated the experimental output energy by comparing it with the calculated results.

1. INTRODUCTION

It is required of an inertial fusion energy (IFE) driver to provide several megajoules of pulse energy (four MJ at 350 nm) at the moderate rep. rate of 10 Hz with an overall efficiency of more than 10%. High-power laser diode arrays complement solid-state laser for the IFE driver with their compactness, brightness, high efficiency and long life. The latest modular architecture of the four MJ diode-pumped solid-state laser (DPSSL) driver consists of 400 modules of 10-kJ energy at 351-nm wavelength and 12-Hz rep. rate. Diode-pumped watercooled slab laser amplifiers compose the 15 beamlets of 1-kJ output each with multiple-beam phase-coupling, then the 1053 nm-output beams are up-converted to 351 nm. For the demonstration of HALNA (High Average-power Laser for Nuclear-fusion Application) we developed a small-scale test bed of the 10-J output Nd:glass DPSSL amplifier (HALNA-10), using the same design parameters as those of the HALNA-1k (1-kJ output), such as slab thickness, pump intensity, stored energy density and safety margin to thermal fracture. The HALNA-10 has achieved 8.5-J output per pulse at 0.5 Hz with 2 times diffraction-limited (TDL) beam quality [1].

On the basis of these results, we advanced a 10-Hz rep. rate experiment with the newly designed system. The four-pass zig-zag optical geometry consists of two symmetrical paths along the glass slab axis, made of ten diamonds in the slab. Laser-diode (LD) stacks with a pulse duration of 200 μs at 10 Hz pump the laser medium with 290-kW peak power at a wavelength of 803 nm. In this paper the development of HALNA-10 is reported on.

2. SYSTEM LAYOUT

The layout of the laser system is shown in Fig. 1. The laser system incorporates MOPA (Master Oscillator Power Amplifier) configurations. In order to extract energy from a laser medium efficiently, a zig-zag slab amplifier through which laser beam passes four times of

different optical path in round trip was adopted. A laser oscillator is formed by the single longitudinal and transverse-mode CW-diode-pumped Nd:YLF seed laser at 1053 nm and a diode-pumped Nd:YLF Q-switched slave oscillator.

We stabilized the oscillator by feedback algorithm, which made rise time of an oscillation waveform the minimum. The energy output of the oscillator was 1 mJ. The pre-amplifier was a diode-pumped Nd:YLF rod amplifier which amplified an oscillator output to 300 mJ. The laser beam pattern, which passed through a serrated rectangular aperture, was transmitted by relay imaging with spatial filters. The high spatial frequency components generated by thermal distortion of the laser glass were removed by pinholes in the spatial filters. A laser beam passed four times through the laser glass of the main amplifier on an optical zig-zag path. Between the second and third path it passed twice through a Faraday rotator with a 45° rotation. After passing twice through the Faraday rotator, the final output of s-polarization was reflected by a polarizer.

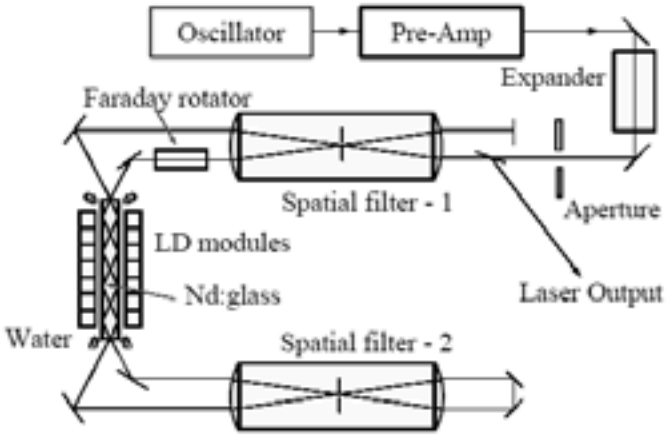

Figure 1. System layout.

The laser glass design was carried out in consideration of the damage threshold value, amplification characteristics and the prevention of parasitic oscillation. In our design, a laser beam is propagated through different optical paths on a round trip as shown in Fig. 1. As the stored energy changes in each region, it is necessary that the amplification on the next path is calculated after subtraction the energy extracted. After dividing the laser glass into segments, the output energy of each segment of the laser glass is calculated. We modified the Frantz-Nodvik equation[2] and the Eggleston-Frantz equation [3] to derive the equation of the laser pulse propagation in a laser medium. The output of 10 J may be obtained from the results of the calculations with a pumping energy of 48 J by LD modules. The pumping dimensions of the zig-zag slab are 268 mm length, 22 mm height and 10 mm width.

3. OPTICAL ELEMENTS OF A HIGH-AVERAGE AMPLIFIER

The design of a high-average output laser requires an estimate of the laser damage threshold of optical components. LD modules and the laser glass are contained in the laser head. The laser glass and the serrated aperture were examined with regard to laser damage.

Laser head

A photograph of the laser head is shown in Fig. 2. The laser head is equipped with LD modules and holds laser glass cooled by water flowing through the channel between the laser glass and a window sheet glass. The water coolant flows on the surface of the laser glass with a velocity of 1 m/s to reduce thermal effects on the laser glass. The LD stack element is composed of 100-W LD bars (Hamamatsu Photonics) at a wavelength of 803 nm. Cooling water is supplied from the backside of the LD bars. It pumps the laser glass with an output energy of 1 J, at a peak power density of 2.5 kW/cm^2 and a pulse width of 200 μs. Twenty-four stack elements are assembled into an LD module (FIG.3) which produces 120 kW peak power. Two sets of LD modules pump laser medium with a total energy of 48 J from the right and left side.

Figure 2. Laser head without LD modules.

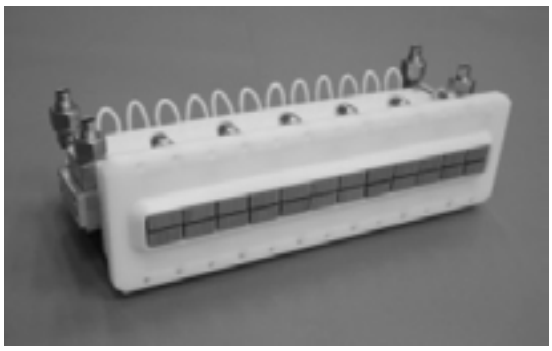

Figure 3. LD module.

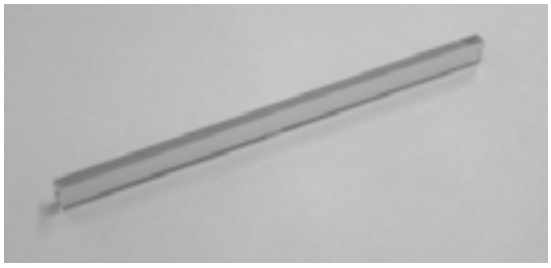

Figure 4. Laser glass with sol-gel AR coating.

Laser Glass

The laser medium is Neodymium-doped phosphate glass (HAP-4). The Nd doping level of HAP-4 is 1×10^{20} cm^{-3} and the stimulated emission cross-section is 3.6×10^{-20} cm^2. In order to obtain the output energy of 10 J at 10 Hz, we determined the size of the HAP-4 by the calculation of amplification and the simulation of thermal effects. The thin film for anti-reflection (AR) was formed on the entrance and exit faces of the laser glass by the sol-gel coating process. Figure 4 shows a photograph of the slab glass with sol-gel AR coating.

When ethyl-silicate solution is added to water, it changes to sol by a polycondensation reaction which starts with hydrolysis. A substrate is dipped into this sol solution and pulled up with constant speed, and the uniform thin film is coated by reacting sol on a substrate. Since the damage threshold power of thin sol-gel film is high, it excels as thin AR film of optical components of high-average output laser. Film thickness is adjusted by the pull-up speed of the substrate.

First of all, we designed the sol-gel AR coating of the one-layer film. The incident angle of the laser beam to the laser glass was 26°. In this case, in order to obtain the maximum transmissivity at a wavelength of 1053 nm, the maximum transmissivity at normal incidence had to be obtained by a wavelength of 1120 nm. Since the value of the refractive index of coating film is 1.29, film thickness was calculated to be 217 nm. When the incident angle in the calculation is 26°, the maximum transmissivity is 99.7% for a p-polarized beam and 99.9% for an s-polarized beam.

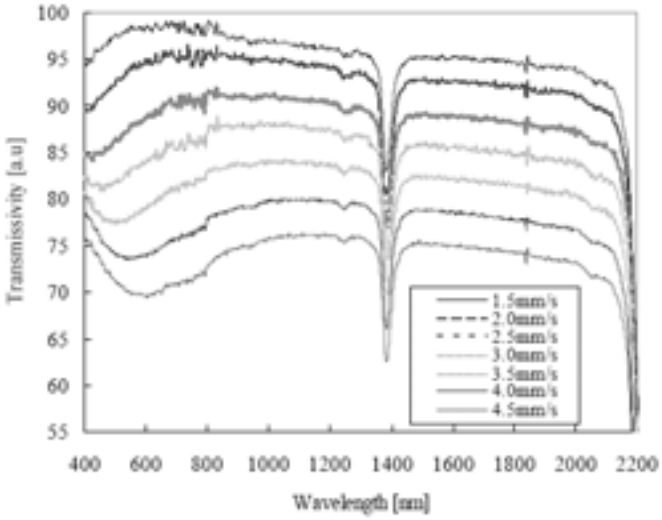

Figure 5. Spectral transmissivity of sol-gel film.

The pull-up speed of the laser glass was decided on the basis of an experiment. Changing pull-up speeds, we coated various thin sol-gel films on quartz glasses and measured their spectral transmissivity. Fig. 5 shows the result of the measurement of spectral transmissivity. The pull-up speed was evaluated from the relation between peak transmissivity and pull-up speed. When pull-up speed increases, it turns out that the peak value of transmissivity shifts to the longer wavelength. The approximation curve which expresses the relation between the peak wavelength and the pull-up speed is obtained from this result. The pull-up speed is 4.1 mm/s, which gives a peak wavelength of 1120 nm at normal incidence. We coated sol-gel film on the entrance and exit faces of the laser glass at an experimental pull-up speed of 4.1 mm/s. The measured reflectivity was 0.4% for an s-polarized beam and 0.2% for a p-polarized beam at 1053 nm at an incident angle of 26°.

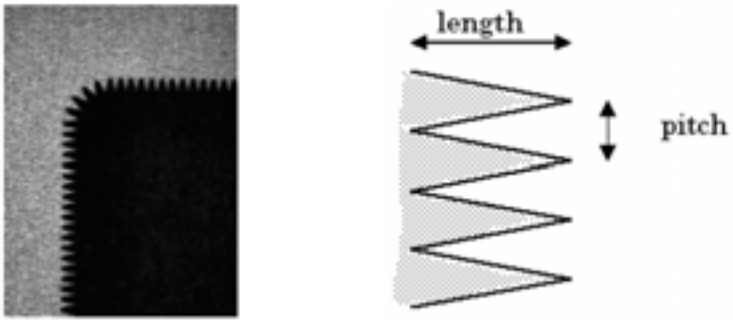

Figure 6. Serrated aperture (pitch: 0.3 mm, length: 0.6 mm).

Serrated aperture

The laser beam amplified by the pre-amplifier was expanded to an ellipse of 15 × 30 mm by the expander and was formed into a rectangular aperture. In order to obtain a uniform spatial

distribution, the serrated aperture was adopted as the rectangular aperture. The surrounding of the aperture was shaped into a saw-tooth form and achieved a uniform output beam [4] pattern. Laser processing, which is a simple and cheap method to make a serrated aperture, was adopted. In the laser processing, since part of the saw-tooth section did not have an acute angle on the material-processing side, the peak in intensity due to diffraction appeared in a beam pattern. In order to obtain a uniform beam pattern, we evaluated serrated apertures with different pitches and lengths of saw-teeth. As a result of this evaluation, we determined to use the serrated aperture with a pitch of 0.3 mm and a length of 0.6 mm. The partial picture and the spatial pattern of the aperture are shown in Figures 6 and 7.

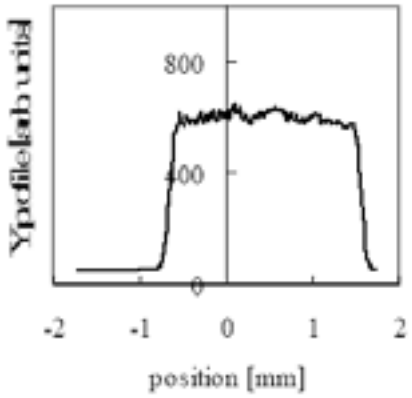

Figure 7. Spatial pattern of serrated aperture.

4. RESULTS OF EXPERIMENTS

Figure 8 shows a measured pumping profile which is an emitting pattern at the entrance face of the laser glass. It is obtained by an infrared camera. Although the pumping x-profile has a dent which was caused by the distribution of absorbed LD energy, the y-profile is rather uniform.

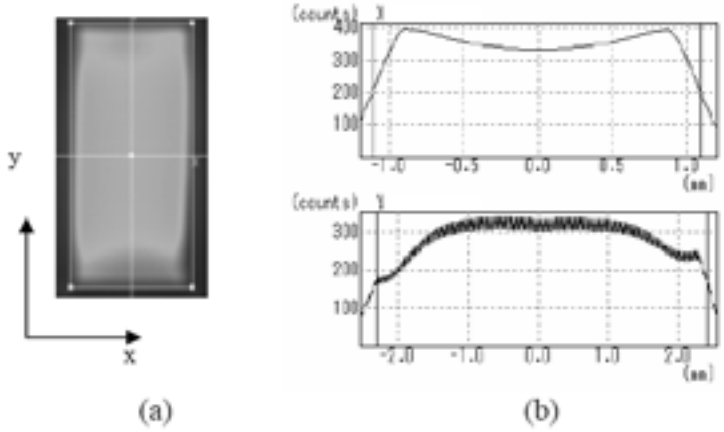

Figure 8. Spatial pattern (a), x and y profile (b).

Laser output energies of 10.6 J and 7.5 J at 1 Hz and 10 Hz, respectively, were achieved. Figure 9 shows the calculated results and a measured value of the 1 Hz operation. Compared to the calculated results, laser output energy is small. It is considered that the thermal lensing effect of the laser glass lowered the output energy. The estimated temperature increase was about 40°C at the 10 Hz operation. The extraction efficiency of 44% and the optical-to-optical conversion efficiency of 20% were measured at 1 Hz. Over 80% of the output energy was focused into the 5 TDL area without any wavefront correction.

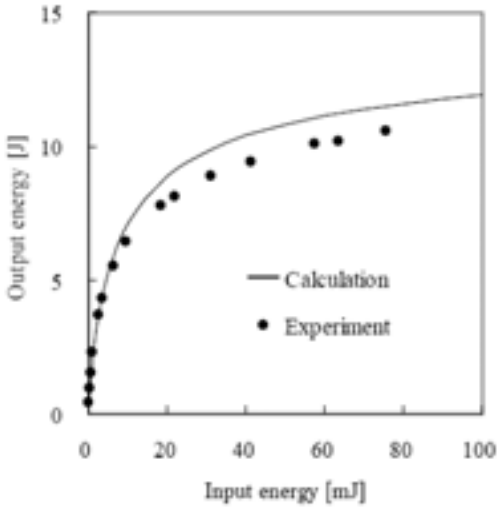

Figure 9. Calculated results and measured value of 1 Hz operation.

5. CONCLUSIONS

We described developments in the high-average power laser for the IFE driver. We adopted optical elements such as laser glass and the serrated aperture in consideration of laser damage. We coated sol-gel film on the entrance and exit faces of the laser glass for AR coating. The pull-up speed of the sol-gel coating was decided on the basis of an experiment. Measured reflectivity was 0.4% for an s-polarized beam and 0.2% for a p-polarized beam. In order to obtain a uniform spatial distribution, the serrated aperture was adopted as a rectangular aperture. We evaluated serrated apertures with different pitches and lengths of saw-teeth. Measured output energy was 10.6 J at 1 Hz and 7.5 J at 10 Hz. Compared to calculated results, laser output energy was low. It was considered that the thermal lensing effect of laser glass lowered the output energy. We are planning to advance our development of a 20 J at 10 Hz operation.

ACKNOWLEDGEMENTS

The authors thank Mr. H. Kitamura at the Institute of Laser Engineering, Osaka University, for technical instruction on the sol-gel AR coating process. Part of this research has been carried out under the project sponsored by NEDO (New Energy and Industrial Technology Development Organization) in Japan.

REFERENCES

[1] T. KAWASHIMA et al., Jpn., J. Appl. Phys. **40** (2001) 6415.
[2] L.M., FRANTZ and , J S. NODVIK, J. Appl. Phys., **34** (1963) 2346.
[3] J.M. EGGLESTON et al., IEEE, J. Quantum Electron., **25** (1989) 1855.
[4] Y. KITAGAWA et al., Annual Progress Report 2002, Institute of Laser Engineering, Osaka University (2002) 12.

Intense heavy ion and laser beams interacting with solid, gaseous and ionized matter

D.H.H. Hoffmann[1,2], A. Blazevic[2], P. Ni[2], O. Rosmej[1], M. Roth[2], N. Tahir[1], A. Tauschwitz[1], S. Udrea[2], D. Varentsov[2], K.Weyrich[1], Y. Maron[3]

[1] GSI-Darmstadt, Darmstadt, Germany
[2] Institut für Kernphysik , Technische Universität Darmstadt, Darmstadt, Germany
[3] Weizmann Institute of Science, Rehovot, Israel

Abstract. Interaction processes of heavy projectile-ions with solid and gaseous targets with a target thickness exceeding the ion stopping length were under theoretical and experimental investigation. The main goal of the current experiments is to understand the details of the energy deposition of the fast heavy ion penetrating solid matter [1]. This depends on the charge state distribution and velocity of the ion inside the target volume as well as on the target density.

For the first time the dynamic evolution of the projectile ion velocity inside extended solid targets was observed. K-shell projectile and target atom radiation spectroscopy in the photon energy region of 1.5–4 keV was applied to analyse the ion charge and velocity along the ion beam interaction path in extended solid targets [2]. The variation of the projectile Kα-satellite's Doppler shift due to the ion deceleration was used to measure with a spatial resolution of 50–70 mm the ion velocity over more than 1mm of the beam track. Aerogel targets of SiO_2 with a low mean density of 0.15 g/cm^3 allowed to extend the ion stopping length more than 10 times as compared to a solid quartz target, and it was therefore possible to increase the spatial resolution of the method. K-shell projectile spectra show the long lasting radiation of the highly charged Ca+17–Ca+19 ions down to the energies of 2 MeV/u. This is in disagreement with the measurements of the ion charge states distribution measured after their passing through solid carbon foils.

Intense heavy ion beams from the Gesellschaft für Schwerionenforschung (GSI-Darmstadt) accelerator facilities, together with two high-energy laser systems [3] (PHELIX: **p**etawatt **h**igh **e**nergy **l**aser for **i**on e**x**periments, and nhelix: **n**anosecond **h**igh **e**nergy **l**aser for **i**on e**x**periments), are a unique combination to facilitate pioneering beam-plasma interaction experiments [4], to generate and probe high-energy-density (HED) matter and to address basic physics issues associated with heavy ion-driven inertial confinement fusion. In one class of experiments the laser will be used to generate plasma and the ion beam will be used to study the energy loss of energetic ions in ionized matter, and to probe the physical state of the laser-generated plasma. In another class of experiments the intense heavy ion beam will be employed to create a sample of HED matter, and the laser beam, together with other diagnostic tools, will be used to explore the properties of these exotic states of matter [5, 6]. The existing heavy ion synchrotron facility, SIS18, delivers an intense uranium beam that deposits about 1 kJ/g of specific energy in solid matter. Using this beam, experiments have recently been performed where solid lead foils were heated and a brightness temperature of the order of 5000 K was measured, using a fast multi-channel pyrometer that has been developed jointly by GSI and IPCP Chernogolovka. It is expected that the future heavy ion facility, FAIR (Facility for Antiprotons and Ion Research), will provide compressed beam pulses with an intensity that exceeds the current beam intensities by three orders of magnitude. This will open up the possibility to explore the thermophysical and transport

properties of HED matter in a regime that is very difficult to access using the traditional methods of shock compression.

Inertial Fusion Energy requires intense laser or particle beams to heat matter to high temperatures in the order of 300 eV. Interaction processes of photons and ions with ionized matter are an important ingredient for the process of inertial fusion. For this reason, GSI as an accelerator laboratory for heavy ions takes specific interest in the investigation of interaction phenomena of heavy projectile-ions with ionized matter as well as solid and gaseous targets. Here we report about experiments where the target thickness exceeded the ion stopping length and thus the ions were fully stopped inside the target material, as shown in Fig 1, where an intense Ar-ion beam is stopped in a cryogenic Kr-crystal.

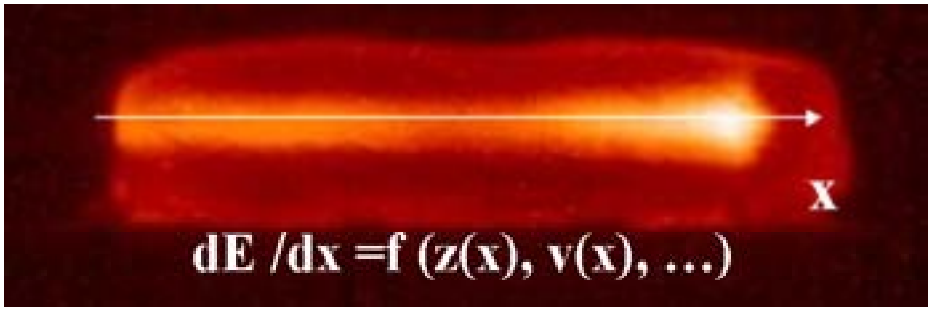

Figure 1. A 300 MeV/u Ar beam is penetrating into a Kr-crystal. The aim of the experiment is the investigation of the stopping process of ions inside matter and the determination of the dynamics of energy loss as a function of penetration depth and velocity.

The main goal of the current experiments is to understand the details of the energy deposition of the fast heavy ion penetrating solid matter [1]. This depends on the charge state distribution and velocity of the ion inside the target volume as well as on the target density. The availability of intense ion beams from the GSI accelerator, combined with improved spectroscopy methods, made it possible for the first time to observe the dynamic evolution of the projectile ion velocity inside extended solid targets. We measured the K-shell projectile and target atom radiation in the photon energy region of 1.5–4 keV. Due to the high spectral and spatial resolution we were able to analyse the ion charge and velocity along the ion beam interaction path in extended solid targets [2].

In Fig. 2 the principal setup of the experiment is shown. Ionization and electron capture processes led to the emission of characteristic radiation from target ions and atoms as well as from the projectile. Due to the high initial energy of 11.4 MeV/u the projectile velocity was approximately 10% of the speed of light in a vacuum. Under these conditions the relativistic Doppler-shift was observable also at observation angles perpendicular to the ion trajectory. The spatial resolution was 50–70 μm and we observed the ion penetrating almost 10 mm into the solid target. Moreover, we made use of the variation of the projectile Kα-satellite's Doppler shift due to the ion deceleration to determine the ion velocity as a function of penetration depth.

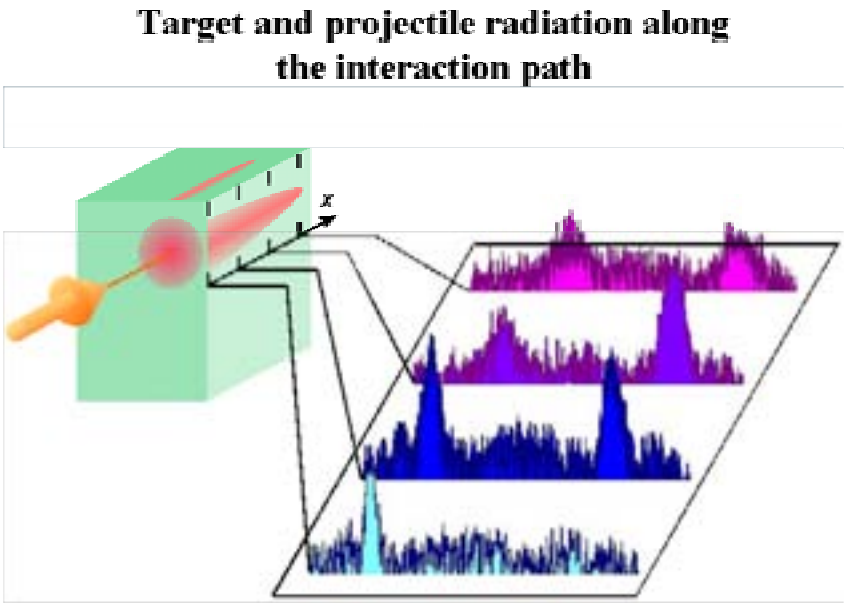

Figure 2. Along the interaction path the projectile and the excited target atoms or ions emit radiation, which is recorded with high spectral and spatial resolution.

Aerogel targets of SiO_2 with a low mean density of 0.15 g/cm^3 allowed to extend the ion stopping length more than 10 times as compared to a solid quartz target, and it was therefore possible to increase the spatial resolution of the method.

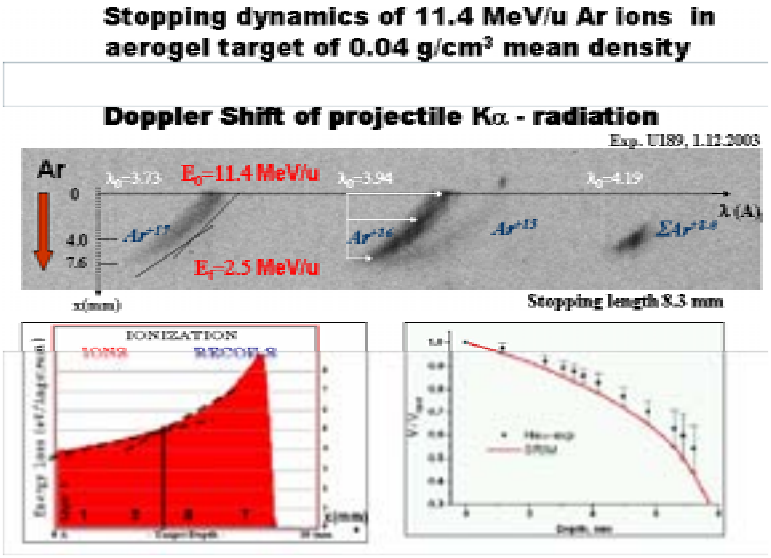

Figure3. The upper insert shows the radiation spectra Ar projectiles of different charge states from H-like (Ar+17), He-like (Ar16+) and Li-like (Ar15+) down to the radiation of the lower charge state ions, which are not resolved. The lower left insert shows the derived energy loss as a function of penetration depth, which is then compared to (lower left) standard stopping calculations.

In Figure 3, K-shell projectile spectra show the long lasting radiation of the highly charged Ar ions down to the energies of 2 MeV/u. The fact that the high-charge states are obviously

preserved down to very low energies is in disagreement with measurements of the ion charge state distribution measured after passing through solid carbon foils. In these measurements the charge state is measured with detectors far away from the last interaction process, whereas the current method allows to observe the charge state in situ. With these new measurements and the new technique it will be possible to address the question why the charge state distribution of ions measured behind a gaseous target or a solid foil are so different, while the specific energy loss does not differ significantly.

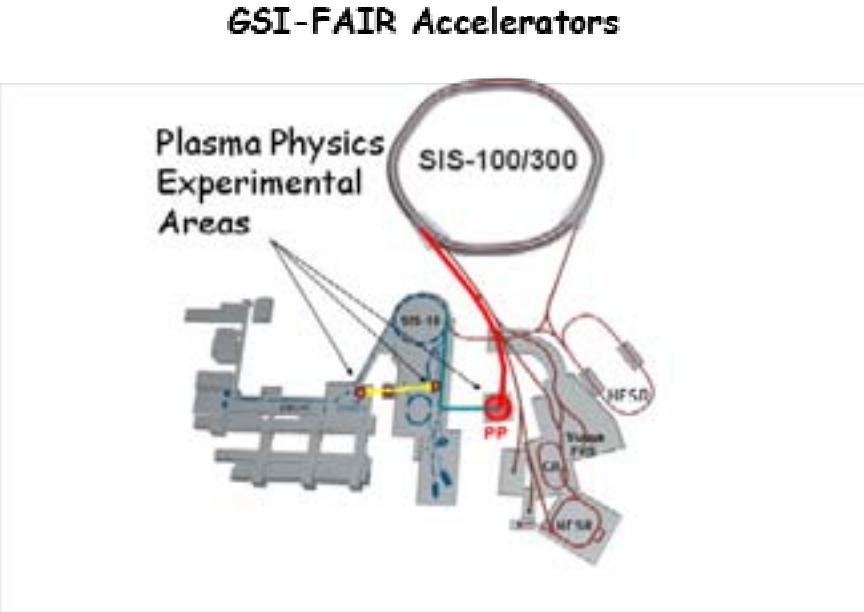

Figure 4. GSI accelerators and the experimental areas of plasma physics. The FAIR project at GSI will greatly improve the experimental option for beam-plasma experiments.

REFERENCES

[1] I.E. BAKHMETJEV et al., Research into the advanced experimental methods for precision ion stopping range measurements in matter. Laser Part. Beams 21, 1. (2003).

[2] O. ROSMEJ et al., Projectile spectroscopy of heavy ion beams. ECLIM 2004, Laser Part beams 23, (2005) in print.

[3] P. NEUMAYER, Invited talk ECLIM 2004, Laser Part. Beams 23, (2005), accepted for publication.

[4] D.H.H. HOFFMANN, K. WEYRICH, H. WAHL, D. GARDES, R. BIMBOT, C. FLEURIER, (1990). Energy loss of heavy ions in a plasma target. Phys. Rev. A42, 2313.

[5] N.A. TAHIR, S. SHUTOV, D. VARENTSOV, P. SPILLER, S. UDREA, D.H.H. HOFFMANN, I.V. LOMONOSOV, J. WIESER, M. KIRK, R. PIRIZ, V.E. FORTOV, R. BOCK, (2003). The influence of the equation of state of matter and ion beam characteristics on target heating and compression. Phys. Rev. Spec Top. 6, 020101.

[6] D. VARENTSOV, N.A. TAHIR, I.V. LOMONOSSOV, D.H.H. HOFFMANN, J. WIESER, V.E. FORTOV, Energy loss dynamics of an intense uranium beam interacting with solid neon for equation of state studies. Euro Phys. Lett. 64, 57.

High-quality return relativistic electron beam by intense laser pulse in a low-density foil plasma

B. Li[1], S. Ishiguro[2], M.M. Skoric[3], T. Sato[4]

[1] Institute of Applied Physics and Computational Mathematics, Beijing, China
[2] The Graduate University for Advanced Studies and National Institute for Fusion Science, Toki, Gifu, Japan
[3] Vinca Institute of Nuclear Sciences, Belgrade, Serbia and Montenegro
[4] Earth Simulator Center, JAMSTEC, Yokohama-shi, Japan

Abstract: Electron acceleration by intense laser beam interaction with an under-dense plasma layer was examined by particle simulations. A novel phenomenon of short high-quality, well-collimated return relativistic electron beam was observed in the direction opposite to laser propagation. The formation of an electron beam, its characteristics and the time-history of test electrons were illustrated and analyzed. A novel two-phase electron acceleration mechanism - the initial stage induced by forward stimulated Raman scattering and the second one by the buildup of a large sheath electrostatic field, which operates like a two-stage accelerator - was proposed.

Research on particle acceleration, which is based on an intense laser pulse interacting with a plasma, has recently received much attention due to the advent of short-pulse, high-intensity lasers. Great efforts have been invested in theoretical analysis, particle simulations and experiments, as high-quality high-energy particle beams have wide potential applications, for instance, in the fast ignition of inertial confinement fusion targets [1], laser induced nuclear reactions [2], radiography, etc. Up to now, various concepts of laser acceleration in a plasma, such as the beat-wave accelerator [3, 4], the laser wakefield accelerator [5], the electron beam wakefield accelerator [6] and the plasma accelerator of photon beams [7], are presently under discussion and investigation as possible approaches to acceleration to ultra-high energies. Stochastic heating and acceleration of electrons by two counter-propagating laser pulses were also studied by some authors [8, 9].

When an intense laser pulse propagates in an underdense plasma by nonlinear laser-plasma processes, such as forward stimulated Raman scattering (F-SRS) or a beat-wave scheme, which requires two laser beams and a plasma frequency precisely tuned to their frequency difference, etc., a large-amplitude electron plasma wave (EPW) can be excited behind the front of the laser pulse. The large-amplitude EPW has a very high phase velocity close to the group velocity of a laser pulse and can be used to accelerate electrons and consequently protons or ions to high relativistic energies.

In this paper, electron acceleration to relativistic electron energies by intense laser pulse interacting with an under-dense plasma layer in a vacuum is examined by particle-in-cell (PIC) simulations. The standard dephasing limit is briefly discussed. A new phenomenon of acceleration of a short, high-quality, well-collimated relativistic return electron beam with thermal energy spread was observed in the direction opposite to laser propagation. This novel mechanism operates like a two-stage accelerator. In the first phase, rapid electron acceleration by the relativistic EPW, induced by forward stimulated Raman scattering (F-SRS), allowed a massive initial electron blow-off into a vacuum region. Large ES Debye sheath fields were built spontaneously at two vacuum boundaries that further strongly accelerated electrons (second stage) to ultra-relativistic beam energies. The influence of ion dynamics will also be briefly discussed.

The fully relativistic electromagnetic (1D3V) EM PIC code (all quantities depend on the x-coordinate and on the time, and the particle momenta have three components) was used. The length of a simulation system and plasma was 5000 c/ω_0 and 1000 c/ω_0, where c and ω_0 was the speed of light and the carrier frequency of a laser pulse in a vacuum, respectively. The plasma density was $n = 0.01 n_{cr}$, which means $\omega_0/\omega_p = 10$, where ω_p was the electron plasma frequency, $n_{cr} = \omega_0^2 m_e \varepsilon_0 / e^2$ the critical density of a laser pulse. The electron temperature was $T_e = 1 keV$. At the front and rear side of the plasma, there were two $2000\, c/\omega_0$-long vacuum regions. The number of cells was 10 per $1\, c/\omega_0$ with 100 electrons in one cell, and ions were kept immobile as a neutralizing background. The linearly polarized laser pulse with the electric field E_0 along the y-direction, with the normalized amplitude $a = eE_0/(m_e \omega_0 c)$, was launched at $x = 1500\, c/\omega_0$, where e and m_e were the electron charge and mass, respectively.

The electrons were accelerated by F-SRS which was blown-off into a vacuum to build a potential charge separation barrier preventing more electrons to leave the plasma. For fast escaping electrons, as well as for EM waves, two extra numerical damping regions at both ends of the system were used. The time, electric field and magnetic field were normalized to $2\pi/\omega_0$, $m_e \omega_0 c/e$ and $m_e \omega_0 / e$, respectively; the time was taken as zero, $t = 0$ when a laser pulse arrived at the front (left) vacuum-plasma boundary.

In order to study electron acceleration, four different simulation runs have been presented, varying the laser amplitude a. The maximum momentum and energy obtained by electrons after the breaking of large-amplitude EPW are given in Table 1.

Table 1. Simulation results for different plasma length L and laser amplitude a; I stands for laser intensity for $1\,\mu m$ laser light, $p^{\max}$ and $E^{\max}$ stand for the maximum momentum and energy gained by electrons, respectively.

Simulation No	1	2	3	4
$L(c/\omega_0)$	1000	1000	1000	1000
a	0.5	1.0	2.0	3.0
$I(10^{18} W/cm^2)$	0.35	1.37	5.49	12.4
$p^{\max}/m_e c$	6	91	219	246
$E^{\max}(MeV)$	3	46	112	126

In the cases of laser amplitude $a = 0.5$, 1.0, 2.0 and 3.0, the maximum momentum obtained by electrons is $p^{\max}/m_e c \approx 6$, 91, 219 and 246, while the corresponding maximum electron energy is $E^{\max} \approx 3$, 46, 112 and 126, respectively. The maximum energy was found to increase at higher laser amplitudes. A free electron interacting with a plane EM wave (laser field) acquires an energy equal to $E_e = m_e c^2 a^2/2$; e.g., $a = 2$, $E_e \approx 1.0 MeV$. Accordingly, we cannot expect highly energetic electrons to be directly accelerated by an ultra-intense laser EM field.

For the laser pulse parameters used, the normalized amplitude was of the order of unity, the pulse length was several plasma periods and the laser frequency was several times the plasma frequency. In such conditions, the laser-plasma interaction is defined by the self-modulated regime, in one-dimensional limit, it is dominated by F-SRS instability [10]. F-SRS modulates

the intense laser pulse at the plasma frequency with a corresponding modulation of the plasma density. The resulting large EPW grows until it reaches the wave-breaking limit, after which large numbers of background electrons are self-trapped and accelerated to high energies.

The large-amplitude EPW is with a phase velocity $\upsilon_p \approx \upsilon_g$, so the Lorentz factor is $\gamma_p = (1-\upsilon_p^2/c^2)^{-1/2} \approx (1-\upsilon_g^2/c^2)^{-1/2} \approx \omega_0/\omega_p$, where υ_g and υ_p are the corresponding group velocity and phase velocity of a laser pulse, respectively. According to ref. [4], in the two-dimensional cold plasma theory, the critical amplitude of EPW is determined by the wave-breaking limit (standard dephasing limit); the maximum energy of an electron trapped by the potential of a relativistic EPW is given by $E^{\max} = 2\gamma_p^2 m_e c^2$. By taking the used parameter $\omega_0/\omega_p = 10$ gives $E^{\max} = 102MeV$. From Table 1 we can see that in two cases, higher laser amplitude cases $a = 2$ and 3.0, the standard dephasing limit $E^{\max} = 102MeV$ is exceeded. In recent years great efforts have been made to understand how the maximum energy can exceed the standard dephasing limit $E^{\max} = 2\gamma_p^2 m_e c^2$ [9, 11–13].

We leave now the dephasing limit problem; our goal is to focus on a new phenomenon, i.e, the generation of a high-quality, well-collimated return highly relativistic electron beam.

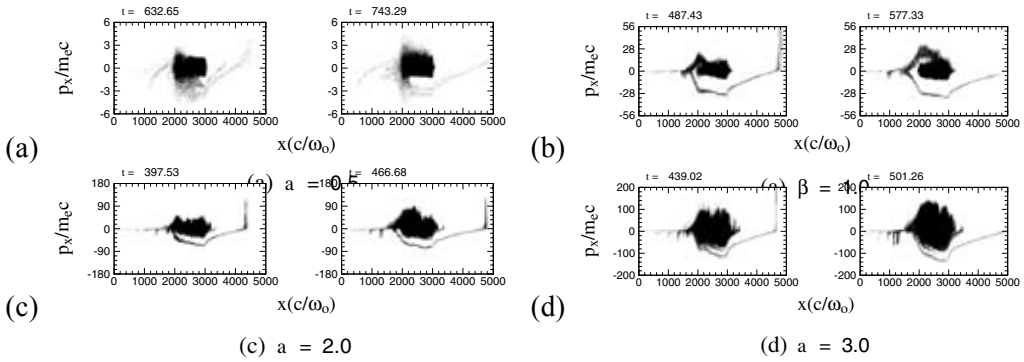

Figure 1. Electron phase-space $x \sim p_x$ snapshots for plasma density $n = 0.01 n_{cr}$ and laser amplitudes (a) $a = 0.5$*, (b)* $a = 1.0$*, (c)* $a = 2.0$*, and (d)* $a = 3.0$*, respectively.*

In Figure 1, electron phase-space snapshots for four simulations with laser amplitudes $a = 0.5$, 1.0, 2.0 and 3.0, are plotted. One can see that, except in the $a = 0.5$ case, in the direction opposite to the laser propagation, during some time interval the phenomenon of a short high-quality and well-collimated return relativistic electron beam can be observed in the electron phase-space. We also found that, when the laser amplitude is between $a = 1.0$ and 2.0, the quality of the return relativistic electron beam is better than in other cases for our simulation parameters. As an example, we now concentrate on the laser amplitude $a = 1.0$ to study and explain the details of the generation of a pulsed high-quality well-collimated return relativistic electron beam.

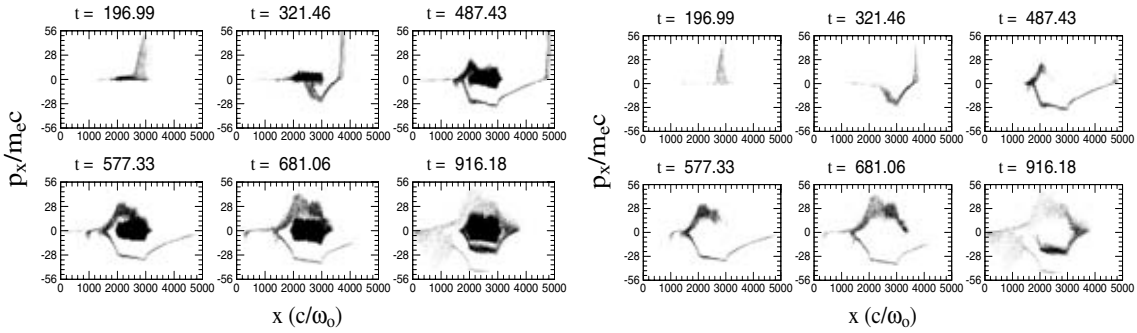

Figure 2. The electron phase-space $x \sim p_x$ snapshots for total electron momentum (left) and test electrons momentum (right), respectively.

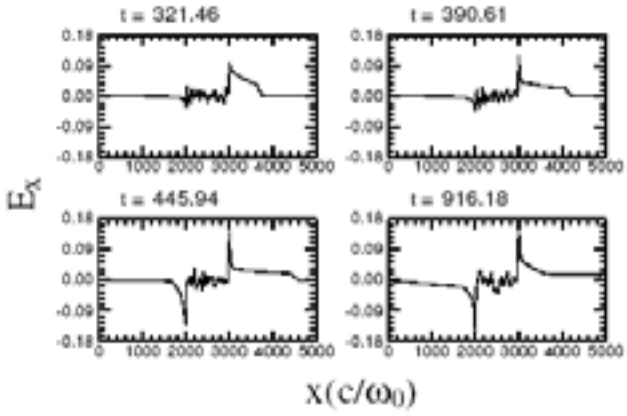

Figure 3. The ES field snapshots (E_x is normalized to $m_e\omega_0 c/e$) from the 1D-PIC simulation.

In Figure 2 (left) for the electron phase-space snapshots, the processes of electron acceleration can be seen directly. At an early stage, background electrons start to interact with a forward propagating relativistic EPW and are accelerated to large positive momenta p_x. The accelerated electrons move forward to the rear plasma-vacuum boundary and escape from the plasma layer into the vacuum region to build a potential barrier due to charge separation. As shown in Fig. 3, a large sheath ES field is quickly formed, its structure gradually decreasing into the vacuum region. The accelerated electrons entering this region experience deceleration, to be eventually stopped. Further, these electrons reverse their motion to be accelerated backwards into the bulk plasma. However, some ultra-fast electrons overcome the potential barrier and eventually become lost in the numerical-damping region which we introduced.

The electrons which are accelerated backwards through the bulk plasma are out of phase with the counter-propagating large EPW and will travel without much interaction toward the front plasma-vacuum interface. As time progresses, eventually a high-quality and well-collimated relativistic electron beam bunch will be formed. When these electrons pass through the front plasma-vacuum boundary into a vacuum region, again they first experience deceleration and then reverse motion by a repulsive charge separation potential. As a result, most of the electrons return into the bulk plasma to be again accelerated forward, to the rear plasma boundary. However, in the meantime, the relativistic electron beam will gradually separate from the rest of the beam due to the interaction of the beam electrons with the bulk plasma. Since the sheath ES field at the plasma-vacuum boundary still exists, electrons which arrive at the rear side experience the same process as before. Moving back and forth, energetic

electrons will re-circulate through the bulk plasma. In time, due to electron beam interaction with the bulk plasma, the relativistic beam features will eventually be lost and mixed with the rest of the heated bulk plasma.

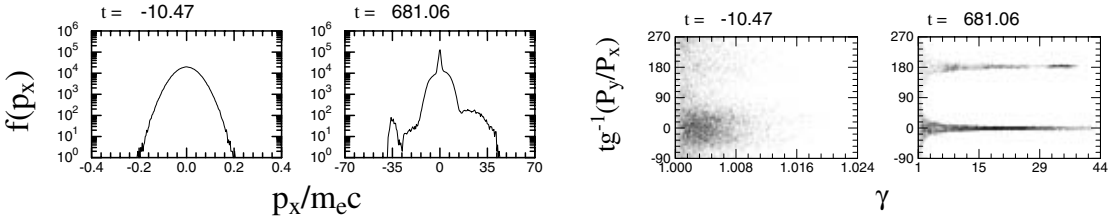

Figure 4. The snapshots for longitudinal momentum distribution (left) and angular energy-distribution $\gamma \sim \tan^{-1}(p_y / p_x)$ *(right), respectively.*

Figure 4 (left) shows the snapshots for electron longitudinal momentum p_x distribution. The peaked distribution in the second plot indicates that the high-quality well-collimated return relativistic electron beam is formed as the accelerated electrons are reflected and pulled back into the bulk plasma from the rear plasma-vacuum interface, i.e, in the opposite direction to the laser propagation, as is characterized by the peak around $p_x / m_e c \approx -35$.

One can see this process more clearly by taking the time interval between $239 \le t \le 955$ (corresponds to start and end of the pulsed electron beam) and selecting as test electrons those having negative momenta between $-20 \le p_x / m_e c \le -90$. About 1.3% of the total number of electrons satisfy these two conditions. By introducing test electrons we can easily trace back their earlier time history and vice versa. In Fig. 2 (right) the test electron phase-space snapshots are given. A picture of electron acceleration, deceleration, forward and backward motion, etc., is clearer.

As shown in Fig. 4 (right), for the angular energy distribution $\gamma \sim \tan^{-1}(p_y / p_x)$ of test electrons the initial number of electrons to be accelerated, which has angular energy distribution $-90^0 \sim 90^0$ (moving forward, initially) is greater than that of $90^0 \sim 270^0$ (moving backward, initially). When accelerated in time, the electron angular distribution is mostly concentrated around two angles, 90^0 and -270^0, that is, $|p_x| >> |p_y|$; indeed, it demonstrates that electrons are accelerated mainly by the longitudinal field.

In order to better visualize this, electron orbits in the phase space are shown for two-test electrons out of all the accelerated electrons. The time history of orbits $x(t)$ and momentum $p_x(t)$ is plotted in Fig. 5. The scenario seen is consistent with our discussions. Moving back and forth, fast energetic electrons re-circulate through the bulk plasma.

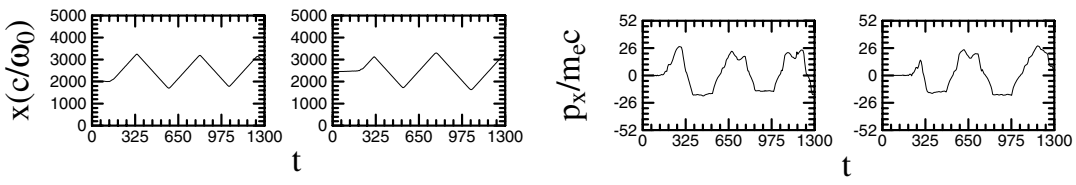

Figure 5. The time history of orbits $x(t)$ *(left) and longitudinal momentum* p_x *(right) for two representative test electrons.*

Based on these results, we propose that above novel relativistic electron acceleration by intense laser interacting with under-dense foil plasma when SRS takes place, can be divided into two phases: the initial rapid electron acceleration by F-SRS and the second electron acceleration due to large sheath ES fields at the rear plasma vacuum boundary. The second phase results in the formation of a high-quality well-collimated return relativistic electron beam. This two-phase electron acceleration operates just like a two-stage accelerator.

Why can this sort of high-quality and well-collimated relativistic electron beams be efficiently formed at appropriate laser amplitudes, e.g., $a = 1 \sim 2$? This result appears to stem from a synchronism and positive feedback between the electron acceleration and the sheath ES field formed at the rear vacuum boundary. Possibly, at lower laser amplitudes the absence of massive electron acceleration by F-SRS forms a low sheath ES field which changes slowly; the proper conditions for the generation of a high-quality relativistic electron beam are not met. Furthermore, in simulations for plasma density $n = 0.01 n_{cr}$ and ion mass $M_{ion} = 1836 m_e$, the ion plasma wave period is $T_{ion} \approx 43 T_p = 430 T_0$, where T_p and T_0 are the electron plasma period and laser pulse period, respectively. The total simulation time is about $t \approx 1300 T_0 \approx 3 T_{ion}$. Therefore, it appears plausible to neglect the ion dynamics, specially in the formation of the short well-collimated relativistic electron beam. Additional PIC runs with moving ions have proved that above assertion is correct.

In conclusion, we presented the novel mechanism for relativistic electron acceleration by intense laser pulse interacting with a thin low density foil plasma, discovered by way of 1D-PIC simulations. The standard dephasing limit and the electron acceleration process were discussed. A new phenomenon of a pulsed high-quality well-collimated return relativistic electron beam with thermal energy distribution, in the opposite direction of laser propagation, was proposed [14]. The mechanism of the beam formation, beam characteristics and the time-history in the *(x- p{x})* phase space for test electrons in the beam were analyzed and clarified. It operates like a two-stage accelerator: In the initial phase rapid electron heating in the F-SRS driven relativistic plasma wave allows a massive initial electron blow-off into a vacuum. Large ES Debye sheath fields are created to further accelerate electrons (second stage) to ultra-relativistic beam energies. For example, in a 160 microns long, $0.01 n_{cr}$ under-dense foil plasma illuminated by a laser at $10^{19} W/cm^2$, the maximum electron energy exceeding 120 MeV is obtained. The influence of ion dynamics was also briefly discussed. Finally, our results are expected to be of a particular relevance for a type of exploding foil laser-plasma experiments and simulation works [15, 16].

Some of us acknowledge support: (Baiwen Li) of the National Natural Science Foundation of China, Project No. 10445003 and (M.M.S.) of the Ministry of Science and Environmental Protection of the Republic of Serbia, Project No. 1964.

REFERENCES

[1] M. TABAK et al., Phys. Plasmas 1, 1626 (1994).
[2] P.L. SHKOLNIKOV et al., Appl. Phys. Lett. 71, 3471 (1997).
[3] C.E. CLAYTON et al., Phys. Rev. Lett. 70, 37 (1993).
[4] T. TAJIMA, J. M. DAWSON, Phys. Rev. Lett. 43, 267 (1979).
[5] P. SPRANGLE et al., Phys. Rev. Lett. 69, 2200 (1992); E. Esarey et al., Phys. Fluids B 5, 2690 (1993); T. M. Antonsen and P. Mora, Phys. Rev. Lett. 69, 2204 (1992).

[6] P. CHEN et al., Phys. Rev. Lett. 54, 693 (1985); J. D. Miller et al., Phys. Rev. Lett. 67, 1747 (1991).
[7] S.C. WILKS et al., Phys. Rev. Lett. 61, 337 (1988); S.C. Wilks et al., Phys. Rev. Lett. 62, 2600 (1989).
[8] J.T. MENDONCA, F. DOVEIL, J. Plasma Phys. 28, 485 (1982); J.T. Mendonca, Phys. Rev. A 28, 3592 (1983).
[9] Z-M. SHENG et al., Phys. Rev. Lett. 88, 055004 (2002); G. Shvets et al., Phys. Rev. Lett. 81, 4879 (1998).
[10] W.B. MORI et al., Phys. Rev. Lett. 72, 1482 (1994); W.B. Mori, IEEE J. Quantum Electron. 33, 1942 (1997); E. Esarey et al., Phys. Rev. Lett. 72, 2887 (1994).
[11] A. TING et al., Science 273, 472 (1996); R. Wagner et al., Phys. Rev. Lett. 78, 3125 (1997).
[12] K.C. TZENG et al., Phys. Rev. Lett. 79, 5258 (1997); D. Gordon et al., Phys. Rev. Lett. 80, 2133 (1998).
[13] E. ESAREY et al., Phys. Rev. Lett. 80, 5552 (1998).
[14] LI BAIWEN, S. ISHIGURO, M.M. SKORIC, H. TAKAMARU, T. SATO, Laser and Particle Beams, 22, 307 (2004).
[15] A.J. MACKINNON et al., Phys. Rev. Lett., 88, 215006 (2002).
[16] G. MALKA et al., Phys. Rev. Lett. 78, 3314 (1997); J.J. SANTOS et al., Phys. Rev. Lett. 89, 025001(2002); S.P. HATCHETT et al., Phys. Plasmas 7, 2076 (2000); C. ROUSSEAUX et al., Phys. Plasma, 9, 4261 (2002); Y. SENTOKU et al., Phys. Rev. E 65, 046408 (2002).

Generation of intense fast proton streams with the use of a picosecond high-power laser interacting with a double-layer foil target

J. Badziak[1], H. Hora[2], J. Krása[3], L. Láska[3], P. Parys[1], K. Rohlena[3], J. Wolowski[1]

[1] Institute of Plasma Physics and Laser Microfusion, Warsaw, Poland
[2] Dept. of Theoretical Physics, University of New South Wales, Sydney, Australia
[3] Institute of Physics, A.S.C.R., Prague, Czech Republic

Abstract. In recent works some useful aspects of fast ion emission from plasma produced with the use of high power laser generating ultrashort pulses have been emphasized. In particular, the possibility of applying laser-produced intense high-energy ions in inertial fusion has been suggested. In this paper our recent studies on fast proton generation in the plasma produced by an intense 1-ps laser pulse, carried out at the Institute of Plasma Physics and Laser Microfusion (IPPLM), Warsaw, are presented. The characteristics of ion fluxes emitted forward from various kinds of single- and double-layer targets were measured with the use of ion collectors and an electrostatic ion-energy analyser. The amplitudes of the hard X-rays emitted from the plasma were measured with the use of semiconductor detectors. Our experiments showed that a double-layer system makes it possible to obtain higher energies and higher proton current densities than single-layer systems. The mechanisms of proton acceleration and the possibility of production of picosecond proton beams of ultrahigh current densities, useful for inertial fusion, are discussed in the paper.

1. INTRODUCTION

The rapid development of high-peak-power lasers generating short (≤1ps) pulses (SPs) opened principally new possibilities of applications of ion beams emitted from laser-produced plasmas. Unlike large long-pulse (ns or subns) laser installations, a short-pulse laser (SP-laser), even of low energy (≤1J), makes it possible to produce very high laser intensities and, as a result, to generate intense high-energy ion bursts of ions of subnano- or picosecond duration [1, 2], which are not achievable by other currently known sources. This feature creates a prospect of different unique applications of SP-laser-driven ion beams, in particular, in inertial confinement fusion (ICF) research and high energy-density physics. However, besides the short ion pulse duration, these applications require also extremely high ion current densities, in some cases surpassing 10^{10}A/cm^2 [2–4]. Such ion current densities are attainable with a target normal sheath acceleration (TNSA) mechanism [1, 5] using relativistic laser intensities and curved targets enabling ballistic focusing of laser-driven ion beams [2, 5].

Just recently, we have proposed and demonstrated another method which makes it possible to produce ion beams of very high current densities in a planar geometry at subrelativistic laser intensities and at a low energy (≤1J) of the laser pulse [6, 7]. This method – referred to as skin-layer ponderomotive acceleration (S-LPA) – uses ponderomotive forces induced at the skin-layer interaction of a short laser pulse with a proper preplasma layer produced by a laser prepulse in front of a solid target. In this paper, we examine the influence of target structure on the current densities and energies of fast protons produced by the S-LPA mechanism at laser intensities ~10^{17} W/cm^2. Results of our measurements are compared to those obtained from the recent short-pulse experiments using the TNSA mechanism at relativistic laser intensities (~10^{20} W/cm^2).

2. THE S-LPA MECHANISM OF FAST ION GENERATION

In the S-LPA method [6, 7], an essential role is played by a thin preplasma layer (at a thickness of L_{pre} at least several times smaller than the laser focal spot diameter d_f) produced by the laser prepulse in front of a solid target. The main short laser pulse interacts most intensely with the plasma in the skin layer near the surface of the critical electron density, n_{ec}, and the geometry of the interaction is almost planar ($L_{pre} << d_f$). The high plasma density gradient in the interaction region induces two opposite ponderomotive forces acting – at the laser beam incidence perpendicular to the target surface – nearly parallel to the target normal. These forces break the plasma near the critical surface and drive two thin plasma blocks towards the vacuum and the plasma interior, respectively. The block area is approximately equal to the laser focal spot area: $S_{bl} \approx S_f$, and the block thickness $L_{bl} \approx S\lambda$, where $S = (1/|n|) \geq 1$ is the dielectric swelling factor (n is the plasma refractive index, λ is the laser wavelength). As the density of the plasma blocks is high (the ion density $n_i \approx n_{ec}/z$, where z is the ion charge state), even at moderate ion velocities $v_i \sim 10^7$–10^8 cm/s, the ion current densities $j_s = zen_iv_i$ can be very high (~10^9–10^{10} A/cm^2 or higher). The time duration of the ion current flowing out of the interaction region (which functions as the ion source) is approximately equal to the laser pulse duration. Due to an almost planar acceleration geometry, the angular divergence of the ion beam is small.

For subrelativistic laser intensities: $I << I_{rel} \approx 4.1 \times 10^{18}/\lambda^2$ [W/cm^2, μm], the ion energies, E_i, and the ion current densities, j_s, of the plasma blocks can be estimated from the following equations [6]:

$$E_i \approx 0.93 \times 10^{-16}\, s\, z\, I\, \lambda^2, \quad [\text{keV, W/cm}^2, \mu\text{m}] \tag{1}$$

$$j_s \approx 74\, (s\, z/A)^{1/2}\, \lambda^{-1}\, I^{1/2}, \quad [\text{A/cm}^2, \mu\text{m, W/cm}^2] \tag{2}$$

where s = S for the forward-accelerated ions and s = S – 1 for the backward-accelerated ions, and A is the atomic mass number. The swelling factor S essentially depends on the plasma density gradient and at very steep density gradients S ≈ 1 [8]. As it can be seen from (1) and (2), at S = 1 only a forward-accelerated ion beam is produced and the forward-directed ponderomotive force becomes the usual light pressure. In such a case, for instance, a 1-μm laser pulse of intensity 10^{17} W/cm^2 produces a ~ 10-keV proton beam of the current density $j_s \approx 23$ GA/cm^2. The optimum plasma density gradient results in a significant increase of both the proton energies and the proton current densities [8].

To estimate the fast ion current density at the source (in the close vicinity of the target surface) on the basis of measurements (e.g. the time-of-flight measurements) we can use the expression [6, 7]:

$$j_s \approx Q_i/\tau_{is}S_s, \tag{3}$$

where: Q_i – the total charge of fast ions measured in the far expansion zone; τ_{is} – the duration of fast ion generation at the source, which is roughly equal to the laser pulse duration, $\tau_{is} \quad \tau_L$ [2, 5]; S_s – the area of the fast ion source. In general, $S_s \geq S_f$ (S_f is the laser focal spot area), and, e.g. for the TNSA method, S_s can be even ten times larger than S_f [9, 10]. However, as it was mentioned earlier, at the short-pulse subrelativistic S-LPA and $d_f >> L_{pre} > \lambda$, the changes of S_s due to the plasma or hot electron expansion during the acceleration process, can be neglected, thus $S_s \approx S_f$ [7].

3. EXPERIMENTAL ARRANGEMENT

The experiment was performed with the use of a 1-ps, 1.05-μm subjoule laser pulse generated by a terawatt CPA Nd:glass laser [11]. To measure forward-emitted ion fluxes the f/1 aspheric lens focusing the 1-ps laser beam on a thin target normally to its surface was used (see Fig. 1). The maximum laser intensity approached 2×10^{17}W/cm^2 at 30–40% of laser energy concentrated in the focal spot of $d_f \approx 10$ μm. A specific feature of the 1-ps pulse was its temporal shape comprising the long-lasting (>0.3ns) low-intensity background and the short-lasting prepulse (a sequence of a few ps pulses covering the time period ~10^{-10} s) of an intensity ~10^4 times lower than the intensity of the main ps pulse [12]. As the intensity of the long-lasting background was at least 10^8 times lower than that of the main pulse [11, 12], no preplasma was produced by it on the surface. The short-lasting prepulse produced the preplasma of a thickness of $L_{pre} \leq 5$ μm [12, 13]. This preplasma thickness was at least several times smaller than the laser focal spot diameter d_f, thus the condition for the quasi-planar skin-layer interaction of the laser beam with the preplasma was fairly well fulfilled (section 2). Fulfilling this condition was an essential feature of our experiment as opposed to most other short-pulse experiments, particularly those performed at relativistic laser intensities (e.g. [1, 9, 14, 15]).

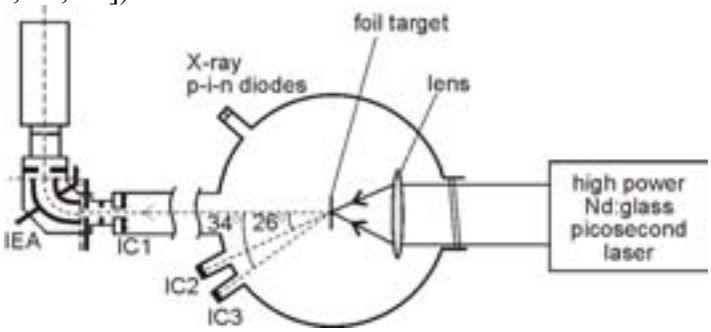

Figure 1. Simplified scheme of the experimental arrangement. IEA – electrostatic ion-energy analyzer; IC1, IC2, IC3 – ion collectors.

Both single-layer and double-layer targets were used in the experiment, in particular: (1) polystyrene targets of the thickness of L_T, of 1 μm (marked PS1); (2) an Al target of L_T = 0.75-μm (marked A10.75); (3) a double-layer target with a 0.05-μm Au front layer (facing to the laser) and a 1-μm polystyrene back layer (marked Au0.05/PS1); (4) a double-layer target with a 1-μm polystyrene front layer and a 0.05-μm Au back layer (marked PS1/Au0.05). The thickness of the target was selected in such a way that the condition: $L_T \leq \lambda$, L_h was fulfilled, where $L_h \approx 1$–2 μm is the characteristic path length of the heat wave in the target generated by the leading edge of the laser pulse (including the prepulse), calculated from the classical heat transport formulas [16, 17]. Fulfilling this condition means that the rear target surface is overheated while the ps pulse interacts with the target, the ion density scale length at the rear surface is relatively large and, as a result, the TNSA mechanism of the ion acceleration is substantially suppressed [5, 18–20].

The characteristics of fast ion fluxes emitted forward from thin foil targets were measured using the time-of-flight method. Three ion collectors and an electrostatic ion-energy analyser (IEA), located as shown in Fig. 1, were used to record ions [12]. In particular the IEA and the ring ion collector (IC1) recorded ions emitted close to the target normal and the laser beam axis. The ion measurements were supplemented with the measurements of hard X-rays in the range of 4–30 keV performed with the use of Si photodiode with proper filters.

4. RESULTS AND DISCUSSION

Figure 2 presents typical IC signals from Au0.05/PS1 and PS1/Au0.05 double-layer targets recorded in the direction normal to the target. We can see that for both targets only a single fast proton group (identified by the IEA), well separated in time from other ion groups, is generated. The fast proton beam was deduced to be highly collimated, as no fast protons were recorded at 26° and 34° angles. We also observed a single fast proton group emitted with a small angular divergence for the other targets used in the experiment, in agreement with a simple physical picture of S-LPA sketched in sec. 2.

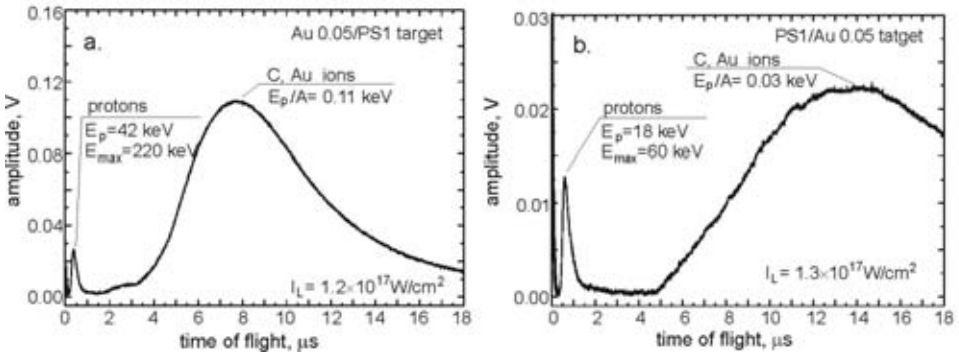

Figure 2. The ion collector signals from the double-layer targets irradiated by a 1-ps laser pulse, recorded in the direction normal to the target.

Examples of energy distributions of protons emitted in the normal direction from Au0.05/PS1 and PS1/Au0.05 targets are presented in Fig. 3, and the mean and the maximum proton energies (averaged over many laser shots) for all the targets used are shown in the diagram in Fig. 4. The highest proton energies were achieved for the double-layer target with the Au front layer. Both the mean and the maximum proton energies for this target are about 2 times higher than the ones for the PS1 target and 3–4 times higher than those for the PS1/Au0.05 target. The Au0.05/PS1 target also produced the highest hard X-ray signal. In particular, this signal was ten times higher than the one from the PS1 target and about 4 times higher than that from the PS1/Au0.05 target.

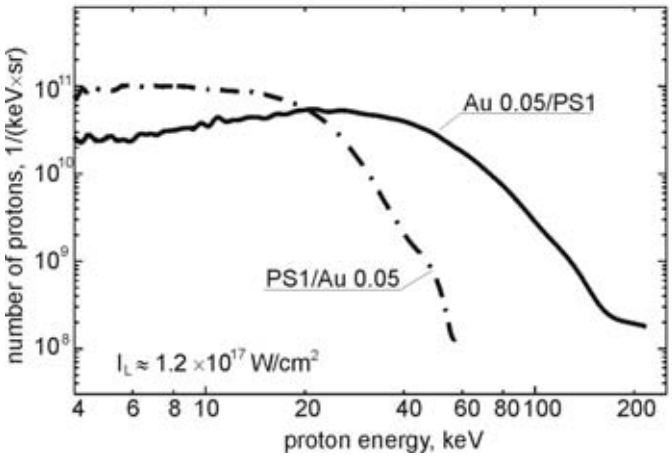

Figure 3. The energy distributions of protons emitted from the double-layer targets normally to the target.

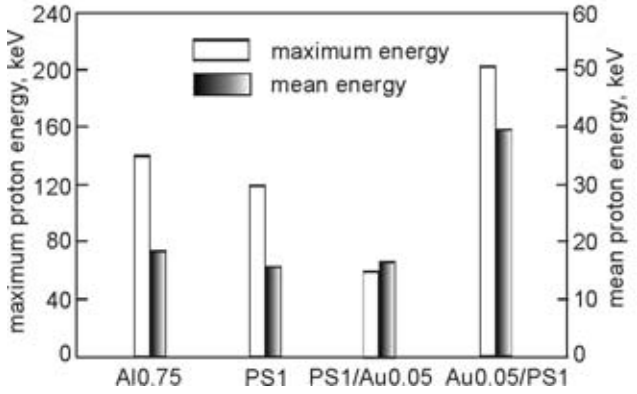

Figure 4. The maximum and the mean energies of protons produced from various thin foil targets. $I_L = (1.2 \pm 0.2) \times 10^{17} W/cm^2$.

A plausible explanation of the observed properties could be as follows. Though the whole target is more or less ionised by the laser prepulse ($L_h \geq L_T$) and then by the main laser pulse, the plasma is the hottest and its ionisation degree is the highest in the front part of the target, where the process of ponderomotive acceleration takes place. In the Au-H-C plasma mixture of the front part of the Au/PS target, the ratio of the density of fast electrons (driven directly by the ponderomotive force) to the density of protons, n_{ef}/n_p, is higher than in the case of the H-C plasma mixture of the PS target. According to the law of momentum flux conservation between the ions (mainly protons due to the highest z/A ratio) and the fast electrons, a higher n_{ef}/n_p ratio should result in greater proton acceleration (higher accelerating field) and, finally, in a higher proton velocity. In the case of the PS/Au target, the relatively cold and dense Au layer on the rear side of the target does not contribute to the fast electron balance in front of the target, but it rather acts as a damper for the protons propagating through the target. As a result, the proton energies from the PS1/Au0.05 target are significantly lower than the ones from the Au0.05/PS1 target and even lower than those from the PS1 target. On the other hand, the high-Z back layer is a reason for the higher efficiency of a hard X-ray emission in relation to the low-Z PS target.

Table 1. Parameters of ion beams produced in various experiments. (a) The current densities of protons emitted within a 3° angle cone. $I_L = (1.2 \pm 0.2) \times 10^{17} W/cm^2$. (b) The current density of protons emitted within a 20° angle cone – Ref. 10. (c) The current density of protons emitted within a 40° angle cone – Ref. 9.

method	laser	target	proton current density at the source, GA/cm^2	proton current density at the source per steradian, $GA/cm^2\,sr$	mean proton energy, keV
S-LPA	0.5J/1ps $10^{17} W/cm^2$	Al 0.75	0.3 (a)	100	18
		PS1	1 (a)	350	16
		PS1/Au0.05	0.9 (a)	320	17
		Au0.05/PS1	1.3 (a)	460	40
TNSA	50J/1ps $8\times10^{19} W/cm^2$ VULCAN	Al 100 μm	1.6 (b)	12	4×10^3
	500J/0.5ps $3\times10^{20} W/cm^2$ PETAWATT	CH 100 μm	8 (c)	16	6×10^3

To estimate the fast proton current density at the source, j_s, we used the equation (3) and assumed: $\tau_{is} = \tau_L$, $S_s = S_f$ and $Q_i = Q_{IC1}$, where Q_{IC1} is the fast ion charge passing through the IC1 collector (Fig. 1) seen within the angle of 3° from the ion source. As $Q_{IC1} < Q_i$ (the ion beam divergence is expected to be higher than 3°), the calculated proton current densities actually represent the lower limit of their real values. The current densities of protons emitted within the 3° angle cone from the particular targets, as well as the proton current densities recalculated to 1 steradian, are shown in Table 1. The highest proton current densities (>1GA/cm^2 within the 3° angle) are produced from the Au/PS target, though the difference to the case of the PS target is not so significant here as the difference between energies of protons for these targets. For comparison, the table also contains the proton current densities achieved in the experiments with short-pulse high-energy lasers (VULCAN in England and PETAWATT in USA), where the TNSA mechanism at relativistic laser intensities was expected to produce the fast proton beam [9, 10]. To calculate these current densities we used eq. (3) and the data related to the total charge of fast protons, the area of the proton source and the laser pulse duration (we assumed $\tau_{is} = \tau_L$) available from [9, 10]. It can be seen that: (a) the proton current densities at the source produced within a 3° angle by subrelativistic S-LPA are comparable to those generated within greater angles by TNSA at relativistic laser intensities; (b) the proton current densities at the source, recalculated to 1 steradian, are significantly higher for S-LPA than for TNSA (confirming, in particular, that the ion beams produced by S-LPA are highly collimated). This fairly surprising result can be understood, if we realize that in the S-LPA method a compact high-density ($n_i \approx n_{ec}/z$) plasma block is generated as opposed to the TNSA method, where a lower-density ($n_i << n_{ec}/z$), more extended plasma layer is accelerated.

One drawback of subrelativistic S-LPA is a relatively low energy of generated ions, limited to ~1MeV/nucleon. This drawback could be overcome by an extension of the advantages of subrelativistic S-LPA – whose most important symptom is a quasi-planar acceleration of the high-density plasma block, to the relativistic intensity region. It seems to be feasible if the laser pulse and the target thickness are carefully optimised [20–22], and particularly: (1) the laser prepulse (background) intensity is very low (no preplasma is produced); (2) the laser pulse is very short: $\tau_L \leq 50$fs (the laser pulse leading edge produces only a thin high-density plasma layer); (3) the laser focal spot is relatively large: $d_f \geq 10\ \lambda_L$ (to secure the quasi-planar acceleration geometry); (4) the target thickness is small: $L_T \leq \lambda_L$ (to ensure, regarding the effect of relativistic transparency, that almost the whole of the target interacts directly with the light wave). The relativistic regime of S-LPA has been demonstrated just recently with the use of 3D PIC simulations [21] (the authors called this regime the "laser piston"). The interaction of a 25-fs laser pulse of intensity 10^{23} W/cm^2 with a 1-μm solid-density plasma slab resulted in the quasi-planar generation of a relativistic ($E_i \approx 3$ GeV) high-density ($n_i \approx 3n_{ec}$) proton block with the estimated proton current density $\approx 10^{13}$A/cm^2. Although such extreme ion block parameters are still a matter of the future, the production of high-density ion blocks with multi-MeV ion energies using relativistic S-LPA is fully realistic with the current laser technology.

The very high ion current density and ps duration of the fast ion pulse produced by S-LPA opens the prospect for new experiments in high energy-density physics and nuclear fusion. In particular, a block of DT plasma accelerated by a ps laser pulse towards the DT plasma interior seems to be ideal for the generation of a laser fusion ignition front. The plasma block acts like a (space charge neutral) DT ion beam for which the ignition condition in solid density (frozen) DT fuel of >10^{10} A/cm^2 current density [23] for optimum ion energy (80 keV) can be easily achieved by ps laser pulses of $I < I_{rel}$. For example, a ps laser pulse of $I \sim 0.3\, I_{rel}$

can produce an ~80-keV DT ion flux with a current density of $j_s \sim 5.5 \times 10^{10}$ A/cm^2 at $\lambda = 1.05$ μm or $j_s \sim 5 \times 10^{11}$ A/cm^2 at $\lambda = 0.35$ μm. We see that such extremely high ion current densities are attainable even at low energies (≤1 J) and subrelativistic laser pulse intensities, which can be easily generated at a high repetition rate. In particular, it makes possible the accomplishment of highly efficient DD or DT fusion in small-scale devices for, e.g., fast neutron production. The achievement of high fusion gain through use of an optimized DT ion beam from the ps skin layer interaction in large-scale experiments can also be imagined, but it needs to be confirmed by further detailed studies.

5. CONCLUSIONS

We have shown that the S-LPA mechanism in the system with a double-layer target containing a high-Z front layer and a low-Z hydrogen-rich back layer produces a proton beam of higher proton energies and proton current densities than in the case of using a single-layer target. Independent of the kind of target, the beam is highly collimated and consists only of a single fast proton group. In spite of low energy and subrelativistic intensity of the laser pulse, the proton current densities at the source produced by the S-LPA mechanism attain extremely high values (> 1GA/cm^2), which are comparable to those achieved with the TNSA mechanism at significantly higher energies and relativistic intensities of the laser pulse. It opens the prospect for tabletop experiments in high energy-density physics and nuclear fusion. In particular, it makes possible the accomplishment of highly efficient DD or DT fusion in small-scale devices for fast neutron production and other applications.

ACKNOWLEDGEMENTS

This work was supported in part by the International Atomic Energy Agency in Vienna under Contract No 11535/RO and by the State Committee for Scientific Research (KBN), Poland, under Grant No 1 PO3B 043 26.

REFERENCES

[1] S.P. HATCHETT, C.G. BROWN, T.E. COWAN et al., Phys. Plasmas 7, 2076 (2000).
[2] P.K. PATEL, A.J. MACKINNON, M.H. KEY et al., Phys. Rev. Lett. 91, 125004 (2003).
[3] M. ROTH, T.E. COWAN, M.H. KEY et al., Phys. Rev. Lett. 86, 436 (2001).
[4] G.H. MILEY, F. OSMAN, H. HORA et al., Proc. SPIE 5449 (2004) paper 138.
[5] S.C. WILKS, A.B. LANGDON, T.E. COWAN et al., Phys. Plasmas 8, 542 (2001).
[6] J. BADZIAK, S. GŁOWACZ, S. JABŁOŃSKI et al., Appl. Phys. Lett. 85 (October 2004).
[7] J. BADZIAK, S. GŁOWACZ, S. JABŁOŃSKI et al., Plasma Phys. Control. Fusion, in print.
[8] S. GŁOWACZ, J. BADZIAK, S. JABŁOŃSKI, H. HORA, Czech. J. Phys. 54, C460 (2004).
[9] R.A. SNAVELY, M.H. KEY, S.P. HATCHETT et al., Phys. Rev. Lett. 85, 2945 (2000).
[10] M. BORGHESI, A.J. MACKINNON, D.H. CAMPBELL et al., Phys. Rev. Lett. 92, 055003 (2004).
[11] J. BADZIAK, S.A. CHIZHOV, A.A. KOZLOV et al., Opt. Commun. 134, 495 (1997).
[12] J. BADZIAK, J. MAKOWSKI, P. PARYS et al., J. Phys. D: Appl. Phys. 34, 1885 (2001).

[13] J. BADZIAK, H. HORA, E. WORYNA et al., Phys. Lett. A 315, 452 (2003).
[14] E.L. CLARK, K. KRUSHELNICK, J.R. DAVIES et al., Phys. Rev. Lett. 84, 670 (2000).
[15] M. ZEPF, E.L. CLARK, F.N. BEG et al., Phys. Rev. Lett. 90, 064801 (2003).
[16] A. CARUSO, R. GRATTON, J. Plasma Phys. 11, 839, (1969).
[17] M.D. ROSEN, Proc. SPIE 1229, 160, (1991).
[18] A.J. MACKINNON, M. BORGHESI, S.P. HATCHETT et al., Phys. Rev. Lett. 86, 1769 (2001).
[19] P. MORA, Phys. Rev. Lett. 90, 185002 (2003).
[20] M. KALUZA, J. SCHREIBER, M.I.K. SANTALA et al., Phys. Rev. Lett. 93, 045003 (2004).
[21] T. ESIRKEPOV, M. BORGHESI, S.V. BULANOV et al., Phys. Rev. Lett. 92, 175003 (2004).
[22] Y. SENTOKU, T.E. COWAN, A.KEMP et al. Phys. Plasmas 10, 2009 (2003).
[23] H. HORA, Atomkernenergie-Kerntechnik 42, 7 (1983).

TARGET INTERACTION

Kelvin-Helmholtz instability in a viscous thin film past a nanostructure porous lining

N. Rudraiah

National Research Institute for Applied Mathematics (NRIAM), Bangalore, India

Abstract: Interfacial science continues to be a frontier area of research in view of its importance in understanding control and exploitation of many physical processes in inertial fusion energy (IFE). For efficient extraction of IFE, it is essential to reduce the growth rate of surface instability in a laser accelerated ablative surface of an IFE target. The three types of surface instabilities are: i. Rayleigh-Taylor Instability (RTI), ii. Kelvin-Helmholtz Instability, iii. Richtmyer-Meskov Instability (RMI). During the first three years of our research project under CRP, we have proposed the following mechanisms to control the RTI growth rate at the ablative surface of an IFE target: smart material of nano structure porous lining at the ablative surface with and without laser radiation; the effect of an electric field and smart material of nano structure porous lining at the ablative surface with and without laser radiation effect; and the effect of a magnetic field and smart material of nano structure porous lining at the ablative surface with and without the effect of laser radiation and with a magnetic field in the direction opposing the direction of gravity.

1. INTRODUCTION

For efficient extraction of Inertial Fusion Energy (IFE) it is essential to reduce the growth rate of surface instabilities in the laser-accelerated ablative surface of an IFE target. The following three different types of surface instabilities were observed:

1. Rayleigh – Taylor Instability (RTI)
2. Kelvin – Helmholtz Instability (KHI)
3. Richtmyer – Meshkov Instability (RMI)

At present the following mechanisms are used to reduce the RTI growth rate:

1. Gradual variation of density, assuming fluid as incompressible heterogeneous fluid without surface tension.
2. Assuming fluid as compressible fluid without surface tension.
3. IFE target shell with foam layer.

Numerous numerical and experimental data for the RTI growth rate at the ablation surface for compressible fluid fit the formula

$$n = A\sqrt{\frac{\ell g}{1+\varepsilon \ell L}} - \beta \ell \upsilon_a = n_b - \beta \ell \upsilon_a \qquad (1.1)$$

By choosing suitable values for the constants A, ε and β one can fit the available data, as shown in the following table 1.

Table 1. Suitable values of the parameters in eqn. (1.1)

Authors	A	ε	β	n_m
Takabe et al (1985)	0.90	0.0	3.00	
Lindl et al (1995)	1.00	1.0	3.00	
Betti et al (1995)	0.98	1.0	1.70	
Kilkenny et al (1994)	0.90	1.0	3.00	
Knauer et al (2000)	0.90	1.0	3.02	

In the present IAEA – CRP project we have proposed the following mechanisms to reduce the growth rate of RTI:

1. Nanostructured porous lining at the ablative surface (Rudraiah, J of Fusion Sci and Tech 43, 307 – 311, 2003)

2. Electric field using electro-hydrodynamic concepts (Rudraiah, Shivakumar and Chavaraddi, Int. Symposium on Advances in Fluid Mech, Tata Mcgraw Hill Publication, 2004a)

3. Magnetic field using magneto-hydrodynamic concepts (Rudraiah, Krishnamurthy, Jalaja and Tara Desai, J. Laser and Particle Beams, 22, (2004b)

The results obtained using the above mechanisms fit a general form of dispersion relation (Rudraiah 2003):

$$n = \frac{1}{3}\ell^2\left(\delta - \frac{\ell^2}{B}\right) - \beta\ell\upsilon_a = n_b - \beta\ell\upsilon_a \qquad (1.2)$$

for a target lined with porous layer containing nanotubes, considering viscous incompressible fluid. Here $B = \delta h^2/\gamma$ is the Bond number, γ is the surface tension, and $\delta = 1$ in the absence of laser radiation, $\sigma = \theta_{p1} - \theta_{f1}$ in the presence of laser radiation.

Case1. **Incompressible fluids with nanostructured porous lining**

In this case Rudraiah (2003) has shown that

$$\delta = g(\rho_p - \rho_f),\ \beta = \frac{3\alpha\sigma}{4+\alpha\sigma},\ v_a = \frac{(4+\alpha\sigma)}{12(1+\alpha\sigma)}\ell\left(\delta - \frac{\ell^2}{B}\right) \qquad (1.3)$$

ρ_p and ρ_f are the density of porous lining and fluid, respectively δ =1 in the absence of laser radiation and $\delta = \theta_{p1} - \theta_{f1}$ in the presence of laser radiation; suffix 1 denotes the value of temperature θ at y = 1 and suffixes p and f denote porous lining and fluid. Density in the range $5 < \rho_p < 10^3$ (kg/cm^3) k = (1.1–2.7)$\times 10^{-5}$ in^2 for foam metal and k = (1.0 = 2.48) $\times$ $10^{-6} in^2$ for aloxite metal and $\varepsilon = (0.016 - 0.027)$.

Case 2. **Effect of Magnetic Fluid**

In this case Rudraiah et al (2004) have shown that

$$\beta = \frac{\mathrm{M}^3 - 3(\mathrm{M} - \tanh \mathrm{M})}{3(\mathrm{M} - \tanh \mathrm{M})}, \; \upsilon_a = \frac{(\mathrm{M} - \tanh \mathrm{M})\ell\left(\delta - \ell^2 / B\right)}{\mathrm{M}^3} \tag{1.4}$$

and $\delta = 1$ in the absence of the effect of temperature due to laser radiation, and $\delta = \theta_{p1} - \theta_{f1}$ in the presence of temperature due to laser radiation.

Case 3. Effect of electric field in a poorly conducting plasma (Rudraiah et al 2004 (a))

The dispersion relation for RTI is

$$n = n_b \pm \frac{\ell^2}{8}\Delta \tag{1.5}$$

where $\Delta = \frac{\varepsilon_0 v^2}{2h^2\delta}$; the positive and negative sign in the second term here depends on whether the electric potential is in the direction of (positive sign) or opposite to (negative sign) gravity.

In all of these cases, the maximum wave number ℓ_m and the corresponding maximum growth rate n_m and n_{bm} were obtained and the results were tabulated in Table 2.

Table 2. Values of $G = \frac{n_m}{n_{bm}}$ for the above cases

Authors	β	G
Rudraiah (2003) Case 1	0.75	0.79 $(\alpha = 0.1,\ \sigma = 4)$ (79%)
Rudraiah et al (2004) Case 2	0.00004 0.003999981 0.398176	0.99996 (for M = 0.01) 0.99602 (for M = 0.1) 0.71522 (for M = 1.0) 0.02700 (for M = 10) 0.00030 (for M = 100)
Rudraiah et al (2004) Case 3	--	0.81 (for . $\Delta = 0.1$) 81%

In the case of laser radiation taken into effect, the energy equation in the shell–film is given by

$$\upsilon_a \frac{\delta T_f}{\delta y} = \kappa_f \frac{\delta^2 \mathrm{T}_f}{\delta y^3} + \mathrm{I}_0 \Omega e^{-\Omega y} \tag{1.6}$$

In porous lining

$$0 = \kappa_f \frac{\delta^2 \mathrm{T}_p}{\delta y^2} \pm \mathrm{I}_0 \Omega e^{-\Omega y} \tag{1.7}$$

The selection of a particular sign in eqn. (2) will depend on the physical situation. In IFE there is a need for additional energy to fuse DT and hence we should choose the negative sign.

Here I_0 is the initial laser intensity of radiation and Ω is the absorption frequency. We considered two situations.

Situation 1: In this case, T_p in porous lining is assumed to be constant where $T_p > T_f$. In this case the energy equation in dimensionless form is

$$\upsilon_a \frac{\delta\theta}{\delta y} = \frac{1}{R_a} \frac{\delta^2 \theta}{\delta y^2} + Ne^{-\Omega_0 y} \tag{1.8}$$

where $N = \dfrac{\mathrm{I}_0 \Omega_0 \mu_f}{\delta_0 \mathrm{T}_0}$, $R_a = \dfrac{\partial_0 h^3}{\mathrm{K}_f \mu_f}$

To solve these we used two sets of boundary conditions:
Set 1: $\theta=1$ at y = 0 and $\theta=\theta_1$ at y = 1.

$$\text{Set 2: } \theta = 1 \text{ at } y = 0 \text{ and } \frac{d\theta}{dy} = -B_1(\theta_b - 1) \tag{1.9}$$

Here $B_i = \dfrac{h_c h}{x}$ is the Biot number and h_c is the heat transfer coefficient.

Situation 2: In situation 2, we used the Boussinesq approximation with variation T_p and T_f and obtained

$$\upsilon_a \frac{\partial\theta}{\partial y} = \frac{1}{R_a} \frac{\partial^2 \theta_f}{\partial y^2} + Ne^{-\Omega_0 y} \text{ and } 0 = \frac{\partial^2 \theta_p}{\partial y^2} - N_p e^{-\Omega_o y} \tag{1.10}$$

$$N_p = \frac{\mathrm{I}_0 \Omega_0 h^2}{\mathrm{K}_p \mathrm{T}_0} \text{ with } \frac{\partial \theta_p}{\partial y} \to 0 \text{ as } \gamma \to \infty,$$

$$\frac{\partial \theta_f}{\partial y} = B_i(\theta_{f1} - 1)), \frac{\partial \theta_f}{\partial y} = -B(\theta_{p1} - 1)) \text{at } \gamma = 1$$

and $\theta_f = 1$ at $y = 0$

These equations (1.10) were solved using the two sets of boundary conditions given by (1.9).

2. MATHEMATICAL FORMULATION

The physical configuration considered in this paper with rectangular coordinates (*x, y*) is shown in Fig. 1. It consists of a thin layer of clear fluid, denoted as region 1; it is bounded above by a nanostructure porous lining regarded as densely packed fluid saturated porous layer denoted as region 2, and below by a rigid surface at $y = 0$.The interface is at $y = h$.

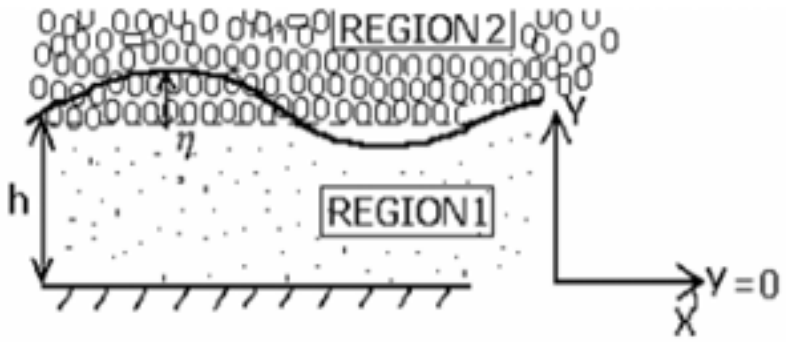

Figure 1. Physical Configuration. Region 1 is the clear-fluid and region 2 is the porous medium.

The basic equations for the clear-fluid region are governed by Navier-Stokes equations and those for the porous region by the Darcy equations as given below:

Clear fluid region - 1

$$\rho_f\left[\frac{\partial\vec{\rho}}{\partial t}+(\vec{\rho}.\nabla)\vec{\rho}\right]=-\nabla\rho+\mu_f\nabla^2\vec{q} \tag{2.1}$$

$$\nabla.\vec{q}=0 \tag{2.2}$$

where $\vec{q}=(u,v)$ are the components of velocity in the x and y direction, p is the pressure, ρ_f is the density, μ_f is the viscosity of the fluid and $\nabla^2=\frac{\partial^2}{\partial x^2}+\frac{\partial^2}{\partial \gamma^2}$.

Porous region - 2

$$\vec{Q}=-\frac{k}{\mu_f}\nabla p \tag{2.3}$$

where $\vec{Q}=(Q_x,Q_y)$ are the components of the Darcy velocity and k is the permeability of the porous media. We used the following boundary and surface conditions:

No-slip condition.

$$u=v=0 \text{ at } y=0 \tag{2.4}$$

Beavers and Joseph (BJ 1967) Slip Condition.

$$\frac{\partial u}{\partial y}=-\frac{\alpha}{\sqrt{k}}(u_B-Q_x) \text{ at } \quad y=h \tag{2.5}$$

Normal Stress Condition - Dynamic Condition .

$$p=-\partial\eta-\gamma\frac{\partial^2\eta}{\partial x^2} \quad at \quad y=h \tag{2.6}$$

Kinematic Condition

$$v=\frac{\partial\eta}{\partial t}+u\frac{\partial\eta}{\partial x} \quad at \quad y=h \tag{2.7}$$

which for linear theory takes the form

$$\upsilon=\frac{\partial\eta}{\partial t} \qquad \text{at} \quad \text{y = h} \tag{2.8}$$

These equations were simplified using the Stokes and lubrication approximations (for details see Rudraiah et al [4]). The above equations were made dimensionless using

$$u^* = \frac{u}{u_0},\ x^* = \frac{x}{h},\ y^* = \frac{y}{h},\quad p^* = \frac{p}{\delta h},\quad u_o = \frac{\delta h^2}{\mu_f}, \tag{2.9}$$

where asterisks * denote dimensionless quantities. Substituting eqs. (2.9) into the above equations and for simplicity's sake neglecting the asterisks, we got

$$\frac{d^2u}{dy^2} = \mathrm{P} \tag{2.10}$$

$$\frac{dp}{dy} = 0, \tag{2.11}$$

$$\frac{\partial u}{\partial x} + \frac{\partial v}{\partial y} = 0, \tag{2.12}$$

$$Q = -\frac{1}{\sigma^2}\mathrm{P}, \tag{2.13}$$

where $\mathrm{P} = \dfrac{\partial \rho}{\partial x}$ and $Q_x = Q$.

These equations were solved using the following dimensionless boundary and surface conditions

$$u = 0,\quad v = 0,\quad \text{at}\quad y = 0 \tag{2.14}$$

$$\frac{du}{dy} = -\alpha\sigma(u_B - Q)\quad at\quad y = 1 \tag{2.15}$$

$$p = -\eta - \frac{1}{B}\frac{\partial^2 \eta}{\partial x^2}\qquad \text{at}\qquad y = 1 \tag{2.16}$$

$$v = \frac{\partial \eta}{\partial t}\qquad \text{at}\qquad y = 1 \tag{2.17}$$

Here, $\sigma = \dfrac{h}{\sqrt{k}}$ is the porous parameter and $B = \dfrac{\delta h^2}{\sqrt{y}}$ is the Bond number.

3. SOLUTION OF THE PROBLEM

The solution of eqn. (2.10) using eqs. (2.14) and (2.15) is

$$u = \frac{Py^2}{2} - \left[P + \alpha\sigma(u_B - Q)\right]y \tag{3.1}$$

From eqn. (3.1), using $u = u_B$ at $y = 1$, and solving for u_B, we got

$$u_B = -\frac{(\sigma + 2\alpha)}{2\sigma(1 + \alpha\sigma)}P \tag{3.2}$$

Substituting for u_B and Q in eqn. (3.1), we got

$$u = \frac{Py^2}{2} - \left[1 + \alpha\sigma\left\{\frac{1}{\sigma^2} - \frac{(\sigma + 2\alpha)}{2\sigma(1 + \alpha\sigma)}\right\}\right]Py. \tag{3.3}$$

Integrating eqn. (2.12) with respect to y from 0 to 1, using eqs. (3.3), (2.14) and (2.16), we got

$$v(1)=\left[\frac{1}{12}+\frac{\sigma+2\alpha}{4\sigma(1+\alpha\sigma)}\right]\left[\frac{\partial^2\eta}{\partial x^2}+\frac{1}{B}\frac{\partial^4\eta}{\partial x^4}\right]_{y=1} \tag{3.4}$$

To find the nature of the growth rate of small periodic perturbations of the interface, we assumed

$$\eta=\eta(y)e^{i\ell x+nt} \tag{3.5}$$

where ℓ is the wave number and n is the growth rate of the interface.

Using eqn. (3.5) in eqn. (2.17), we got

$$v=n\eta \text{ at} \qquad y=1$$

$$\therefore\ n=\frac{v(1)}{\eta(1)} \tag{3.6}$$

Equation (3.6), on using eqs. (3.5) and (3.4), became

$$n=\ell^2\left(1-\frac{\ell^2}{B}\right)\Delta=n_b-\ell\beta\upsilon_a \tag{3.7}$$

where

$$\Delta=\frac{1}{12}+\frac{(\sigma+2\alpha)}{4\sigma(1+\alpha\sigma)},\ n_b=\frac{1}{3}\ell^2\left(1-\frac{\ell^2}{\beta}\right),\ \beta=\frac{3\alpha(\sigma^2-2)}{4\sigma+\alpha(\sigma^2+6)},\ \upsilon_a=\frac{4\sigma+\alpha(\sigma^2+6)}{12\sigma(1+\alpha\sigma)}\ell\left(1-\ell^2/\beta\right) \tag{3.8}$$

4. CONCLUSIONS

We noted that when $\sigma=\sqrt{2}$ the quantity n in eqn. (3.5) took the value

$$n_b=\frac{1}{3}\ell^2\left(1-\frac{\ell^2}{B}\right) \tag{4.1}$$

which is independent of porous parameters α and σ. This implies that the porous layer bounding above has no influence on the dispersion because of the reason given below.

The dispersion relation (4.1) is exactly the same as the one given by Babchin (1983) for flow in the absence of porous media. In other words, when $\sigma=\sqrt{2}$, eqn. (3.2) was reduced to

$$u_B=-\frac{1}{2}\mathrm{P}=Q \tag{4.2}$$

From this we concluded that the dispersion relation (4.1) occurs when the velocity u_B at the permeable wall of the channel is equal to the Darcy velocity Q within the permeable material, and the velocity profile in the free flow has zero shear at the interface. We noted that in most applications (see Beaver's and Joseph 1967) h will be considerably greater than $\sqrt{2k}$. It is therefore probable that for values of σ near $\sqrt{2}$ the average size of the individual pores within the porous layer is at least equal to the height of the channel and it can be assumed that the rectilinear flow in the fluid layer would break down. Therefore σ has to be greater than $\sqrt{2}$. The cutoff wave number, ℓ_{ct}, above which the KHI mode is stabilized was found to be

$$\ell_{ct}=\sqrt{B} \tag{4.3}$$

The maximum wave number, ℓ_m, obtained from eqn. (3.5) by setting $\frac{\partial n}{\partial \ell}=0$, was

$$\ell_m=\sqrt{B/2} \tag{4.4}$$

The corresponding maximum growth rates were

$$n_m = \frac{B}{4}\Delta \tag{4.5}$$

and

$$n_{bm} = \frac{B}{12} \tag{4.6}$$

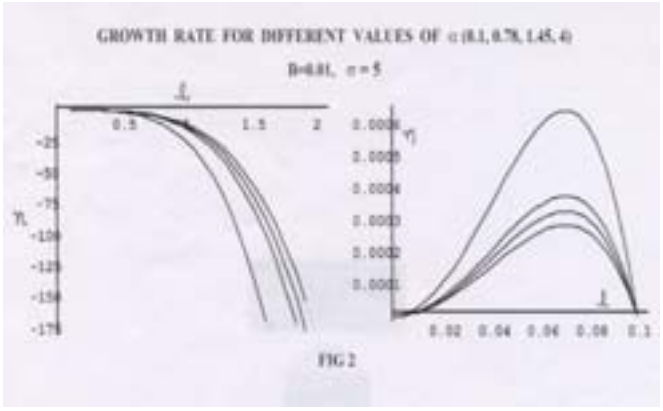

Figure 2. Growth rate plotted as a function of wave number ℓ for different values of slip parameter α, and fixed values of Bond number B and porous parameter σ.

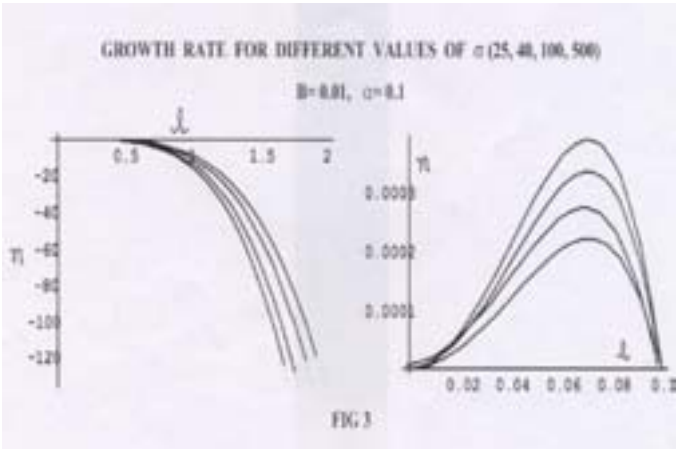

Figure 3. Growth rate plotted as a function of wave number ℓ for different values of porous parameter σ and fixed slip parameter a, Bond number B.

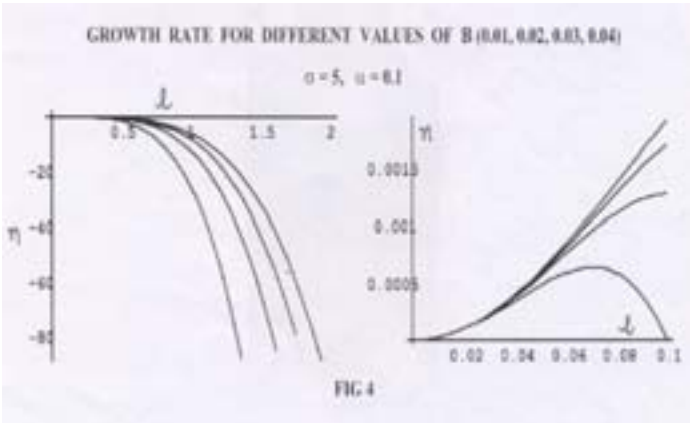

Figure 4. Growth rate plotted as a function of wave number ℓ for different values of Bond number B and fixed values of slip parameter α and porous parameter σ.

From eqs (3.7) and (3.8) it followed that the fractional decrease, Φ, in the growth rate of the free surface with a permeable upper wall over what it would be if the wall were impermeable was

$$\Phi = \frac{n - n_b}{n_b} = -\frac{3\alpha(\sigma^2 - 2)}{4\sigma(1 + \alpha\sigma)} \qquad (4.7)$$

with $\sigma > \sqrt{2}$.

From this we concluded that the growth rate of the KH instability was considerably reduced when one side of the channel had porous lining, for $n < n_b$ and $n_b > 0$.

The dispersion relation (3.7) was computed numerically for different values of slip parameter α, porous parameter σ and Bond number B, the results of which are depicted in Figs 2 to 4. These figures represent the growth rate n against the wave number ℓ. In all of these cases, the growth rate was negative for $\ell > 0.1$ and positive for $\ell < 0.1$, hence the interface always being stable at large wavelengths and unstable at small wavelengths. It is clear that an increase in α increases the growth rate in the negative direction. The same is also true in Figs. 2 and 3 for an increase in σ and B respectively.

ACKNOWLEDGEMENT

This work is supported by IAEA under the CRP project No.IND-11534. Their financial support is gratefully acknowledged.

REFERENCES

[1] A.J. BABCHIN, A.L. FRENKEL, B.G. LEVICH, G.I SIVASHINSKY (1983), Nonlinear saturation of Rayleigh-Taylor instabilities in thin films, *Phys. Fluids* , **26**, 3159–3161.

[2] S. CHANDRASEKHAR, (1968), Hydrodynamic and Hydromagnetic stability, Clarendon, Oxford, 1961.

[3] K. MIKAELIAN (1993), Effect of Viscosity on Rayleigh-Taylor and Richtmyer-Meskov Instabilities, *Phys. Rev.* E **47**, pp 375–383.

[4] N. RUDRAIAH, B.S. KRISHNAMURTHY, R.D. MATHAD (1996), The effect of an oblique magnetic field on the surface instability of a finite conducting fluid layer, *Acta Mechanica,* **119**, pp 165–180.

[5] N. RUDRAIAH, R.D. MATHAD, B. AMID (1997), "The Rayleigh-Taylor Instability of a viscous fluid layer with viscosity stratification", *Current Science*, **72**, No.6, pp 391–395.

[6] N. RUDRAIAH, C. WAGNER, G.S. EVANS, R. FREDRICH (1998), "Nonlinear study of Rayleigh-Taylor instability in thin films past a porous layer", *Ind. J. Pure. Appl. Math.* **29** No.4, pp 417–431.

[7] N. RUDRAIAH, P. SRIDHARAN, S. BHARGAVA (2002), "Rayleigh-Taylor instability in a finite thickness layer of a non-Newtonian fluid", *Appl. Mech. and Engg.* **5**, No.2, pp 315–327.

[8] N. RUDRAIAH (2003), "Effect of Porous Lining on Reducing the Growth Rate of Rayleigh-Taylor Instability in the Inertial Fusion Energy Target", *Fusion Science and Tech*. **43,** pp 307–311.

[9] N. RUDRAIAH, I.S. SHIVAKUMARA, K.B. CHAVARADDI (2004 (a)), "Electrohydrodynamic Rayleigh-Taylor Instability of a Finite Thickness Layer of Poorly Conducting Viscous Fluid", International Symposium on Advances in Fluid Mechanics, published by Tata McGrawHill.

[10] N. RUDRAIAH, B.S. KRISHNAMURTHY, A.S. JALAJA, D. TARA (2004 (b)), Effect of a Magnetic Field on the Growth Rate of Rayleigh-Taylor Instability of a Laser-Accelerated Thin Ablative Surface, Laser and Particle Beams, **22,** pp 1–5.

Interactions of subnanosecond laser -pulses with low-density plastic foams

M. Kalal[1], J. Limpouch[1,4], N.N. Demchenko[2], S.Yu. Gus'kov[2], A.I. Gromov[2], A. Kasperczuk[3], V.N. Kondrashov[6], E. Krousky[4], K. Masek[4], M. Pfeifer[4], P. Pisarczyk[7], T. Pisarczyk[3], K. Rohlena[4], V. B. Rozanov[2], M. Sinor[1], J. Ullschmied[5]

[1] Czech Technical University in Prague, FNSPE, Prague, Czech Republic
[2] P. N. Lebedev Physical Institute of RAS, Moscow, Russian Federation
[3] Institute of Plasma Physics & Laser Microfusion, Warsaw, Poland
[4] Institute of Physics, AS CR, Prague, Czech Republic
[5] Institute of Plasma Physics, AS CR, Prague, Czech Republic
[6] Troitsk Institute of Innovation and Thermonuclear Research, Troitsk, Russian Federation
[7] Warsaw University of Technology, ICS, Warsaw, Poland

Abstract. Interactions of sub-nanosecond laser pulses of iodine laser "PALS" with low-density foams and acceleration of Al foils by the pressure of the foam matter are investigated here, both experimentally and theoretically. An X-ray streak camera was used for evaluation of the speed of energy transfer through the porous foam material. The shock-wave arrival on the rear side of the target was monitored by optical streak camera. Accelerated foil velocities, measured by three-frame optical interferometry and shadowgraphy, reached a few times 10^7 cm/s. The accelerated foil shape was smooth, without any signature of small-scale structures present in the incident laser beam. Conversion efficiencies as high as 14 % of the laser energy into the kinetic energy of Al foil were derived. Experimental results compared well with our two-dimensional hydrodynamics simulations and with an approximate analytical model.

1. INTRODUCTION

Laser interactions with low-density plastic foams of supercritical density, i.e., the electron density n_e, in the fully ionized and homogenized foam greater than the laser critical density, are important, as foam layers can be used for the improvement of the spherical symmetry of direct-drive inertial fusion. Most approaches to implosion symmetry improvement are based on smoothing the laser imprint by thermal conductivity in a relatively thick, relatively hot low-density outer layer of the target (Desselsberger *et al*., 1992; Gus'kov *et al*., 1995). An alternative approach to the mitigation of laser imprint was based on density tailoring of a layered target, consisting of low-density porous matter on top of a higher-density payload. A distant laser prepulse was used as a shaping pulse providing impedance matching between foam and payload and thus suppressing Rayleigh-Taylor instability (Metzler *et al*., 1999). While many experiments (Hall *et al*., 2002) use foams with micron or submicron pore size, interactions of laser pulses of several nanoseconds with foams of typical pore radius comparable to or greater than 10 μm were studied in other experiments (Gus'kov *et al*., 2000; Caruso *et al*., 2000). This study linked up to our previous work (Kalal *et al.*, 2003), and the distinctive feature of these experiments was the interaction of subnanosecond laser pulses with foams containing large pores, the laser pulse being shorter than the time needed for the full homogenization of the foam matter.

The main goal of our work was to study energy transport through the low-density porous matter and to demonstrate a sufficient efficiency of thin foil acceleration together with a substantial smoothing effect of the low-density foam absorber. The experimental setup is explained in section 2, while the results of X-ray and optical diagnostics are presented and discussed in section 3. Our two-dimensional hydrodynamic simulations are described in

section 4, while analytical estimates are calculated and compared with the experiment and simulations in section 5. Conclusions are drawn and discussed in the last section.

2. EXPERIMENTAL SETUP

Experiments were conducted on the PALS iodine laser facility (Jungwirth *et al.*, 2001) in Prague. The laser provided a 400 ps (FWHM) pulse with an energy up to 600 J at the basic harmonic ($\lambda_1 = 1.32$ μm). Laser was incident normally on the target; the laser spot radius in the best focus was $R_L \approx 40$ μm. Here the target was placed outside the best focus and the laser spot radius $R_L \approx 150$ μm was used. Thus laser spot radius R_L is large compared to pore diameter D_p. Laser irradiances were varied from $I \approx 10^{14}$ W/cm^2 up to $I \approx 10^{15}$ W/cm^2. No method of optical smoothing was used, and thus one can assume that the laser beam focus was not quite uniform and contained small-scale intensity non-uniformities.

Several types of foam target were used. Most experiments were done with thick layers of polystyrene foam of a density range of 8–10 mg/cm^3 and of a typical pore diameter of $D_p \approx 50$–70 μm. Other polystyrene foams of a density of $\rho \approx 30$ mg/cm^3 and a pore diameter of $D_p \approx 10$ μm, and also of $\rho \approx 20$ mg/cm^3, and $D_p \approx 5$ μm, as well as polyvinylalcohol (PVA) foam of a density $\rho \approx 5$ mg/cm^3 and a typical pore diameter of $D_p \approx 5$ μm were used. In the majority of foam targets a 2 μm or 0.8 μm thick aluminum foil was placed at the rear side of the foam.

The diagnostic system included observation of target emissions and also optical probing of the target. A side-view pinhole image of plasma emissions in the X-ray region (photon energy >1.7 keV) was observed by the KENTECH low-magnification X-ray streak camera placed in a side view. The temporal resolution was either 30 or 70 ps and the spatial resolution of 50 μm was in the direction normal to the target surface (target depth). We present here also preliminary results on the measurement of shock wave arrival on the rear side of the target via self-emission registered by the optical streak camera. Optical interferometry and shadowgraphy were carried out by means of a 3-frame interferometric system with automated image processing technique, described in detail in a paper (Pisarczyk *et al.*, 1994). Each of the three recording channels was equipped with a CCD camera of the Pulnix TM-1300 type, with a matrix of 1300 × 1030 pixels. The diagnostic system used a probing beam at the third harmonics with similar, but slightly shorter pulse duration than that of the main beam. Interferogram processing included parasitic noise filtering, comparison of object and reference interferograms, and a subsequent reconstruction of radial electron density distributions.

3. EXPERIMENTAL RESULTS

The target self-emission was imaged with eleven-fold magnification on the X-ray streak camera 50 μm wide entrance slit providing spatial resolution along the target depth. Only photons of energy above 1.5 keV could propagate without significant absorption through the recording channel. As plastic foams containing only carbon and hydrogen were used, the amount of X-ray emissions was rather low. The only usable pictures (weak, but significantly above the X-ray streak sensitivity limit) were recorded of the foam targets of largest pore diameter (50–70 μm). From such recordings, as presented in Fig. 1, the upper estimate of laser penetration depth was the thickness of the immediately heated layer of about 120 μm.

Thus the laser penetration was not more than two pore layers. Later a heat wave propagated into the foam material with a velocity of approximately ~ 1.4×10^7 cm/s; the rear side of the heated area is denoted by a full yellow line in Fig. 1. Though the X-ray signal lasts for nearly 3 ns, the X-ray emitting zone covers only about two thirds of the foam thickness, and no emission near the Al foil at the target rear side was detected. Consequently, the foil at the rear side of the target is supposed to be accelerated as a whole without significant expansion and its velocity can be measured by optical probing.

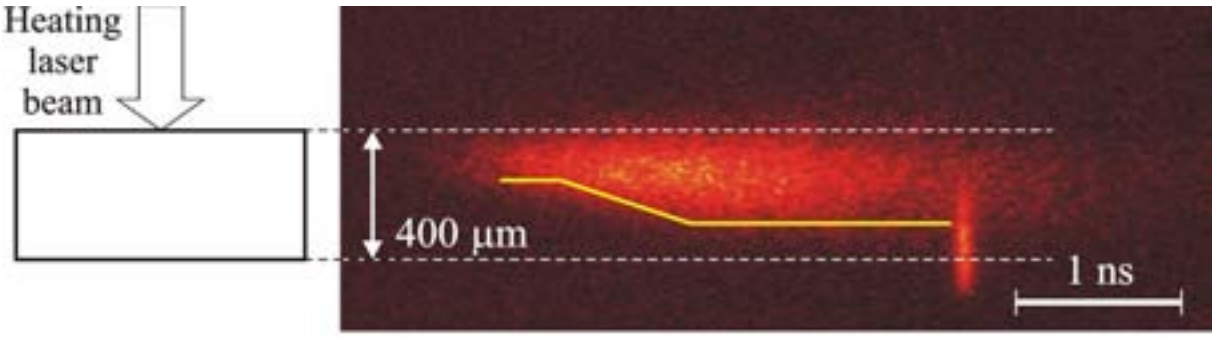

Figure 1. X-ray streak record of lateral slit picture of interaction of 400 ps iodine laser (λ=1.32 μm) pulse of energy 92 J and beam radius 150 μm with 400 μm thick polystyrene foam of density $\rho \approx 9$ mg/cm^3 and pore diameter $D_p \approx 50 - 70$ μm, with a 2 μm thick Al foil placed at the rear side of the target.

Experimental sequences of 3 interferometric pictures taken in one laser shot are presented in Figure 2. While the rear side boundary of a 400 μm-thick polystyrene target with a 2 μm Al foil on the rear side was sharp with no signs of low-density plasma behind the target, a 0.8 μm-thick Al foil at the rear side of a 100 μm-thick PVA foam was heated and its expansion observed later.

The position of point P (rear side opposite to the laser beam centre) was measured with a precision of 5–10 μm, the results of which are summarized in Figure 3. The speed of the accelerated Al foil could be determined from the difference in point P positions in different frames. The speed of the accelerated foil grew with the laser energy. Foil acceleration during the laser pulse was inferred in 100 μm-thick PVA foam. In 400 μm-thick polystyrene foams, the shock wave reached the foil only 2–4 ns after the laser pulse, and the delay decreased with laser energy. The above delay was by about 2 ns larger than in simulations of homogeneous material of the same density as the foam, and the difference was tentatively explained by the foam homogenization process.

In order to verify the feasibility of the measurement of the time and form of the shock wave arrival on the rear side of the target, we conducted a preliminary experiment where self-emission from the rear side of the target was imaged on the slit of an optical streak camera. The result is presented in Fig. 4 where the absolute timing of the shock wave arrival was established from the fiducial position. The shock wave arrival delay grows smoothly with the distance from the central point. No macroscopic spatial features were registered, which was also consistent with the smooth shape of the accelerated part of the foil observed in optical interferometry. This preliminary measurement was carried out during another experiment on a PALS laser, and third harmonics of the iodine laser were used. Consequently, due to different experimental conditions the direct comparison of this measurement with other results presented here is not possible.

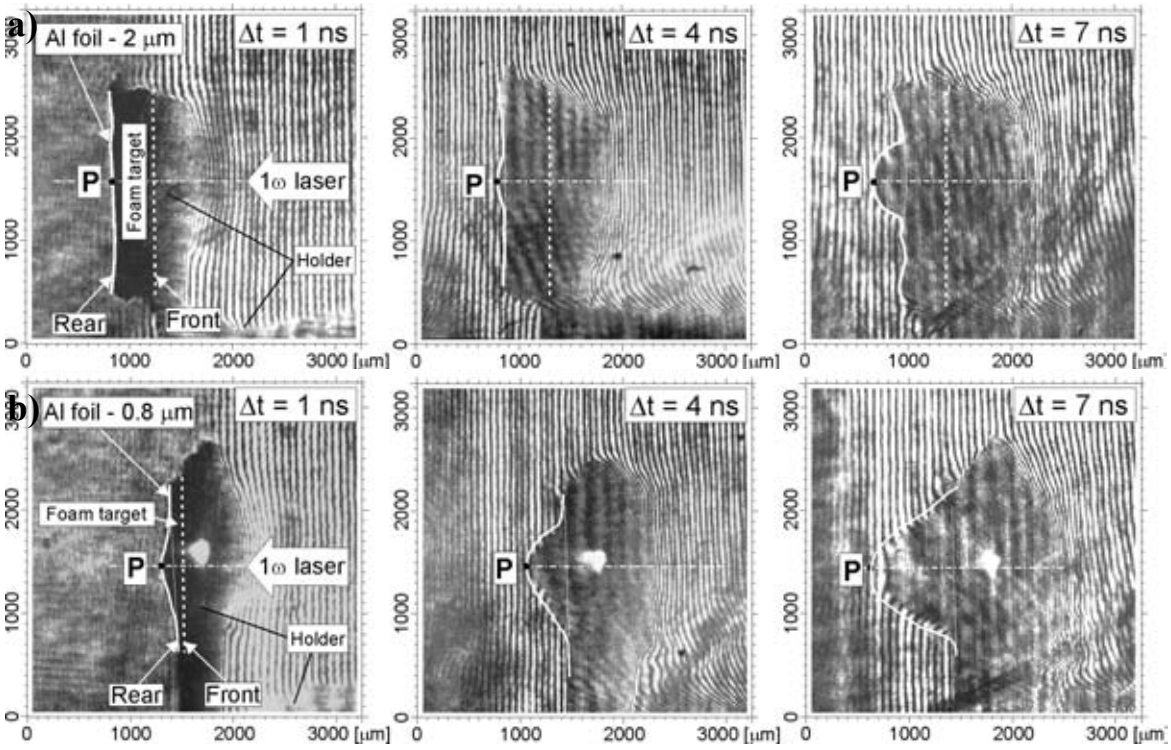

Figure 2. Sequence of 3 interferograms recorded in one shot in time instants 1, 4 and 7 ns after the main 400 ps FWHM laser pulse maximum. The laser wavelength was 1.32 μm and the beam radius 150 mm on the targets. Parasitic effects of the target holder are denoted in the left pictures. a) Polystyrene foam of ρ ~ 9 mg/cm^3, D_p ~ 50–70 μm, 400 μm thick, with 2 μm-thick Al foil at its rear side. Laser energy 173 J. b) PVA foam of ρ ~ 5 mg/cm^3, D_p ~ 5 μm, 100 μm thick, with 0.8 μm-thick Al foil at its rear side. Laser energy 238 J.

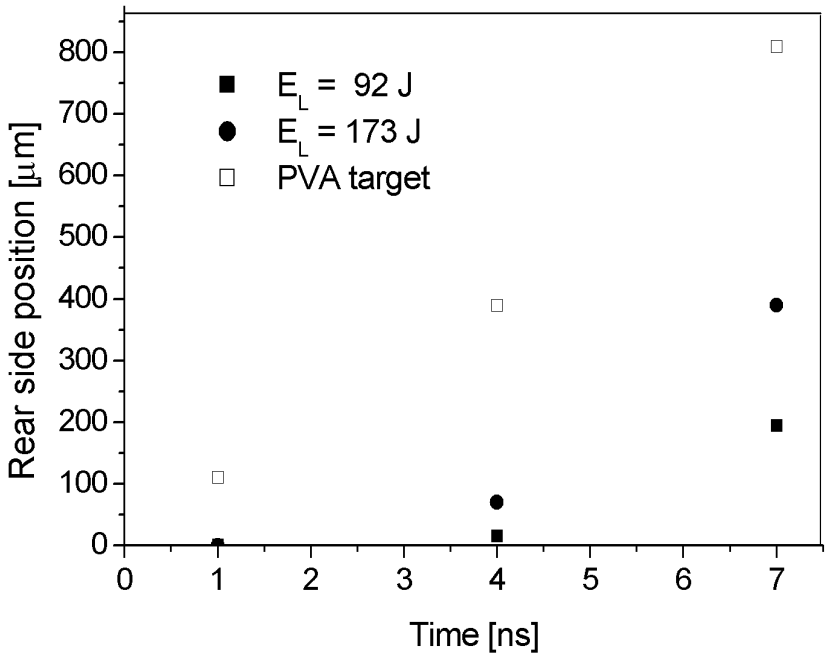

Figure 3. Experimentally measured position of point P versus time after the laser pulse maximum for two laser energies and 2 μm Al foil on polystyrene foam of ρ ≈ 8–10 mg/cm^3, pore diameter D_p ≈ 50–70 μm and thickness Δ = 400 μm. Points are also plotted for 0.8 μm Al foil on PVA foam of 5 mg/cm^3, D_p ≈ 5 μm, Δ = 100 μm and laser energy 238 J.

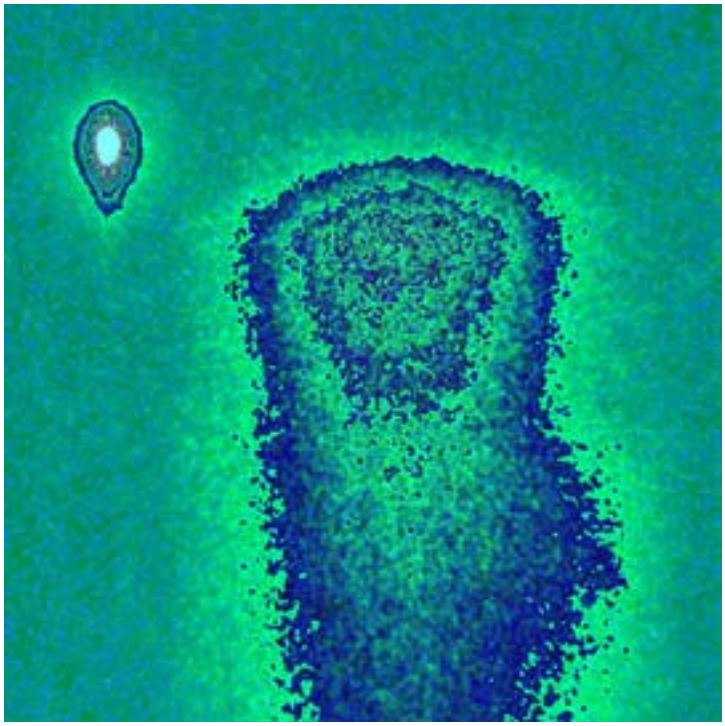

Figure 4. Optical streak record of self-emission of the rear side of the target with fiducial in upper left corner. Time grows downwards with a scale of 5 ns/image; the spatial scale is 1.3 mm/image. Third harmonics of an iodine laser pulse (wavelength λ=432 nm, energy E_L = 75 J) are focused on a spot of a radius of 150 μm on 700 μm thick polystyrene foam of a density of $\rho \approx 9$ mg/cm^3 and pore diameter $D_p \approx 50 - 70$ μm, a 5 μm-thick Al foil is placed at the target rear side.

4. COMPUTATIONAL SIMULATIONS AND ANALYTICAL MODEL

Simulations were performed in cylindrical geometry by two-dimensional Lagrangian hydrodynamics, code ATLANT-HE, including advanced treatment of laser propagation and absorption (Iskakov *et al.*, 2003). The code does not take into account the fine-scale structure of the foam, thus the time of the hydrothermal wave transit through the foam may be underestimated.

The calculated laser absorption was approximately 50%. The plasma radius essentially exceeds the laser beam radius on the target due to fast lateral heat transport in the low-density porous matter. The smooth shape of the accelerated foil was observed, with the width considerably larger than the laser beam diameter. The fast electrons did not significantly preheat the unevaporated Al layer in simulations for the laser intensities $\leq 10^{15}$ W/cm^2.

The analytical model was based on the assumption of a spherical hydrothermal wave (Gus'kov *et al*., 2000) propagating from the laser absorption point. The time instants when the hydrothermal wave reached the rear side of the target were in good agreement with the numerical simulations. However, the experimental data were by about 2 ns greater for 400 μm thick polystyrene foam. In our opinion, such a condition was caused by the direct influence of

the initial foam structure on the target dynamics. The pressure accelerating the Al foil was calculated, the derived hydrodynamic efficiency being $\eta \approx 0.12$.

Table 1. Foil velocities measured in the experiment, calculated in our simulations and via analytical model.

Laser energy	**Target**	$\mathbf{v_{exp}}$ **(cm/s)**	$\mathbf{v_{simul}}$ **(cm/s)**	$\mathbf{V_{max}}$ **(cm/s)**
92 J	$(CH)_n$	6.0×10^6	4.9×10^6	4.8×10^6
173 J	$(CH)_n$	8.0×10^6	8.2×10^6	6.7×10^6
238 J	$(CH)_n$	------	1.1×10^7	8.2×10^6
238 J	PVA	1.4×10^7	3.5×10^7	1.32×10^7

Table 1. $(CH)_n$ is 400 μm thick polystyrene foam of a density of 9 mg/cm^3 with a 2 μm Al foil, and the PVA is 100 μm thick PVA foam of a density of 5 mg/cm^3 with a 0.8 μm Al foil. Experimental and simulation velocities are represented by average values in the interval 4–7 ns after the laser maximum.

The foil velocities measured in the experiment, calculated in our simulations and via analytical model, are compared in Table 1. The Al foil in PVA foam target is heated up to 800 eV in the simulations and its expansion led to an excessive velocity of the rear boundary.

5. CONCLUSIONS

Interactions of a laser beam of the iodine laser "PALS" with low-density foam targets have been investigated, both experimentally and theoretically. The speed of the heat wave inside polystyrene foam was estimated $\sim 1.4 \times 10^7$ cm/s from the X-ray streak measurements.

Velocities of accelerated foil at the rear side of the target, measured by 3-frame optical interferometry, were in good agreement with our two-dimensional hydrodynamic calculations and with the analytical model. However, in our experiments a delay in the shock wave propagation in the foam was observed in comparison with our theoretical calculations which did not take into account the foam structure. This is explained here by the phenomenon of non-equilibrium foam homogenization. The smooth arrival of the shock wave on the rear side of the target was in agreement with the smooth shape of the accelerated foil observed by way of interferometry.

ACKNOWLEDGEMENTS

This work was partly funded by project INTAS-01-572 and by IAEA Research Project No. 11655/RBF. Partial support of the Czech participants by the Czech Ministry of Education, Youth and Sports under project LNA00100 "Laser Plasma Research Centre" is gratefully acknowledged. The authors thank Dr. Dimitri Batani for his expertise and the PALS staff for its excellent support.

REFERENCES

[1] A. CARUSO, C. STRANGIO, S.YU. GUS'KOV, V.B. ROZANOV (2000). Interaction experiments of laser light with low density supercritical foams at the AEEF ABC facility. *Laser & Particle Beams* **18**, 25–34.

[2] M. DESSELBERGER, M.W. JONES, J. EDWARDS, M. DUNNE, O. WILLI (1992). Nonuniformity imprint on the ablation surface of laser-irradiated targets. *Phys. Rev. Lett.* **68**, 1539–1542.

[3] S.YU. GUS'KOV, N.V. ZMITRENKO, V.B. ROZANOV (1995). Laser-greenhouse thermonuclear target with distributed absorption of laser energy. *JETP* **81**, 296–304.

[4] S.YU. GUS'KOV, A.I. GROMOV, YU.A. MERKUL'EV, V.B. ROZANOV, V.V. NIKISHIN, V.F. TISHKIN, N.V. ZMITRENKO, V.V. GAVRILOV, A.A. GOL'TSOV, V.N. KONDRASHOV, N.V. KOVALSKY, M.I. PERGAMENT, S.G. GARANIN, G.A. KIRILLOV, S.A. SUKHAREV, A. CARUSO, C. STRANGIO (2000). Nonequilibrium laser-produced plasma of volume-structured media and ICF applications. *Laser & Particle Beams* **18**, 1–10.

[5] T. HALL, D. BATANI, W. NAZAROW, M. KOENIG, A. BENUZZI (2002) Recent advances in laser–plasma experiments using foams. *Laser & Particle Beams* **20**, 303–316.

[6] A.B. ISKAKOV, N.N. DEMCHENKO, I.G. LEBO, V.B. ROZANOV, V.F. TISHKIN (2003). 2D Lagrangian code "ATLANT-HE" for simulation of laser-plasma interaction with allowance for hot electron generation and transport. *Proc. SPIE* **5228**, 143–150.

[7] K. JUNGWIRTH, A. CEJNAROVA, L. JUHA. B. KRALIKOVA, J. KRASA, E. KROUSKY, P. KRUPICKOVA, L. LASKA, K. MASEK, T. MOCEK, M. PFEIFER, A. PRAG, O. RENNER, K. ROHLENA, B. RUS, J. SKALA, P. STRAKA, J. ULLSCHMIED (2001). The Prague Asterix Laser System. *Phys. Plasmas* **8,** 2495–2501.

[8] M. KALAL, J. LIMPOUCH, E. KROUSKY, K. MASEK, K. ROHLENA, P. STRAKA, J. ULLSCHMIED, A. KASPERCZUK, T. PISARCZYK, S.YU. GUS'KOV, A.I. GROMOV, V.B. ROZANOV, V.N. KONDRASHOV (2003). Thermal smoothing by laser-produced plasma of porous matter. *Fusion Science & Technology* **43**, 275–281.

[9] N. METZLER, A.L. VELIKOVICH, J.H. GARDNER (1999). Reduction of early-time perturbation growth in ablatively driven laser targets using tailored density profiles. *Phys. Plasmas* **6**, 3283–3295.

[10] T. PISARCZYK, R. ARENDZIKOWSKI, P. PARYS, Z. PATRON (1994). Polari-interferometer with automatic images processing for laser plasma diagnostics. *Laser & Particle Beams* **12**, 549–562.

TARGET FABRICATION

FST technologies for IFE target fabrication, characterization and delivery

E.R. Koresheva, I.V. Aleksandrova, G.D. Baranov[1], V.I. Chtcherbakov, A.I. Kupriashin, V.N. Leonov, A.I. Nikitenko, I.E. Osipov, V.V. Petrovskiy[1], I.A. Rezgol, A.I. Safronov[1], T.P. Timasheva, I.D. Timofeev[1], S.M. Tolokonnikov, A.A. Tonshin[2], L.S. Yaguzinskiy[2]

Lebedev Physical Institute of RAS, Moscow, Russian Federation
[1] "Red Star" State Unitary Federal Enterprise, Moscow, Russian Federation
[2] Moscow State University, Moscow, Russian Federation

Abstract. Inertial fusion energy (IFE) research indicates that energy generation by means of cryogenic fuel target compression requires targets to be injected into the target chamber centre at a rate of about 6 Hz. This requirement can be fulfilled only if the targets are free standing. Technologies based on using the free-standing targets (or FST-technologies) in each production step are being developed at the Lebedev Physical Institute (LPI) since 1989. In this paper we present the progress results of the study being done for an issue of the FST-technologies extension on IFE requirements.

1. IFE TARGET PRODUCTION

The demonstration of the supply of free-standing targets (i.e., target technology and delivery) is the important task of the IFE programme. With this aim, a prototypical target system has been created at LPI [1]. The system operates with 5-to-25 free-standing targets at one time. The transport process is target injection between fundamental system elements: shell container – layering module – test chamber. The targets move downwards along the layering channel in rapid succession - one after another - which results in a repeatable target injection into the test chamber (Fig.1). Depending on the layering channel geometry, the target residence time inside may vary within the range of 1÷15 sec.

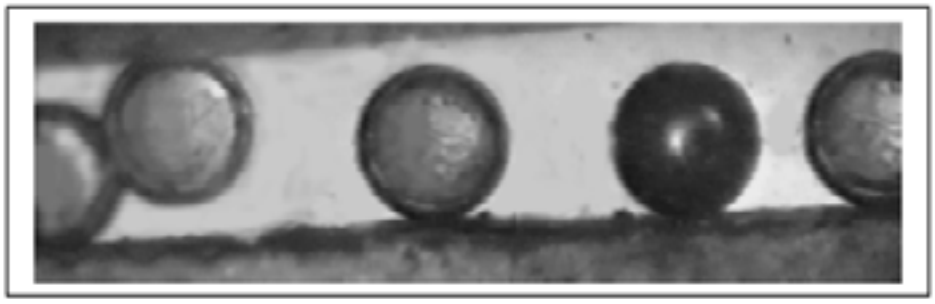

Figure 1. Cryogenic target injection from the layering module into the test chamber at a rate of 0.1 Hz. CH shells of 1 mm-diam. with 90 μm-thick H2 solid layer.

Using the created system we were able to demonstrate, on a reduced scale, the main steps of the IFE target supply: D2-fuel filling, cryogenic layering and injecting the millimeter size targets into the test chamber with a rep-rate of 0.1 Hz [2].

The FST layering simulation code was first developed for millimeter-size targets [3]. It is based on solving Stephen's problem of moving boundaries between the fuel phases (gas, liquid and solid) and nonlinear boundary conditions on the outer shell surface. Then the code was made adaptable and scalable for numerical experiments with reactor targets. As a result of these activities, it has been well documented (theoretically and experimentally) that the

FST layering method forms thick solid cryogenic layers (up to 100 μm) inside moving polymer shells (1.8 mm-diam.) within a time of less than 15 s.

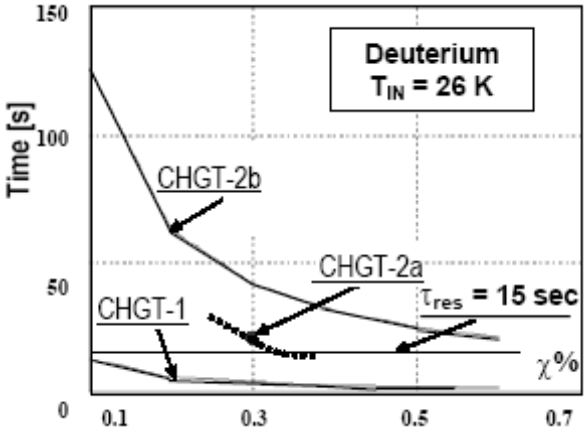

Figure 2. Layering time vs. parameter χ.

Theoretically we considered two configurations of a classical high-gain target: CHGT-1 (4 mm diam. and a 45 μm-thick CH shell with a 200 μm-thick fuel layer) and CHGT-2 (5.5–6 mm diam. and a 300–500 μm-thick CH shell with a 200–300 μm-thick fuel layer). Numerical experiments carried out in [2, 4] have shown that for the CHGT1 the gas fill time by diffusion is about 14 hours for D2, the calculated layering time is between 5 and 15 sec (Fig. 2; χ is the relative contact area between the target and the channel wall). This allows for carrying out first experiments on reactor target formation by FST using the existing layering module.

The CHGT2 is noted for its thick polystyrene shell with low thermal conductivity, which results in a relatively long layering time: between 66 and 127 s, depending on the shell thickness (Fig. 2). This means that the existing layering module should be modified. With this in mind we created and tested a miniature device, a so-called rotating and bouncing cell (R&B cell), which is mounted at the bottom of the layering module, directly in the optical test chamber (Fig. 3; [4]). A vibrating membrane is an integral part of the cell. The couple "membrane & target" is driven by an input signal generated by an inverse piezo-electric effect. The R&B cell operates at cryogenic temperatures, which are controlled within the rates of 0.1–60 K/min. If we keep fixed temperatures, it is controlled in ±0.01 K. The modulation of the input signal impresses information on the carrier frequency and amplitude. This allows placing the target in a trajectory with modes similar to those of the FST-layering channel. The advantages of the R&B cell application for fuel layering are that the time of target residence is unlimited and the device dimensions are rather small (Table 1). At the moment our experiments have shown that the R&B cell application allows fabricating uniform small-grained D_2 layers on the inner surface of a CH shell (Figure 4).

Figure 3. In the R&B cell layer symmetrization & freezing take place within the same small area.

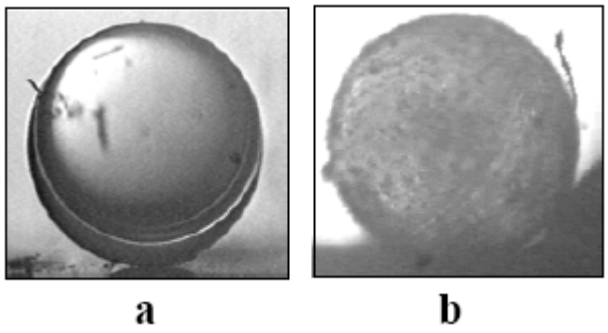

Figure 4. Cryogenic D2-layering using the R&B cell (a) before layering, 20 K;(b) after layering, 5.8 K; 1.2 mm-diam. CH shell filled with D2 up to 300 atm at 300 K. Piezocrystal: 10 kHz, 75 V; Layer thickness: ~47 μm; Formation time: <60 sec.

For reactor-scale targets, there is one more important issue - target quality survival. The critical point is to withstand the environmental effects: excess heat and mechanical load arising during target delivery. Our investigations have shown that the properties of fuel material and its microstructure and composition have a dominant effect on the cryogenic layer quality and substantially determine the fuel layer response to the environment. For example, the introduction of minor dopes (HD) into hydrogen (H2) allows the forming of a cryogenic layer with a glassy structure, which has an extremely smooth surface finish [4, 5]. These experiments were carried out with more than 30 targets. It is of particular importance that the glassy layer obtained is highly stable and remains transparent upon target heating, at least

within one heating cycle from 5 K to triple point and higher. This layer property has large prospects for future IFE application because it enables the target to be injected into the reactor chamber at very low temperatures, when risk of both mechanical and thermal damage is minimal. Currently, we can form glassy layers with different doping agents and study their influence on the layer quality (Figure 5) [6].

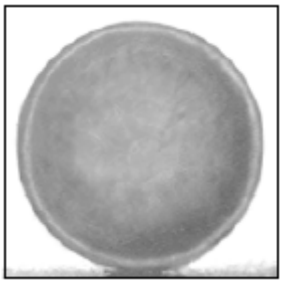

Figure 5. Solid cryogenic layer in a glassy state CH shell: 2R=1.5 mm; Coating: 200Å Pt/Pd 50-μm solid cryo layer from 97% D2+3% Ne.

Further developments are being designed to continue this study and initiate parallel experiments on super-dispersed structure formation using the R&B cell.

Table 1. Comparative characteristics of the FST-layering devices

Symmetrization & Freezing	Dimension, mm^3	Residence time limitation
Layering channel	1500x25	< 1-to-15 s
R&B cell	5x25	Unlimited

2. IFE TARGET CHARACTERIZATION

The goal of the ICF target characterization is to provide reliable information within a definite time. From this viewpoint, the following two stages of producing the targets are of special interest: (1) the layering technique development, which requires the most comprehensive information on the object (i.e., a 3D reconstruction of the target is necessary); (2) the fueling of a commercial power plant, which requires 500, 000 fusion targets each day or six fusion targets each second.

In the first case it is necessary to enhance information about the target configuration, in the second to shorten the characterization time (fast quality control).

For precise and accurate characterization of individual targets (microshell or cryogenic targets), a prototype of the tomograph was created at LPI (Fig.6), including the system of a target scanning and image recording, the tomographic test chamber and the specially developed software *"Target Studio"* for target 3D reconstruction, using a set of its backlit images obtained in visual light [7]. The spatial resolution of the optical system was 1 μm for 490 nm wavelengths; the accuracy of angular positioning of the target was ±1.5-to-2.5 minutes. The prototype operation was demonstrated in a number of controlled experiments with polystyrene microshells for a projection set ranging from 60 to 100 backlit images. The prototype has the following distinguished features: (a) operation with both free-standing and

pre-mounted targets; (b) scanning of a target both at room and cryogenic (4.2-to-77 K) temperatures.

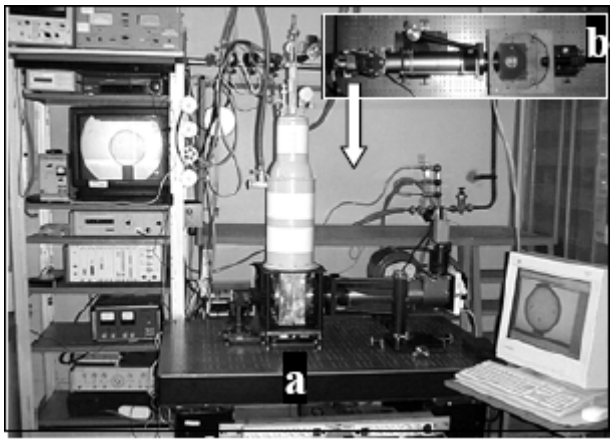

Figure 6. A 100-projections tomograph for free-standing target characterization: views from the side (a) and the top (b).

Methods for fast target characterization were also under way at LPI, namely: time minimization of all processing stages, threshold characterization, fast characterization of a target batch, and moving target characterization with simultaneous control of its quality, velocity and trajectory. One of the approaches to solve the enumerated issues was the application of the optical scheme based on the Fourier holography (correlator with frequency plane). The actuating unit and the photo-detector only determined the operation rate of such a system (several μsec).

The physical principles of the Fourier holography scheme operation were considered and a simulation model was developed in the form of a complete computer programme, *HOLOGRAM*. The shadow target images considered as amplitude transparencies were entered as model input.

Our computer experiments have shown that this approach allows to achieve the following results [8]: (1) recognition of the target shape perturbations in both low and high harmonics, (2) quality control of both a single target and a target batch, (3) simultaneous control of the flying target quality, velocity and trajectory.

Thus, the Fourier holography scheme looks promising for the fast control of IFE targets.

3. IFE TARGET DELIVERY

The following target delivery issues are under way at LPI: target tracking and timing, target trajectory correction, technology of target protection from overloads and overheat, protecting sabot composition and geometry optimization, sabot and target assembly, etc. Within this scope, the design of the device for continuous cryogenic target fabrication, target & sabot repeatable assembly and acceleration using the coil gun has been proposed [9]. Small changes of the design allow for the repeatable assembling the elements of an indirect-drive target at cryogenic temperatures.

Theoretical and experimental studies were carried out confirming for the first time the feasibility of ferromagnetic sabot acceleration in a single coil at cryogenic temperatures

(Figure 7). Further analysis has shown that the application of magneto-dielectric instead of ferromagnetic processes makes it possible to reduce the sabot weight by 3 to 4 times, under retention of its magneto-active properties, allowing to effectively accelerate the sabot both in a coil and gas gun, as well as in the coil&gas hybrid injector [9]. A physical model of acceleration of the magneto-dielectric sabot in the electromagnetic field of solenoids was created and a relevant mathematical software, *COIL,* was developed, allowing the optimization of sabot composition and geometry.

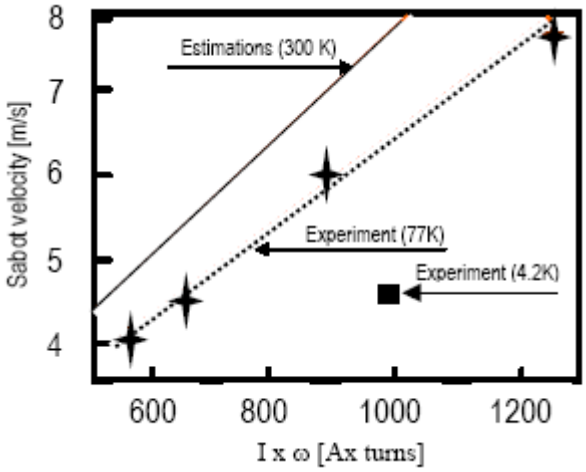

Figure 7. Ferromagnetic sabot acceleration in a single coil.

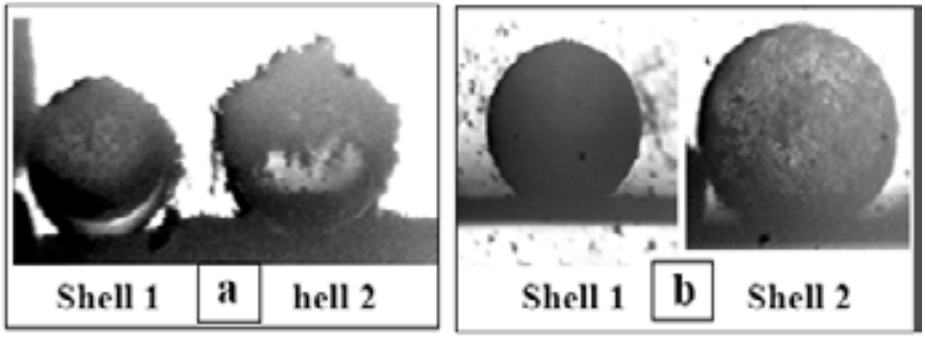

Figure 8. Deposition of the outer protective cryogenic layer onto the target, using the R&B cell (T=14.6 K).
CH shells inside the R&B cell prior to the experiment. Shell 1(2R=1.2 mm) has a palladium coating of 150 Å thickness; Shell 2:2R=1.4 mm; (b) An opaque protective cryogenic layer covers each shell after the R&B cell operation in the mode of target bouncing.

The deposition of the outer ablating layer was also under consideration. The ablating layer can be used for (a) protecting a target during its flight inside a reactor chamber and (b) controlling the target flight trajectory. Using the R&B cell, we first demonstrated a process of deposition of the dispersed layer of solid oxygen onto the outer surface of the polystyrene shells (Fig. 8; [6, 7]). Allowing for the results obtained (opaque protective layer), we propose the following physical layout of the target formation: fuel filling, fuel layer formation, target characterization, and deposition of the outer ablating layer if the target is within specifications.

4. NEXT STEP

Our investigations allowed us to point out the most promising options for further R&D in the area of IFE target technology, namely: (a) application of the R&B cell for fuel layering as well as for outer ablating layer creation, (b) formation of a fuel layer in a "glassy" state, using minor doping, (c) precise target characterization, using a 100-projections tomograph, (d) fast target characterization, using the Fourier holography approach, (e) cryogenic assembly of the elements of an indirect-drive target and/or target assembly with protecting sabot (single-step and repeatable modes).

We plan to create a small-scale experimental facility in order to put this activity into practice.

REFERENCES

[1] I.V. ALEKSANDROVA et al. *Free-standing target technologies for ICF*. Fusion Tech., 38, N1,166, 2000.

[2] E.R. KORESHEVA et al. *IAEA Project #11536: Extension of Free-Standing Target Technologies on IFE Requirements.* report, 1st IAEA Research Coordination Meeting on Elements of IFE Power Plants (May 21–24, 2001, IAEA Headquarters, Vienna, Austria).

[3] I.V. ALEKSANDROVA et al. *Rapid fuel layering inside moving free-standing ICF targets: physical model and simulation code development*. Laser and Particle Beams, 20,13, 2002.

[4] E.R. KORESHEVA et al. *Progress in the extension of free-standing target technologies on IFE requirements.* Fusion Science and Technology, 43, N3, 290, 2003.

[5] E.R. KORESHEVA et al. *A new method of fabrication of the transparent solid hydrogen layer inside a microshell: the application to inertial confinement fusion*. J.Phys.D: Appl. Phys. 35**,** 825, 2002.

[6] I.V. ALEKSANDROVA et al. *An efficient method of fuel ice formation in moving free-standing ICF/IFE target.* J.Phys.D: Appl.Phys. 37, 1, 2004.

[7] E.R. KORESHEVA et al. *Development of a full-scaled scenario for repeatable IFE target fabrication and injection based on the FST technologies.* Report, 2nd RCM on Element of IFE Power Plants (November 4–7, 2003, IAEA Headquarters, Vienna, Austria).

[8] A.I. NIKITENKO et al. *Possible approaches to rapid control of IFE targets.* Report, 3rd IAEA RCM on Physics and Technology of IFE Targets and Chambers (October 11–13, 2004, Daejon, Rep. Korea).

CHAMBER

Possible approaches to rapid control of IFE targets

A.I. Nikitenko[1], I.V. Aleksandrova[1], S.V. Bazdenkov[1], A.A. Belolipetskiy[2], V.I. Chtcherbakov[1], E.R. Koresheva[1], I.E. Osipov[1]

[1] Lebedev Physical Institute of RAS, Moscow, Russian Federation
[2] Computing Center of RAS, Moscow, Russian Federation

Abstract. The goal of ICF microobjects characterization (such as polymer and glass shells, and cryogenic targets) is to provide reliable information within a definite time. From this viewpoint, the following two stages of producing the targets are of special interest: i. fuel layering technique development, which requires the most comprehensive information on the object (i.e. a 3D reconstruction of the microobject), ii. the fueling of a commercial power plant, requiring 500, 000 fusion targets each day or six fusion targets each second (i.e., this determine the values of some target parameters by which the target can be rejected during its injection). In this report we consider possible approaches exclusively meant for threshold target characterization, namely the application of algorithms for target characterization, based on low-projected tomography, and the application of methods of coherent optics based on Fourier holography for ultra-rapid target characterization. The results of computer experiments are presented. It is shown that (a) depending on the choice of rejection rule, it is possible to construct different threshold algorithms with different operational speeds, and (b) in the case of target quality control using holography method of image recognition, the operational time can be as short as ~1 μs. Therefore, target characterization during the injection process is possible.

1. INTRODUCTION

Characterization is the entire process for making precision measurements of ICF micro-object (such as polymer and glass shells, and cryogenic targets) parameters to ensure that a micro-object is within specifications. The following parameters must be measured and controlled: size, sphericity, non-concentricity, surface roughness, uniformity, etc. For cryogenic targets, to achieve implosion conditions the fusion fuel contained inside a hollow polymer shell must be formed as a highly uniform and smooth solid layer. The layers must meet the following requirements: fuel layer uniformity, concentricity and sphericity must be better than 1%, and fuel layer surface finish better than 0.1–1μm RMS [1]. Therefore, one of the basic issues of cryogenic target production is providing means for the precise and accurate knowledge of target parameters (of course, having in view the parameters of both the shell and the layer).

On the other hand, particular emphasis should be given to the fact that the fueling of a commercial power plant requires of ~500, 000 fusion targets each day, or 6 targets each second. This indicates that the development of rapid quality-control techniques is of critical importance. Thus, the goal of ICF/IFE target characterization is to provide reliable information within a definite period of time. From this viewpoint, the key issues and possible methods of target characterization can be stated as follows:

1) Individual target characterization

This refers to 3D target reconstruction, which requires the use of tomographic information processing methods [2]. At this stage of fuel layering technique development it is necessary to obtain the most comprehensive information on target quality and to certify the yield of the layering module.

2) Threshold target characterization

This refers to the determination of only a certain set of target parameters for rejecting the cryogenic targets without their detailed reconstruction. In the case in question, the most advanced control methods are based on the development of a new class of algorithms for threshold target characterization. It is necessary at the stage of fueling of a commercial power plant, when the characterization time plays a dominant role.

Therefore, in parallel with the activities relating to 3D target reconstruction, the possibility of accomplishing the threshold target characterization has also been analyzed [2]. We have started to develop the algorithms for fast and ultra-fast target characterization. The following is an indispensable condition for reactor-scale targets, providing specifics on:

(a) repeatable target characterization,
(b) in-flight target characterization.

Our recent work indicates that some methods of coherent optics are seen as an appropriate probe for examining the target quality in this case.

2. FOURIER HOLOGRAPHY APPROACH FOR FAST CONTROL OF TARGET PARAMETERS

Consider the optical scheme based on Fourier holography (Fig. 1). The identification signal in the scheme is proportional to the image correlation of the testing target and the etalon target. The signal enhancing corresponds to the better conformity between the testing and etalon targets. A combination of simple electrical threshold circuit and execution unit provides easy target selection. Obviously, the execution unit and photodetector only determine the operational time of the system, which can be as short as ~1 μs. A simulation model was developed in the form of a complete computer programme, *HOLOGRAM*. The shadow target images considered as amplitude transparencies were entered as model input. Fast two-dimensional Fourier transformation in this programme employs the library FFTW [3].

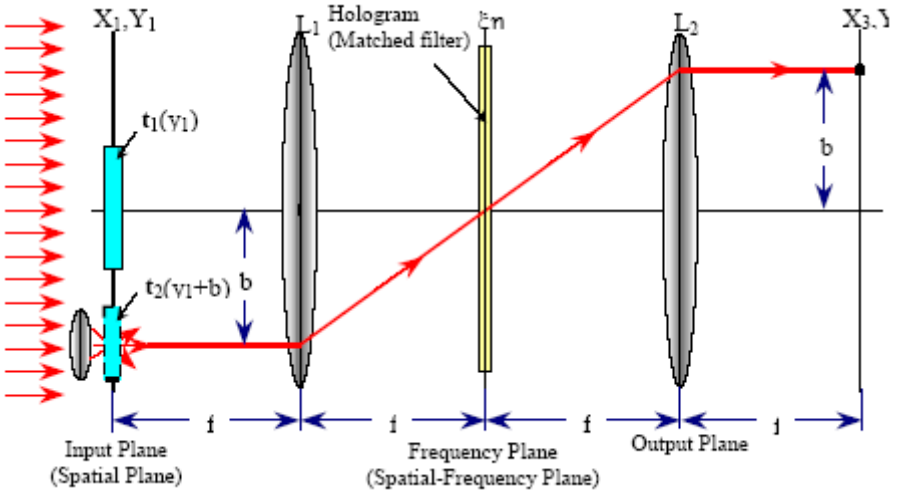

Figure 1. Optical scheme for obtaining Fourier holograms and operation of correlator with frequency plane.

The computer experiments using this programme have shown that it is possible to control the quality of both a single target and a target batch (Figure 2).

The next run of computer experiments was aimed at testing the sensitivity of the Fourier holography scheme in targeting shape perturbations. A set of cryogenic target images was created for using as input data for the *HOLOGRAM* programme. The thickness of the outer shell was 0.07 and that of the cryogenic layer 0.12 relative to the outer radius. The image dimensions were 1010 × 1010 pixel. The radial intensity distribution was chosen as close as possible to the real distribution, with an allowance made for the optical simulation data. The results obtained (Figs 3 and 4) show that it is possible to recognize the target shape perturbations in both low and high harmonics. The amplitudes in the figures are normalized to the amplitude of autocorrelation of the etalon image.

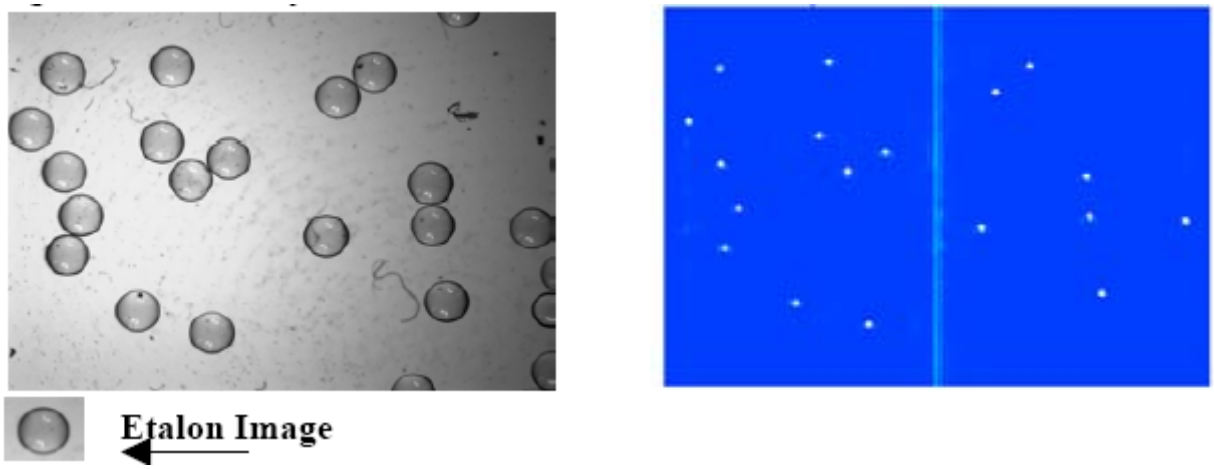

Figure 2. Holographic recognition of a target batch. The correlation peak position corresponds to shell positions in the upper photograph.

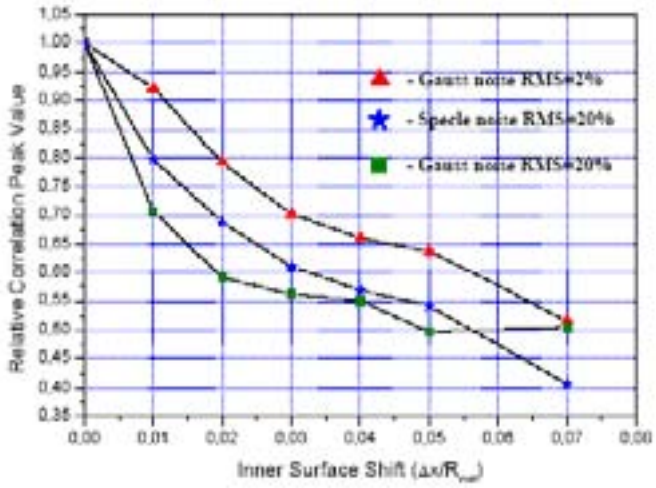

Figure 3. Relative amplitude of the correlation peak versus the shift of the inner surface of the cryogenic target.

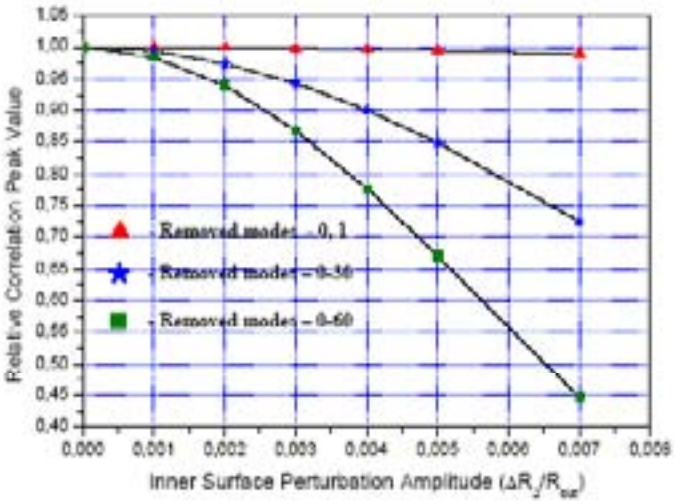

Figure 4. Relative amplitude of the correlation peak versus the shift of the inner surface of the cryogenic target.

When a target is injected into the chamber, two more important parameters should be controlled in addition to its shape, namely, the velocity and trajectory of the target motion. It seems promising to combine these measurements in one device. We have considered a solution of the problem assuming that target velocity is 200–300 m/s. We propose the optical scheme based on the Fourier holography (Fig. 5), which allows simultaneous control of the flying target quality, velocity and trajectory.

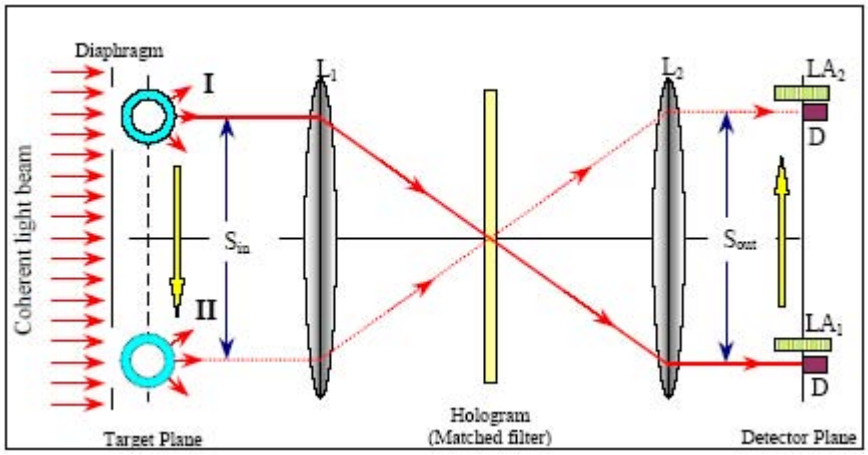

Figure 5. Schematic diagram of the device. Positions I and II are control points along the target trajectory; L1 and L2 are basic lenses; D1 and D2 are photodiodes; LA1 and LA2 are fast-response photosensitive line arrays. The arrows show the direction of the target and the correlation peak motion.

The time-lapse t, measured between the signal maxima from the first and second detector, determines uniquely the target velocity V = Sin/t. We assume that the target moves uniformly. If this is not the case and the target accelerates, the corresponding scheme becomes more complicated (it includes three or more detectors) and the calculation formula changes. This is not of principal importance, and we do not consider such situations for clarity. One can see that in the scheme under consideration the target velocity can be determined at the instant when the target passes position II. It can be assumed that the distance between positions I and II is 3 cm. In that case it will take target 10^{-4} sec to cover this distance. Such a time lapse can be easily measured, with high accuracy. For example, at the Time-to-Digital Converter

frequency of 109 Hz the accuracy equals 10^{-3} %. Figure 6 shows the possible electronic scheme for controlling the flying target trajectory. Presently, it is difficult to estimate the possible accuracy of determining the target trajectory because it obviously depends on a particular realization of mechanical, optical, and electronic components, and the algorithms of data processing. We could only assert that at the parameters given above it seemed possible to determine the target position in the plane perpendicular to its trajectory with an accuracy of ±2 μm. The corresponding angular shift of the target trajectory is approximately $\pm 2 \times 10^4$ radian. We considered the determination of the target trajectory in one plane only (the projection of trajectory to plane). It is obvious that for determining the trajectory in space we need two schemes (shown in Fig. 6) oriented in perpendicular directions.

3. CONCLUSION

Our computer experiments demonstrated that the Fourier holography scheme is promising for fast control of IFE targets. Its application will be topical, especially in cases where time is a critical factor, i.e., at the final characterization stage of the FST facility yield.

The next and overwhelmingly important step is the proof-of-principle study using a small-scale experimental facility for target injection and fast characterization. A schematic diagram of such a facility is shown in Fig. 7 (left). Some principal elements of the facility have been created at LPI (Fig. 7, right), i.e., the layering module (1), the test chamber (2) and the He-Ne laser as the light source (3). The module for fast characterization (4) is under development.

The facility will be capable of target acceleration under action of gravitational forces and its injection into the test chamber, followed by the fast control of target in-flight parameters.

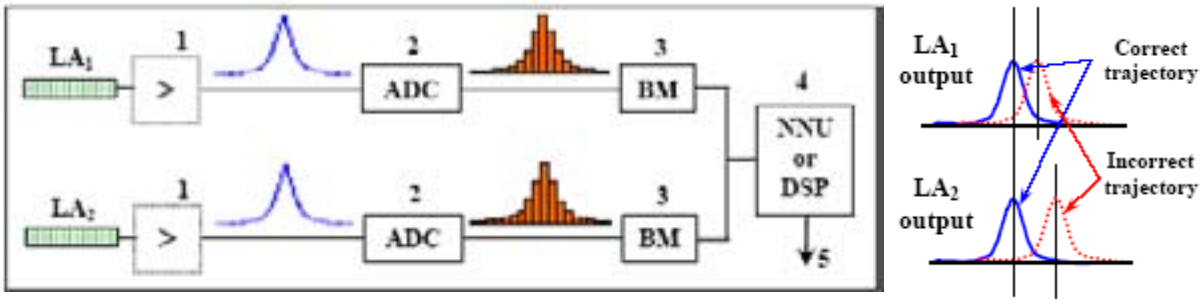

Figure 6. Schematic diagram of an electronic unit for analyzing the target trajectory. LA_1 and LA_2 are line CCD arrays; 1 is the amplifier; 2 is analogue to the digital converter; 3 is a buffer memory; 4 is a processor; 5 is the output signal for the units correcting the target trajectory. At the bottom it is shown how the vector of the target velocity can be determined.

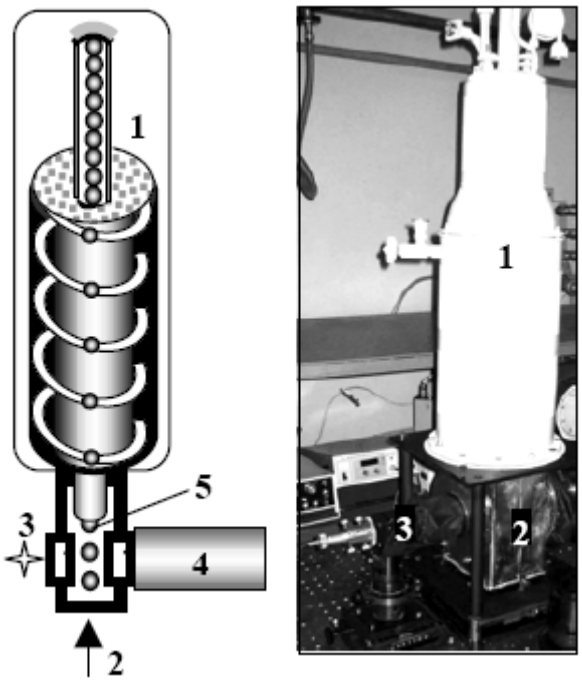

Figure 7. Experimental facility: 1- layering module, 2- test chamber, 3- light source, 4- module for fast characterization, 5- injecting target.

REFERENCES

[1] K.R. SCHULTZ et al. Nucl. Instrum. Methods A 464, 109, 2001.
[2] I.V. ALEKSANDROVA et al. J. Appl. Phys. D: 37**,** 1163, 2004.
[3] FFTW, User manual, http://www.fftw.org/

Investigation of SiC and PbMg target characteristics by the laser mass-spectrometer

R. Khaydarov, U. Kunishev, E. Tojihanov, M. Kholmyratov, G. Berdiyorov

Scientific-Research Institute of Applied Physics at the National University of Uzbekistan, Tashkent, Uzbekistan

Abstract: The progress in the field of science, such as nuclear and radiation physics, inertial thermonuclear fusion by multiply charged ions, radiationally resistant materials, etc., calls for the intensive study of the interaction of laser radiation with materials. In this connection it is important to investigate properties of SiC, which can be used in reactors for thermonuclear fusion, and PbMg plasma as a source of ions for synchrotrons. We discuss physical processes at the interaction of laser radiation with two element (SiC and PbMg) targets at different concentrations of the second component of the target, which leads to an increase in the duration of the impulse of ions of all charges and to the widening of energy spectra of ions of the main component of the target.

The progress in the field of science, such as nuclear and radiation physics, inertial thermonuclear fusion by multiply charged ions, radiationally resistant materials, etc., calls for the intensive study of the interaction of laser radiation with materials. In this connection it is important to investigate properties of SiC, which can be used in reactors for thermonuclear fusion, and PbMg plasma as a source of ions for synchrotrons. It is known that a laser source of ions provides for a larger intensity of a single-circle injection of multiply charged ions in synchrotrons. For the practical use of these sources of ions one should be able to extend the ions' impulse, keeping the charge and intensity of the ions unchanged. This effect can be reached by using multi-element targets. Therefore, in this work we investigate the physical properties of multiply charged plasma ions, formed under the action of laser radiation on two element (SiC and PbMg) targets, and in the latter case for different concentrations of Mg (n = 15%, 25% and 35% of the total target mass).

Mass-charge and energy characteristics of mono- and two-element laser-produced plasmas were studied by way of the mass-spectrometric method [1]. Neodymium laser (λ = 1.06 μm, E = 0.8–1 J, τ = 15 ns, average size of focal spot is ~10^{-4} cm^2) was used in experiments, which gave the power density of laser radiation as up to 10^{11} W/cm^2 at the surface of the target. The construction of the target chamber allows to place 10 targets with a diameter of 10 mm each and to change the place of interaction of laser radiation with targets.

The charge and energy spectra and quantitative characteristics of ions of mono- (Pb, Mg) and two-element (PbMg, α-, β-SiC) plasma at the intensity of a laser radiation of 5×10^{10} W/cm^2 on the target surface were obtained in experiments. It was found that the energy spectra of two-element laser-produced plasma (PbMg) were wider than the one of mono-element plasma. The energy diapason of ions increased with an increase in the concentration of Mg ions in the PbMg target due to the energy exchange between ions of different mass (called effect of "ions' fraction"). The interaction of ions with different mass led to a widening of energy spectra of both kinds of ions.

We discussed physical processes at the interaction of laser radiation with two element (SiC and PbMg) targets at different concentrations of the second component of the target, which led to an increase in the duration of impulses of ions of any charge and to a widening of energy spectra of ions of the main component of the target.

1. CHARACTERISTICS OF SIC MATERIALS WITH DIFFERENT MODIFICATIONS

SiC materials have a good resistance to high temperatures as well as to high radiation, and on the basis of these materials construction and fundamental materials are built for thermonuclear power engineering. In order to use these materials and alloys for ICF it is better first to study the influence of laser radiation and plasma ions on their physical characteristics. Therefore, we investigated the interaction of laser radiation with α- and β-type SiC targets and the formation and dynamics of the plasma ions generated by laser radiation with different intensity q. We obtained experimentally mass-charge spectra of plasma ions, and on the basis of these experimental data we got the energy spectra of ions, as the energy spectra give more information about physical processes in the plasma.

The experimental results obtained showed that both carbon and silicon ions, generated from the surface of both α-SiC and β-SiC targets, had wide energy spectra. Their energy spectrum has an energy interval with the characteristic values $E_{z,min}$ and $E_{z,max}$ and a maximum at some values of energy E_z. The maximum of energy distribution and intensity depended on the charge of ions and the nature of the target. The maximum value of energy spectra was defined by maximal charge multiplicity. The increase in charge multiplicity led to a shift of energy distribution to the high-energy region and to a decrease of its intensity in the ions. Fig. 1 (a-c) shows the typical energy spectra of ions of plasma generated on the surface of α-SiC (a) and β-SiC (c) targets, and on the SiC film of a 40 μm thickness (b) at $q = 5 \times 10^{10}$ W/cm^2. In the case of the α-SiC target (a), the maximum charge Z_{max} of C and Si ions was 2 and 4, respectively, and the maximum energy $E_{max} = 600$ eV. For the SiC film (b), $Z_{max} = 3$ for both kinds of ions, and E_{max} was decreased and equaled 450 eV. The energy spectra of β-SiC (c) plasma ions varied up to 750 eV, and the maximum charge of Si and C ions was $Z_{max} = 3$ and 2, respectively.

The total number of ions with different charges is shown in Fig. 2 for α-SiC (thinner curves) and β-SiC (thicker curves) targets obtained at $q = 5 \times 10^{10}$ W/cm^2. It is seen from this figure that the intensity of single-charged ions is higher than the intensity of ions with higher charges. In the case of α-SiC target the intensity of ions decreases with increasing the charge, while for the β-SiC target the intensity of Z = 3 ions is higher than the one of Z = 2 ions. These experimental results are a consequence of the fact that the nature of target influences the formation of the energy spectra and the charge of plasma ions, as well as the emission of multiply charged ions.

We also investigated the energy distribution of plasma ions increasing power density of the laser radiation from $q = 10^8$ W/cm^2 to 10^{11} W/cm^2, which led to the change of energy spectra of ions of different charge. It was found that the increase of power density of laser radiation mostly changed energy spectra in high-energy regions, where ions of high charge and energy were generated.

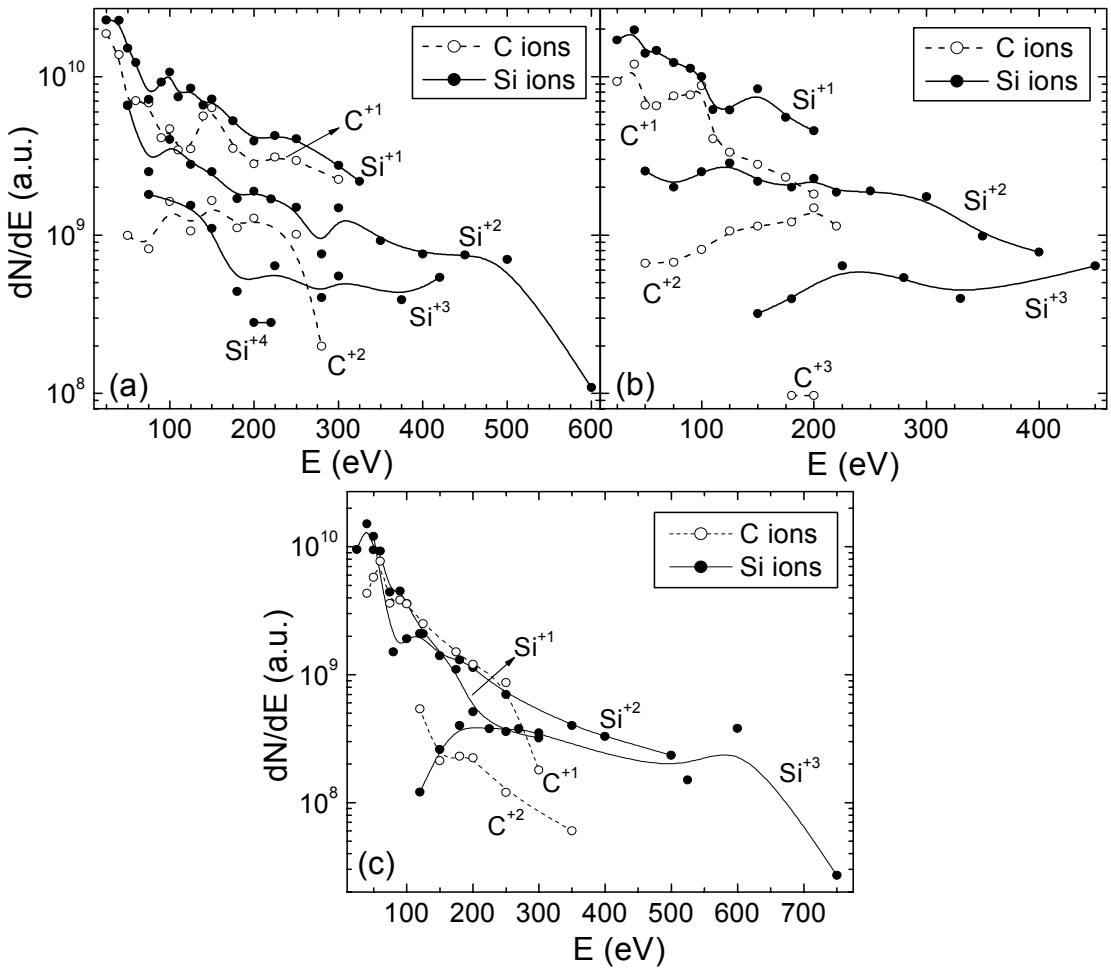

Figure 1. Typical energy spectra of SiC plasma ions obtained at $q = 5\times10^{10}$ W/cm^2 for α–SiC (a), for 40 μm thick SiC film on Si substrate (b), and for β – SiC (c).

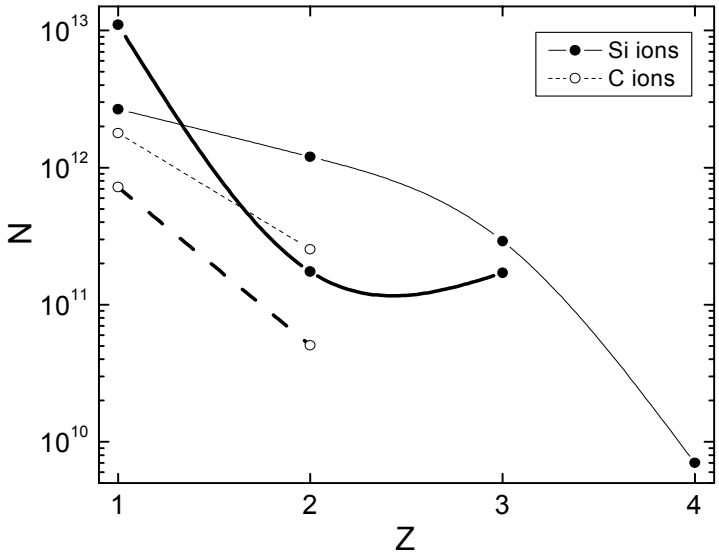

Figure 2. The total number of Si (solid curves) and C (dashed curves) ions as a function of ions' charge Z for α-SiC (thinner curves) and β-SiC (thicker curves) targets.

2. INTERACTION OF LASER RADIATION WITH PBMG TARGETS WITH DIFFERENT CONCENTRATIONS OF MG

Next, we investigated the physical properties of multiply charged ions, formed under the action of laser radiation on two-element (PbMg) targets at different concentrations of light Mg element (n = 15%, 25% and 35% of the total target mass). Experimentally observed mass-charge spectra of PbMg plasma ions for the different concentrations of light element showed that the plasma consisted of Pb and Mg ions and the increase of n led to a change in the mass composition of plasma and in the intensity of both kinds of ions. These changes were clearly seen at a relatively low energy of ions $E/Z \leq 80$ eV, as shown in Fig. 1 (a, b) for mono-(Pb) and two-element (PbMg) plasma (n = 35%) obtained at $q = 5 \times 10^{10}$ W/cm^2.

It is seen from this figure that the inclusion of light element into the plasma leads to a decrease in the charge of Pb ions and to an increase in the speed of these ions. Experimental results also showed that the maximum charge of ions of mono-element Pb (Mg) plasma equaled $Z_{max} = 5$ (4), while the maximum charge of Pb (Mg) ions from two-element PbMg plasma was $Z_{max} = 4$ (3). It was possible to detect Mg ions with a maximum charge of $Z_{max} = 3$ together with Pb ions with a charge of $Z_{max} = 4$ at the energy intervals 800–2500 eV for Pb ions and 250–800 eV for Mg ions. At relatively higher energies of ions ($E \leq 1000$ eV) peaks of Mg ions disappeared and peaks of Pb ions were clearly seen.

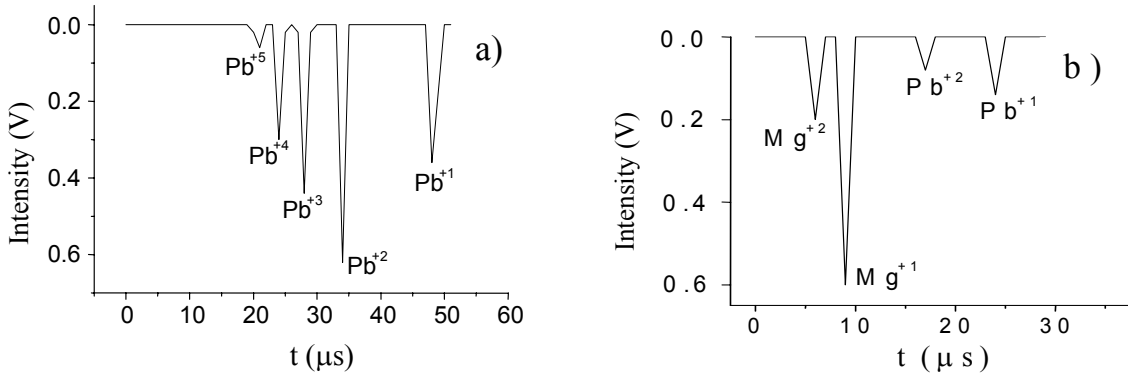

Figure 3. Mass-charge spectra of plasma ions obtained from Pb (a) and PbMg (n = 35%) targets at $q = 5 \times 10^{10}$ W/cm^2. The energy of ions is E/Z = 80 eV.

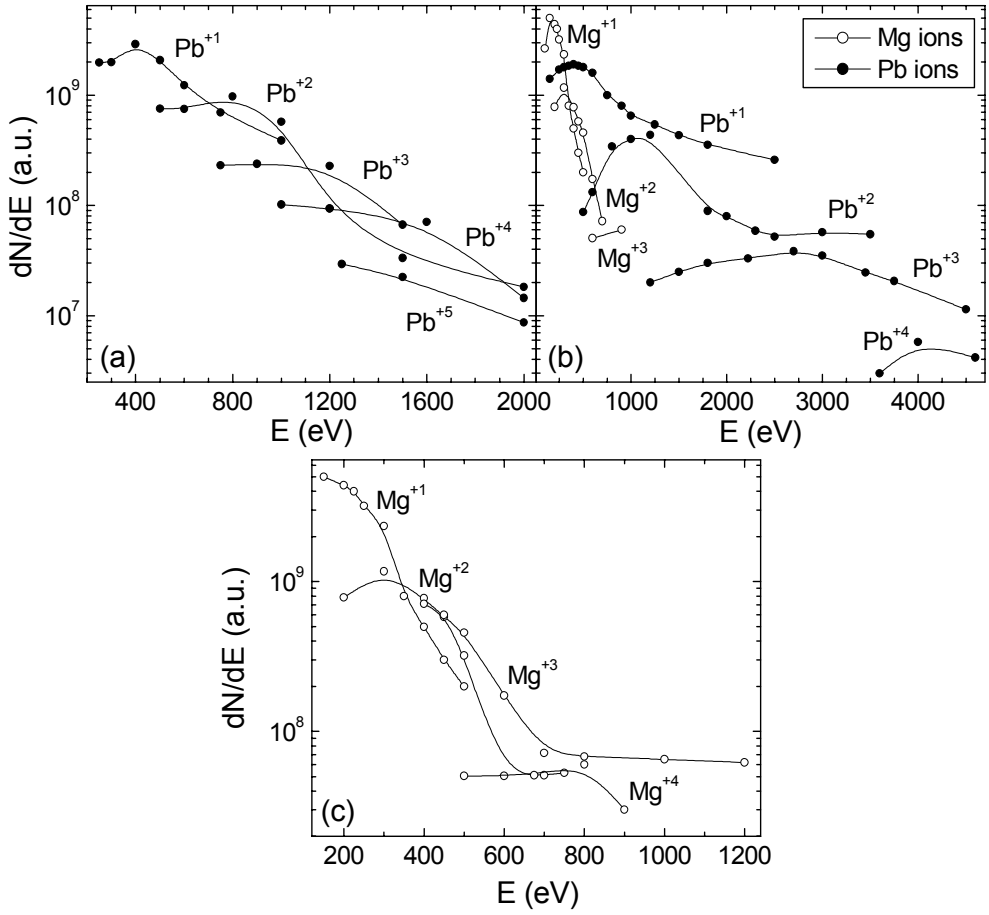

Figure 4. The energy spectra of ions from mono Pb (b), Mg (c) and two-element PbMg (b) plasma for the concentration of Mg n = 35%.

On the basis obtained from mass-charge spectra of ions of mono- and two-element plasma we plotted energy spectra of ions for different *n*. The energy spectra of mono Pb (a), Mg (v) and two-element PbMg (b) for *n* = 35% obtained q = 5 × 10^{10} W/cm^2 are given in Fig. 4. Ions of mono-element Pb and Mg plasma had an energy range of 2000 eV and 1000 eV, with a maximum charge of Z_{max} = 5 and 4, respectively. In the case of the two-element plasma, the Z_{max} of both kinds of ions decreased by a unit. The energy diapason of Pb ions increased (4500 eV), while the energy range of Mg ions decreased to 650 eV. We also found that for any concentration of Mg two packages of ions in different energy diapasons were clearly seen, and with increasing *n* the energy spectra of Mg ions decreased essentially and energy spectra of Pb ions increased to higher energies. To our knowledge, the increase in the energy range of two-element plasma ions in comparison to mono-element plasma is due to the change in recombination processes, which effect can be used to control the charge of ions and their intensity at a given charge.

The maximum E_{max} and minimum E_{min} energies and the total number N of Pb ions with Z = 1^{-5} is given in Table I for different concentrations of Mg ions. The results show that Pb ions with Z = 1,3 E_{max} increase with increasing *n*, while ions with Z = 2,4 E_{min} increase up to *n* = 25% and then decrease. For the E_{min} we see the nonlinear dependency on *n*. Such a tendency was found in Mg ions (see Table II).

Table 1. The maximum and minimum energies of Pb ions with Z = 1^{-5} for different concentrations of Mg.

Z	N	100% Pb	15% Mg	25% Mg	35% Mg	E, eV
1	$N_{max} = 8{,}5 \cdot 10^8$	950	950	1350	1600	E_{max}
	$N_{min} = 4 \cdot 10^8$	675	500	600	800	E_{min}
2	$N_{max} = 2{,}8 \cdot 10^8$	1275	2600	2700	1950	E_{max}
	$N_{min} = 8 \cdot 10^7$	1075	1200	1200	750	E_{min}
3	$N_{max} = 2 \cdot 10^7$	1880	3500	3500	4500	E_{max}
	$N_{min} = 1{,}2 \cdot 10^7$	1750	1680	1800	1200	E_{min}
4	$N_{max} = 2 \cdot 10^7$	4000	–	5380	3520	E_{max}
	$N_{min} = 1{,}2 \cdot 10^7$	3750	–	4380	3370	E_{min}
5	$N_{max} = 3 \cdot 10^7$	2000	–	–	–	E_{max}
	$N_{min} = 10^7$	1250	–	–	–	E_{min}

Table 2. The maximum and minimum energies of Mg ions for different concentrations of Pb.

Z	N	100% Mg	65% Pb	75% Pb	85% Pb	E, eV
1	$N_{max} = 2 \cdot 10^9$	337	337	537	400	E_{max}
	$N_{min} = 9{,}5 \cdot 10^8$	300	300	450	150	E_{min}
2	$N_{max} = 8{,}5 \cdot 10^8$	575	575	620	750	E_{max}
	$N_{min} = 2{,}3 \cdot 10^8$	225	225	150	300	E_{min}
3	$N_{max} = 6 \cdot 10^7$	700	850	830	630	E_{max}
	$N_{min} = 5 \cdot 10^7$	600	600	800	580	E_{min}

Table 3. Duration of Pb ion impulses for different concentrations of Mg.

Z	Δt, μs			
	100% Pb	15% Mg	25% Mg	35% Mg
1	4.9	8.7	9.7	7.4
2	1.8	6.6	6.9	9.8
3	0.6	5.3	4.7	9.8
4	0.4	–	1.1	0.26
5	4.2	–	–	–

Table 4. Duration of Mg ion impulses for different concentrations of Pb.

Z	Δt, μs			
	100% Mg	65% Pb	75% Pb	85% Pb
1	2.3	2.3	2.8	2.2
2	1.8	1.8	2.9	1.5
3	2.2	1.6	1.46	1.2

The duration of Pb and Mg ions is shown in Tables III and IV for different concentrations of the second component of the target. It is seen from these tables that with increasing the concentration of the second element of the target the flight time of ions increased, and it led us to assume that the flight speed of plasma depends on an average mass

$$m_{av} = \frac{m_{Pb} n_{Pb} + m_{Pb} n_{Mg}}{n_{Pb} + n_{Mg}}$$

where m_{Pb} and m_{Mg} are masses of target elements and n_{Pb} and n_{Mg} are their concentration. For the given intensity of laser radiation q the total number of ions is constant $(n_{Pb} + n_{Mg}) = \text{const}$. Using the dependency of the maximum speed of ions on mass [10] $u_{\max} \sim 1/\sqrt{M}$, we can find the maximum energy of ions at a given charge Z.

Figure 5 shows the intensity of Pb ions as a function of the concentration of Mg ions. It is seen that the intensity of Pb ions with a charge of $Z \leq 3$ increases with increasing n, while the intensity of Pb ions with a charge of $Z = 4$ does not depend on n.

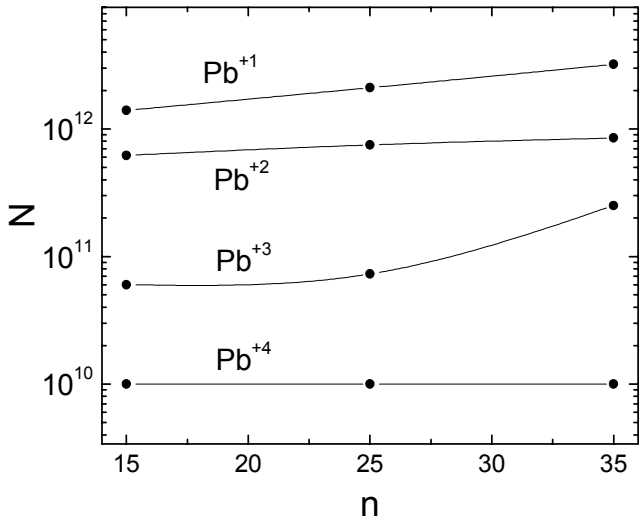

Figure 5. Intensity of Pb ions N as a function of the concentration n of Mg at $q=5\times10^{10}$ W/cm^2.

The enlargement of energy spectra to high energies and the presence of the maximum in spectra show that processes in two-element plasma can be considered to occur in two stages. In the first stage (up to the maximum of distribution) intense ionization takes place, entailing an increase in multiply charged Mg and Pb ions, included in the target in different concentrations. The second phase (after the maximum) is characterized by an increase in recombination processes, i.e., by an energy exchange between light (Mg) and heavy (Pb) ions of plasma. The results of our experiments led us to the conclusion that the formation of charge and energy spectra of multiply charged ions in two-element PbMg plasma is defined not only by the ionization and recombination processes but also by the mutual interaction of ions of different mass in the plasma. In Ref. [14] theoretical calculations were given on the interaction of particle masses which differ by a unit of mass. In that case the cross section of interaction was defined as $\sigma \approx 1{,}396 \cdot \frac{Z^4 \cdot e^4}{(k \cdot T)^2}$. In our case the situation is more complicated because the masses of the plasma components are different and their mutual interaction should be taken into account. The authors of Ref. [15] defined the energy of ions in multi-component plasma $E_k \sim Z_k^2/m_k$, where Z_k и m_k is charge and mass of the ions. The results of our experiments may be illustrated by the theoretical calculations given in Ref. [14], which

show that in such cases the collisional limit of speed of all plasma components is equal, energy does not depend on the charge but becomes proportional to the mass, i.e., $E_k \sim M_k$.

3. CONCLUSIONS

To summarize, we investigated the interaction of laser radiation with two-element SiC and PbMg targets and the formation of mass-charge and energy spectra of multiply charged ions for different target configurations and intensity of laser radiation. We showed that plasma ions from targets of the same SiC material, but with different characteristics, have different energy spectra and intensities, which shows the strong influence of the nature of the target on the plasma ions. Results of experiments in the study of two-element PbMg ions show that with the increasing concentration of Mg, the energy spectrum of ions will increase more than two times due to the exchange of energy between light and heavy ions. The intensity of Pb ions of all charges increases with the increase in the Mg concentration, though the character of the change in intensity does not depend on the concentration. The increase in the intensity of laser radiation mostly changes energy spectra in high-energy regions where ions of high charge and energy are generated.

REFERENCES

[1] M.R. BEDILOV, R.T. KHAYDAROV et al., Plasma Phys., 26, 862 (2000).
[2] YU.A. BIKOVSKIE, B.YU. SHARKOV et.al., Fiz. Plasmy (Moscow), (1977) 3, 1153.
[3] A.V. GUREVICH, L.P. PITAEVSKIY, Voprosy teorii plazmy, (Moscow) Atomizdat, (1980).
[4] S.I. ANISIMOV, M.R. IVANOV et.al., Sov. Phys. Plazmy, (1982) 8, 1045.
[5] M. OGAWA, M.YOSHIBA et.al., Laser and Particle Beams, (2003) 21, 633–638.
[6] M. YOSHIBA, M. OGAWA et al., Nicl. Instrum. Methods, (2000) B 161–163, 1104–1107.
[7] B.YU. SHARKOV, S. KONDRASHEV et.al., Rev. Sci. Instrum, (1998) 69, 1035–1039.
[8] V.I. GUSHENETS, E.M. OKS et al., Laser and Particle Beams (2003), 21, 123–138.
[9] A. SEMEROK, B. SALLE et al., Laser and Particle Beams (2002), 20, 67–72.
[10] F. OSMAN, YU CANG et al., Laser and Particle Beams (2004), 22, 83–87.
[11] RAI.VIRENDRAN, P. JAGDISH et al., Laser and Particle Beams (2003), 21, 65–71.
[12] M.R. BEDILOV, R.T. KHAYDAROV, I.YU. DAVLETOV, Plasma Phys. (1995) 21, p.1007.
[13] A.I. MAGUNOV, A.YA. FAENOV et al., Laser and Particle Beams (2003), 21, 73–79.
[14] A.F. RAFFRAY, D. HAYNES, F. NAJMABADI, Journal Nuclear Materials (2003), 23–31.
[15] M.R. BEDILOV, M.S. SABITOV et al., Fiz. Plasmy (Moskow), (1987) 13, 585.

IFE chamber wall ablations with high-flux pulsed beams including ions and UV laser lights

K. Kasuya[1], T. Norimatsu, S. Nakai[2], A. Prokopiuk[3], W. Mroz[3]

[1] Department of Energy Sciences, Tokyo Institute of Technology, Yokohama, Japan
[2] Institute of Laser Engineering, Osaka University, Osaka, Japan
[3] Institute of Optoelectronics, Warsaw, Poland

Abstract: Simultaneous measurements of intense proton beam diode and ablation characteristics were successfully performed. A newly operated diode could recently produce intense Xe, C and Si beams. The present results of experimental investigations concerning the laser-created crater shapes in different materials suggest that the main mechanism of the absorption of ArF laser radiation is photochemical absorption. In the case of low melting-point materials, and with the accumulation of a large number of laser shots in one place, the flow of molten materials appeared around the crater which is supposed to be a thermal effect. Our present results also suggest that a small part of such short-wavelength ArF laser is absorbed by the classical absorption mechanism.

1. INTRODUCTION

Two kinds of experiments were performed to observe the characteristics of a pulsed intense ion beam and a UV laser beam. The former particle beam species was a proton and the latter laser was an ArF laser. These beams were used for the IFE first wall ablation. Our interest in the use of these beams arose from the modeling of the first wall ablation out of the candidate inertial fusion materials [1].

To understand the precise relation between the thickness of the ablated surface layers made of various materials and the proton beams used to ablate the targets, it is necessary to know (in-situ) the precise characteristics of the focused proton beams under irradiation. We produced such proton beams with one of our pulsed power machines in Japan, measuring current and voltage characteristics at the focal point. Half of the focused proton beam was used for this kind of measurement, while the other half of the same beam was used to ablate the sample targets. With this method we could investigate without much ambiguity the precise relation between the exact beam condition and the ablated thickness.

The first-named author brought various sample materials to Warsaw, and an ArF laser in the Polish authors' laboratory [2] was used to irradiate the samples. After irradiation, the sample surfaces were examined with various diagnostic tools, including a laser microscope (Olympus-LS1200) in the Analysis Center of the second Japanese author (at ILE-Osaka University).

The most important data were the first wall ablation rates obtained under different experimental conditions with different beams, while in some cases the surface species changes under successive beam irradiations were also of interest. All results of the experimental were gathered and compared with our former results [3–6], for the compilation of a future database on IFE reactor designs. The details will be presented during the Technical Meeting.

Many issues have yet to be clarified before we can design more advanced versions of IFE reactor chambers in the near future. These issues change sometimes as the results of new concepts for the target implosion schemes. Most recently, the fast ignition scheme introduced new ways of the production of neutrons, X-ray and ion beams as a result of target implosions.

Although the neutrons share the highest rate of fusion burn energy, they are not captured by the first walls facing the targets, and almost all parts of the energy must be transformed into heat within the thick blankets behind the first walls. On the contrary, the peak power of the X-rays is highest among the energy sharers, although the shared energy itself is lowest. The second energy transporters are the ion beams accompanied by co-moving electrons, almost all energy of which is transformed into heat within the very thin layers of the first walls facing the targets. The rate of the wall ablation thickness with these ion beams is highest among the three components. Thus we tried to make the first contribution to the database on ion beams in this article. The ablation with laser light is also important because the laser light hits the tail cone of the fast-ignition laser-driven target and the reactor chamber wall in the case of an accident.

2. INTENSE FLUX BOMBARDMENT OF THE CHAMBER WALL WITH IFE TARGET IMPLOSION

A few examples of direct irradiation targets are shown in reference [1–6]. In the case of 400 MJ fusion energy output per shot [4], the energy partitions among the neutron, ion beams, alpha particles and X-ray are 82.0%, 14.5%, 2.5% and 1.0%. As for the energy partitions among the ion species, the Carbon ions seem to be most dominant, while the Deuterium and proton ions are next in line. If these results are correct, it is necessary for us as first priority in this field to investigate the Carbon beam ablation of the wall materials. The second is the Deuterium ablation, and then the proton ablation.

3. SIMULTANEOUS MEASUREMENTS OF BEAM AND ABLATION CHARACTERISTICS

There were shot-to-shot characteristic changes in the proton beams produced to irradiate the targets. To avoid any ambiguity we tried to make simultaneous measurements of the beam and the ablation characteristics. Figure1 shows the schematic diagram of the experiment. Two parts were extracted from the converging ring-shaped proton beam with two beam apertures. One part was used to measure the beam current density with a biased ion collector, while the other part was used to simultaneously irradiate the target. The beam apertures were placed at a distance from the focal point (in front of the focal point).

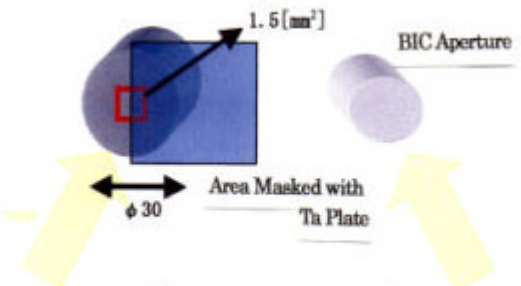

FIG. 1 Schematic Diagram of Proton Beam Irradiation

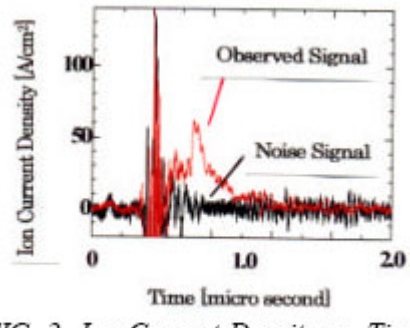

FIG. 2 Ion Current Density vs. Time

The diameter and the thickness of the graphite target were 30 mm and 5 mm. After the beam irradiation, the surface of the target with an area of 1.5 mm^2 was observed with a laser microscope (Keyence VK-8550 in our diagnostic center at our TI Tech main campus). The spatial resolution of the microscope was 1.46 micron along the 3D axes. Half of the irradiated surface was covered with a Ta masking plate.

The current density profile vs. time of the proton beam is shown in Fig. 2. Although the noise level was high, we could distinguish the beam current signal from the noise. Table I summarizes the beam characteristics observed in our experiment.

TABLE I: OBSERVED PROTON BEAM CHARACTERISTICS

Peak Ion Current	2.00 kA
Peak Ion Current Flux	~200 A/cm^2
Pulse Width	~400 ns
Total Ion Flux	2.75x10^{19} /cm^2
Energy Flux	11.0 J/cm^2

With the laser microscope, we could obtain a 3D image of the graphite surface, which is shown in Figure 3. The left lower half is the area irradiated by the beam, while the right upper half is the original surface without beam irradiation. With the software of the microscope, we could estimate the ablated thickness of the surface irradiated by the proton beam. In this case the over-all ablated thickness was 13.3 micron. More details about the ion beam ablation results are described in our other paper [1], as there is not enough space here.

A Thomson parabola ion spectrum analyzer was used to record the ion tracks on a small plastic plate similar to CR-39. After the surface etching of the plastic with a 6N-NaOH water solution at 70^{o}C for 2 hours it was found that the beam species, the beam charge state and the mean beam energy were H+, 1 and 241 keV. We assumed that the beam had a Gaussian shape of energy spectrum with the half-width of 29.8 keV. The energy spectrum distribution of the beam is shown in Figure 4.

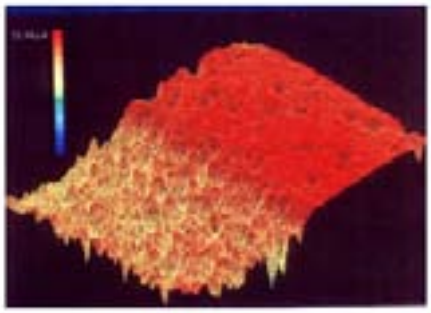

FIG. 3 3D Image of Graphite Surface

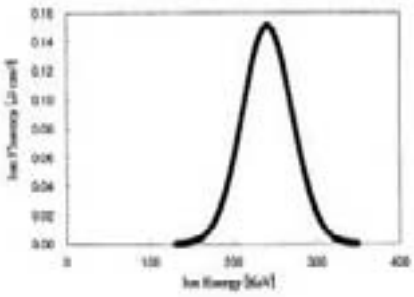

FIG. 4 Beam Energy Spectrum

4. OBSERVATION OF VARIOUS MATERIAL SURFACES IRRADIATED AND CRATERED WITH FOCUSED ARF LASER LIGHTS

It is necessary to know the ablation rates of various material surfaces under irradiation from intense UV laser lights, as one of the ablating beams, when designing the future inertial fusion reactors driven by big lasers. Thus we irradiated various materials with a UV laser light. The laser wavelength, the pulse width and the maximum repetition rate were 193 nm, 20 ns and 50 Hz. The materials irradiated were LiPb and Pb as wet-wall candidates for inertial fusion reactors, while W, C, Al_2O_3, SiC and SiC-Si composite materials were also irradiated as dry-wall candidates. The changes in the condition of the irradiated surface under different irradiation conditions were observed with three different kinds of optical diagnostic tools. The structures of the produced craters were precisely investigated. We could show how resistant Tungsten was against such laser ablations, compared to LiPb or Pb, etc.

4.1 Purpose of ArF Laser Experiments

Without knowledge of the ablation rates of candidate materials for wall and target it is not possible to design reactor chambers for inertial fusion energy (IFE) power plants. An example of a fast ignition laser IFE target design contains a tail cone to guide the intense fs laser light into the central ignition region. The cone material(s) is (are) supposed to be one or two of the LiPb, Pb and gold, which match better with the reactor wall. We must also take account of the various cases in which intense short-wavelength laser lights impinged on such candidate material surfaces in consecutive normal and abnormal (accidental) situations.

The UV lasers with short wavelengths, such as KrF (248 nm), ArF (193 nm) and F_2 (157 nm) lasers, make it possible to use such laser radiation for different applications in pulsed laser deposition and laser micro-fabrication, as well as to start experiments on the investigation into the interaction between intense UV laser radiation and material surfaces [2, 7].

In the case of the KrF laser with a photon energy of 4,99 eV, we can observe (dependent on laser fluency [laser power density] on the target) the effects of the classical ("inverse bremsstrahlung") absorption, as well as of multi-photon absorption and absorption through the excited levels.

Effects of different absorption mechanisms are visible, e.g., during the laser deposition of thin films. With low laser fluencies, the deposited layers are smooth, without any droplets of debris, while, from a laser fluency of about 8 J/cm^2 onwards, some droplets appear in the deposited layers. In the case of film deposition with the ArF laser, the thermal effects caused by classical absorption are not visible with moderate laser fluencies. The photon energy of ArF laser radiation (6,42 eV) is high enough to increase the probability of multi-photon absorption and absorption through the excited levels, which fact makes these two processes the dominant absorption mechanisms. A comparison of the quality of thin films made of hydroxylapatites and deposited with KrF and ArF lasers, is made by the authors of this article in another paper.

In the case of F_2 lasers, the photon energy is higher than in that of ArF lasers, and the efficiency of non-classical absorption mechanism is greater than in the case of ArF laser radiation. However, as the present F_2 laser output energy per pulse is much lower than other UV laser energies, the F_2 laser is not often used in laboratory investigations.

In our article we are presenting results of the interaction of ArF laser radiation with high laser fluencies. The depth of the laser-produced craters was precisely observed with three different kinds of diagnostic methods. The first one was a laser microscope. The highest spatial resolution was obtained under high spatial multiplication, although only the average value covering a rather large area of the craters could be distinguished in applying different materials under different irradiation conditions. If the average was taken within a smaller area, the background noise level was too much to observe the real value. The second method was a digital microscope with a conventional light source, with which we could take easily three-dimensional crater photographs with the highest reality. The third method was a laser displacement counter with a precision motor-drive locater, with which we recorded the depth and height of the crater and wall along a rather narrow traverse line on the surface. The images obtained with these different methods of various material surfaces were compared in detail.

4.2 Experimental Procedure

An ArF laser was used to shoot at targets at an angle of 10^{o} to 45^{o} as compared to the normal angle to the target surface. The sample targets were placed on a movable X-Y-Z holder driven by precision step motors in a vacuum chamber. The vacuum pressure inside the target chamber was about 2×10^{-5} Pa. The maximum output energy of the laser was about 650 mJ, while the size at the laser focus was 0.07×0.17 cm^2. The laser radiation was focused onto the investigated materials by a spherical CaF^2 lens of f = 350 mm, with anti-reflection layers. The distance between the laser light source and the focal point was ~270 cm. Although the laser beam was guided through a vacuum of $p \sim 3 \times 0^{-5}$ torr, high energy-losses (at least 50%) were observed. The energy losses were caused mainly by the three optical elements: (1) the entrance CaF_2 vacuum window, which cut off the vacuum tube near the laser source, (2) the focusing lens and (3) the second CaF_2 window, which prevented the lens from material surface deposition. A part of the laser energy was also absorbed in the residual gas in the guide tube between the laser and the target chamber. The laser fluency was alternated between 15 J/cm^2 and 25 J/cm^2, and the repetition rate of laser was changed from 1 Hz to 50 Hz. The maximum number of laser shots per one spot on the irradiated samples was 2×10^{5}. Irradiated materials were LiPb and Pb as wet-wall candidates for inertial fusion reactors, and W, C, Al_2O_3, SiC and SiC-Si composite materials were irradiated as dry-wall candidates.

The first-named author provided the fourth- and fifth-named authors with various sample materials, and an ArF laser (Lamdaphysik-LPX305i) in their laboratory was used to irradiate these samples. After irradiation the sample surfaces were observed with a laser microscope (Olympus-LS1200) in the Analysis Center of the second- and fourth-named authors, and with a few depth-meters of different kinds (TI Tech), and so on.

It is a simple consideration that the normal incidence of laser light on the target surface is preferable for utilizing the laser energy as effectively as possible for the maximum ablation of the surface. On the contrary, the absorption of laser light by the ablated plumes becomes more intense if the incident angle decreases. This effect is strengthened when the repetition rate of the laser light increases. More quantitative comparisons with the results of the experiments are required.

4.3 Results of Experiments

Results obtained through experiments can be divided into two groups, as follows. The first group is composed of materials with a low melting point (LiPb, Pb), the second of materials with a high melting point.

Fig. 5. 3D-image of LiPb crater.

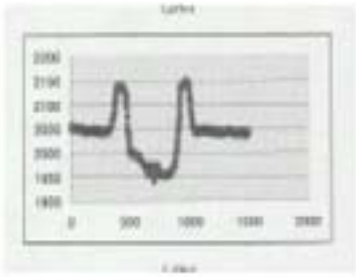

Fig. 6. 1D-plot of LiPb crater.

Fig. 7. 2D-image of LiPb crater.

The materials with a low melting point were irradiated by laser radiation with the high fluency of 25 J/cm^2, at an angle of 10^o with respect to the angle normal to the target surface and with a repetition rate of 10 Hz. Figure 5 shows part of the three-dimensional crater with a visible droplet of the re-molten LiPb target after the 10^3 laser shots. The visualization of the partial crater was done with a digital microscope (Keyence, VHX-100 Model). In the course of successive laser irradiations the surface was heated to a temperature exceeding the melting temperature. The flow formed a typical crater with walls higher than the original surface of the irradiated samples (Figure 6). To obtain these pictures, we used a combined diagnostic tool with two elements, (1) a laser displacement counter (Keyence, LE-4010 Model) and (2) a motor-driven precision locater (COMS, MAP-1EM 50X Model). Within almost the entire area of the crater bottom the bright molten structure was observed, as shown in Figure 7, which was obtained with the above digital microscope.

A more detailed surface investigation was made with a laser microscope (Olympus, LS1200 Model). The average depth of the Pb craters, irradiated under the same conditions as the above LiPb, is shown in Figure 8 as a function of the total number of accumulated laser shots**.** A near proportionality between the depth and the total number of laser shots was observed at the left-bottom corner in the same figure, while a departure from that proportionality set in after the number of two hundred. This fact revealed that the conditions for laser absorption and laser ablation of the irradiated material were turned around at this number. The reason for this change may be a partial melting/re-melting of the crater bottom. In the case of Pb targets, we observed craters with flow-associated walls similar to the LiPb ones.

In the case of Tungsten targets, the above proportionality continued until a total number of 10^4 laser shots (Figure 9). When we concentrated 10^5 laser shots on one place, we also observed a slight difference from the proportionality. At the bottom of Figure 10, an average crater depth is plotted as a function of the distance along the vertical axis on the surface image of the central part of that figure.

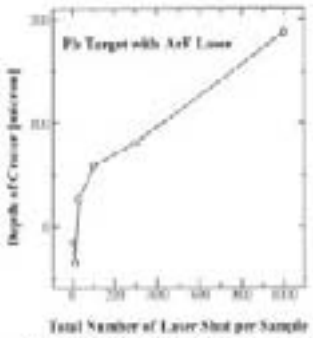

Fig. 8. Crater depth vs. laser shot number for Lead.

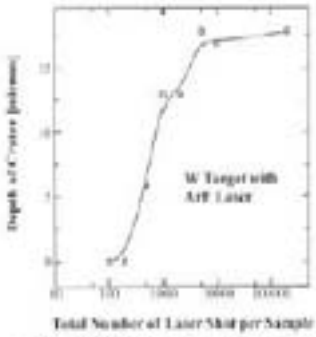

Fig. 9. Crater depth vs. shot number for Tungsten.

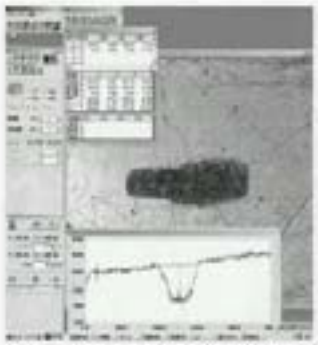

Fig. 10. 1D and 2D images of Tungsten, observed by a laser microscope.

This was obtained after10^4 laser shots in one place. In the same experiments with Tungsten targets we could not observe such walls around the craters, which were formed by the molten material flow. Here we also used the laser microscope. A different kind of diagnostic result with the same microscope is shown in Fig. 11, which represents the 3-dimensional plot of a tungsten crater without any material flow around it. We observed a similar crater shape (without the material flow) after 10^5 laser shots in one place, as the above-mentioned departure from proportionality was slight.

An Al_2O_3 ceramic was also irradiated at an angle of 10^o with respect to the one normal to the target surface, with a laser repetition rate of f = 50 Hz and an average fluency of 15 J/cm^2. After 10^5 laser shots concentrated on one place, a crater was formed with a wall higher than the original surface before laser irradiation (Fig. 12). Since the melting point of Al_2O_3 ceramic is very high (2,050^{o}C) and the wall material is supposed to be aluminum, such a crater could be produced. Here the oxygen within the Al_2O_3 was supposed to be ablated and move far away from the original surface, although the aluminum was expected to remain on the original surface. This was due to the fact that, after the chemical bindings were broken, the ablated oxygen in gas condition was more mobile than the solid or liquid aluminum. It could escape from the crater more quickly than the aluminum. The melting temperature of aluminum is 660.4^{o}C, which means that within the period of the accumulated 10^5 laser shots the temperature at the crater bottom exceeds the melting temperature of aluminum.

The C, SiC and SiC-Si were irradiated at an angle of 10^o with respect to the normal angle to the target surface, with a laser repetition rate of f = 10 Hz and an average fluency of 15 J/cm^2. Under these experimental conditions we could not observe any thermal (melting) effects.

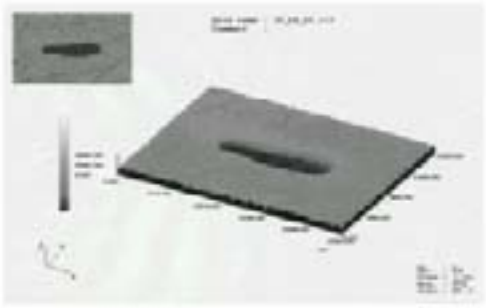

Fig. 11. Bird-eye-view of Tungsten crater.

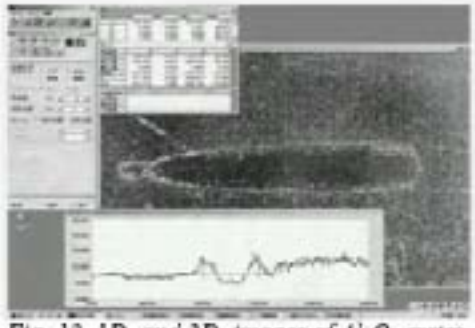

Fig. 12. 1D- and 2D- images of Al_2O_3 crater.

5. DEVELOPMENT OF NEW ION SOURCES FOR TARGET IRRADIATION

5.1. Cryogenic Diode with Compact Cryogenic Cooler

A new cryogenic diode with a compact cryogenic cooler was designed and operated very recently to produce pure, highly efficient beams of high brightness for target irradiation, specifically for the purpose of chamber wall ablation. The cross-sectional view of the diode and the preliminary temperature history vs. time after the start of operation will be discussed elsewhere after we got clearance by the collaborating US Laboratories. Xe beams were produced with this cryogenic ion driver.

5.2. Production of Medium-mass Ion Sources Including C and Si

Room-temperature diodes for the production of carbon and silicon beams were newly proposed, and initial experimental results were obtained. DLC (diamond like carbon) film and silicon wafers could be used in our intensely pulsed ion diodes. The micro-divergence angle of the Si ion beam on the anode surface was obtained in our first experimental demonstration.

6. SUMMARY

Simultaneous measurements of intense proton beam diodes and ablation characteristics were successfully performed. Newly operated diodes could recently produce intense Xe, C and Si beams. Present results of experimental investigations concerning laser-created crater-shapes in different materials suggest that the main mechanism for the absorption of ArF laser radiation is photochemical absorption. In the case of materials with a low melting point, and of the accumulation of a large number of laser shots in one spot, a flow of molten materials appears around the crater, which is supposed to be a thermal effect. Our present results also suggest that a small part of such short wavelength ArF laser is absorbed by the classical absorption mechanism.

ACKNOWLEDGEMENTS

The authors acknowledge the following persons and foundations for their support during this study. Many kinds of materials to be irradiated with the beams were endorsed by several groups in Japan and the USA. This study was sponsored by (1) IAEA, (2) The Ministry of Education, Science, Culture, Sports and Technology in Japan, (3) ILE, Osaka University, (4) the Japan Society for the Promotion of Science, and (5) TI Tech. The work was performed under the IAEA Coordinated Research Project on "Elements of Power Plant Design for Inertial Fusion Energy", RC-845-F1.30.08, Vienna, Austria, and the 2001-2003 US-Japan Collaboration Project in the Field of Nuclear Fusion on "Wear and Tear of Reactor Wall Materials with High Flux Ion Beam and Pulsed X-rays" between SNL and TI Tech. The international collaboration project between Japan and Poland was supported by the Centennial Memorial Foundation of the Tokyo Institute of Technology and the EUREKA E 2841 ADVANCED PLD Project, sponsored by the State Committee for Scientific Research of Poland.

REFERENCES

[1] K. KASUYA, A. KASAMATSU, T. RENK, C. OLSON et al., J. Nuclear Materials 313–316 (2003), pp. 235–238.
[2] W. MROZ, A. PROKOPIUK, B. MAJOR, K. KASUYA et al., Applied Surface Science 197-198 (2002), pp. 371–375.
[3] K. KASUYA, S. ARAYA, T. KAMIYA, Proceedings of the 14th International Conference on High-Power Particle Beams and the 5th International Conference on Dense Z-Pinches, June 23-28, 2002, Albuquerque, NM, USA, (2002), pp. 425–428.
[4] K. KASUYA, T KAMIYA, W. MROZ, T. YAMANAKA, S. NAKAI, ibid., (2002), pp. 433–436.
[5] K. KASUYA, T. RENK, C. OLSON, T. NORIMATSU, T. NAGAI, T. YAMANAKA, S. NAKAI, ibid., (2002), pp. 429–432.
[6] K. KASUYA, T. RENK, C. OLSON, ibid., (2002), pp. 437–440.

Chamber clearing study relevance to Z-pinch power plants

P. Calderoni, A. Ying, M. Abdou

Fusion Engineering Science, Mechanical and Aerospace Engineering Department, University of California Los Angeles, Los Angeles, California, USA, United States of America

Abstract. This paper presents the work recently conducted at UCLA for the Z-pinch vapour clearing study. The superheated flibe vapour generated by a high-current, pulsed electrical discharge expands inside a temperature-controlled chamber and condenses in contact with the liquid. Vapour clearing rates are evaluated from the measured pressure history with the presence of argon gas pressure. The results show that the condensation decay time varies from 2.65 to 4.01 ms as argon gas pressure increases from 2 to 20 torr. These initial results suggest that there appears to be a large design window for Z-pinch vapour clearing even in the presence of an argon gas pressure of 20 torr.

INTRODUCTION

Recent rapid progress on high energy pulsed power capability and the development of a repetitive z-pinch power plant concept have made z-pinches one of the three major driver candidates for inertial fusion energy (IFE). In particular, its target's high yield (3 GJ versus 350 MJ for heavy ion fusion [HIF] as shown in Table 1 [1, 2]) potentially allows the chamber to be economically operated at 0.1 Hz, which relaxes significantly the chamber clearing requirements. The mainline z-pinch power plant approach uses a thick-liquid flibe wall chamber to eliminate the conventional solid-first-wall problem and an indirect-drive target. The Z-pinches and HIF share a strong commonality in that they both use indirect-drive targets and a thick-liquid chamber. However, to mitigate the shock from the blast, the Z-pinch chamber is filled with a modest 10 to 20 torr of an inert gas such as Ar, in contrast to a near hard vacuum chamber in a heavy ion fusion (HIF) power plant. In a previous study of vapour clearing rates under hard vacuum conditions, chamber clearing has been characterized by an exponential decay with a time constant of 6.58 milliseconds. This result implies that condensation rates of flibe vapour are sufficiently fast to satisfy Z-pinch power plants' repetition rates. However, it is well known that the non-condensable, heavy gas molecules can inhibit the condensation process through the accumulation of an interfacial gas layer near the interface and the formation of interfacial mass transfer resistance. The objective of this research was to investigate whether the presence of 10 to 20 torr Ar background gas can have a detrimental effect on the vapour clearing rate and to quantify the flibe vapour clearing decay time as a function of Ar gas pressure. In this study, the superheated flibe vapour was generated by a high-current, pulsed electrical discharge over a pool of liquid flibe. The excited vapour expanded inside a temperature-controlled chamber, where vapour clearing decay time was evaluated from the measured pressure history. In addition, this information of pressure history inside the chamber is important to design the RTL (recyclable transmission line)/target assembly sequence, including the time required to remove the RTL plug and to insert a new RTL/target assembly.

EXPERIMENTAL SETUP

The experiments were performed in a facility designed to generate an electrical discharge in a vacuum chamber with typical peak currents of 100 kA and periods of 100 μs [3, 4]. Although the mechanism for excited vapour generation (resistive and radiative heating) is different from

Z-pinch chambers, the short time-scale of the generation process ensured that relevant conditions were met. A stagnant pool of flibe was maintained in thermal equilibrium in a vacuum chamber. The pool was contained inside an electrically grounded nickel crucible that functioned as the discharge anode when breakdown occurred. The crucible chamber, shown in Figure 1, used a single high-T gas filled metal seal, allowing for operation up to 700^{o}C in uniform temperature-controlled atmospheric conditions. To minimize HF attack and condensation sinks, sapphire view-ports were used for spectroscopy diagnostics. In addition, a ceramic break was applied to fully insulate the anode during discharge, and a hard-vacuum motion feed with a micrometer was used to measure the liquid level, allowing for voltage breakdown studies as well as discharge characterization. During the shot the electrode was suspended 1 inch over the pool surface. The condensation process was studied mainly by measuring the total pressure of the condensing gas. The chamber was equipped with sensors capable of measuring the pressure at different locations over the wide range characterizing the clearing process. In this study, a piezo-resistive absolute pressure sensor was used to measure the initial pressure peak corresponding to the injection of the superheated vapour. The sensors have a range of 15 psia, with a sensitivity of 26.55 mV/psia. The high resonant frequency and low sensitivity to acceleration allows to record the pressure history with microsecond time resolution and adequate noise suppression. A capacitive manometer with millisecond time resolution was used simultaneously to measure the base and the final pressure of residual gases. A steady-state residual gas analyzer was used to evaluate the composition of non-condensable impurities. Furthermore, the chamber was designed with insulated ports to allow a secondary anode connection for an exploding ferritic steel wire set-up.

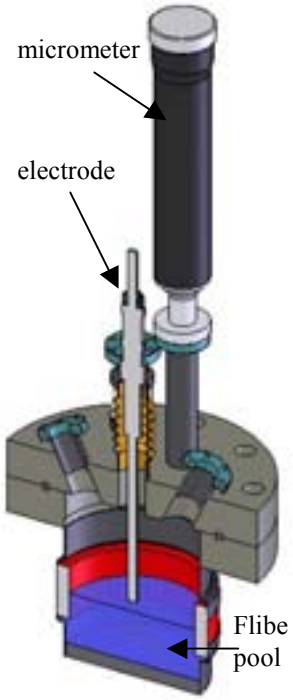

Figure 1. Schematic view of a simulated flibe chamber for a vapour condensation study.

The current set-up is an improved design based on previous experiments on Heavy Ion Beam IFE power plant studies. The previous set-up had been correctly scaling the initial vapour density peak, but the surface area per unit mass had been about 10 times higher than the

scaling suggested. Moreover, the main condensing surface available had been the solid wall of the stainless steel chamber, since the liquid pool from which the vapour was generated had been contained in a small (12 mm diameter) nickel crucible. The current set-up has a larger liquid area in contact with the generated vapour (95.25 mm diameter) and a smaller surface-to-volume ratio and is therefore better reproducing the thick liquid wall chamber conditions of HIF and Z-pinch IFE power plants. The faster condensation rates extrapolated from the measured data in the current set-up are also attributed to the presence of a larger liquid surface, as the dominant condensation mechanism is now the prototypical one of superheated vapour in contact with its own liquid phase.

Sample results of the pressure decay curves for different initial argon gas pressures are presented in Figure 2, where the chamber is kept at 600°C. It is shown that the presence of argon gas does indeed have the effect of slowing down the condensation process because of the formation of a non-condensable buffer above the liquid surface. The buffer forms under hydro-dynamic equilibrium conditions, typically after a period comparable to that of the high current discharge (200 μs). As a result, the pressure decay is characterized by a fast initial phase with high condensation rates, followed by a slower equilibrium phase that depends on the amount of non-condensable gas present. Raw data from the pressure sensor show a significant amount of superimposed ringing noise. This may be either a spurious capacitive effect in the electrical circuit of the piezo sensor or a mechanical vibration of the sensor caused by the initial pressure front.

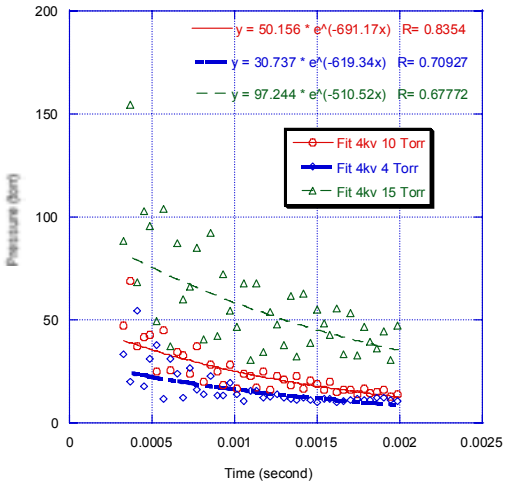

Figure 2. Data fit of pressure decay curves.

RESULTS AND DISCUSSIONS

The analog data from the sensor have been smoothed by numerical interpolation and exponentially fitted. Examples of best exponential fits for three different pressure decay curves are shown in figure 2. The effect of argon gas pressure on the vapour condensation rate is quantified by the exponential decay time defined as:

$$\tau = \ln\left(\frac{P_{res}}{P*}\right)/\lambda \qquad (2)$$

where P_{res} is the residual pressure found in the chamber when equilibrium is reached, and P^* is the best fit peak pressure from the shot. The decay time as a function of residual argon gas pressure is plotted in Figure 3. As shown, the exponential decay time increases from 2.65 ms

to 4.01 ms as argon gas pressures vary from 2 to 20 torr. The decay time increases by about 60% as gas pressure increases from zero to 20 torr. It is also noted that the exponential decay time for the current set-up is about one order of magnitude faster than the data previously obtained, which were designed to simulate the HYLIFE liquid wall concepts. This is probably due to the larger liquid surface available for condensation in the improved experimental set-up described above (about a factor of 50 compared to the previous studies), which may also be one order of magnitude larger than the surface area available for the thick liquid wall concept adopted for the Z-pinch chamber. In future experiments the geometric design of the chamber should take the scaling criterion into consideration.

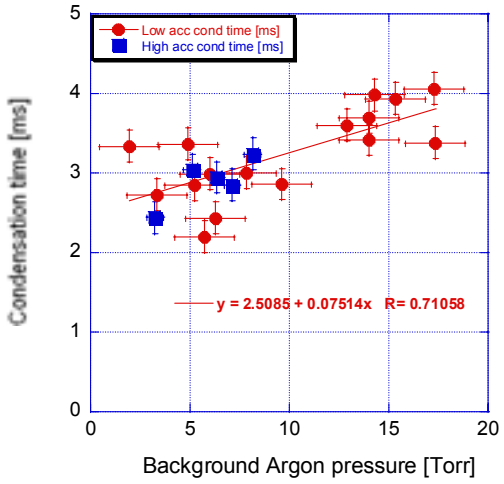

Figure 3. Flibe vapour condensation time as a function of argon gas background pressure.

ANALYSIS

A simple numerical analysis was performed to cross-check the results of the experiments. The numerically derived correlation, which estimates the amount of vapour condensing flux in the presence of a non-condensable gas, coupled with the simultaneously solved ideal gas law and the vapor energy conservation equation, was to estimate the pressure decay characteristics in a zero-dimensional chamber. The correlation written below [5]:

$$j = \frac{1.67}{(2\pi R_v T_v)^{1/2}} \left(P_v - 0.579\ P_{gas} \frac{M_{gas}}{M_v} - P_I \right) \left(1 + 0.515\ \ln \frac{P_v}{P_I} \left(\frac{T_I}{T_v} \right)^{1/2} \right) \left(1 + 4.3 \left(\frac{P_{gas}}{P_I} \right)^{0.52} \left(\frac{M_{gas}}{M_v} \right)^{0.74} \left(\frac{T_I}{T_v} \right)^{4.712} \right)^{-1} \quad (3)$$

explicitly shows that the presence of a non-condensable gas reduces the condensing flux. In addition, its effect magnifies with the heavier molecular weight of the non-condensable gas. The calculated pressure decay evolutions for different argon gas pressures shown in Figure 4 reflect the experimental observations: namely, that vapour condensation has been hindered by

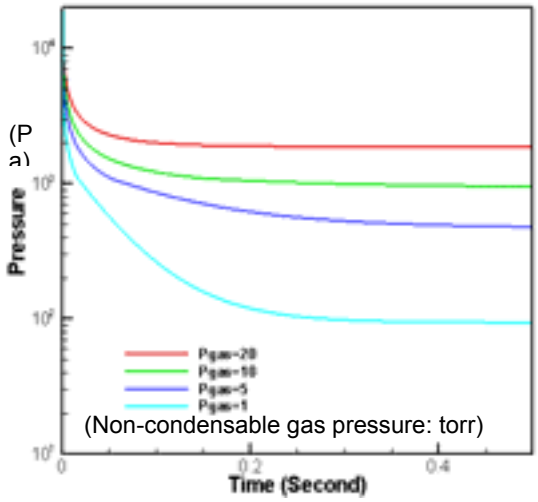

Figure 4. Pressure evolution curves for different argon gas pressures.

the presence of non-condensable gas, while the high amount of non-condensable gas (or higher gas pressure) leads to a much slower vapour condensation. It is noted that the calculated vapour condensation is much slower than the present analytical method in which the hydro-dynamic effect is ignored. These calculations use the saturated pressure of flibe at 600^{o}C for interface conditions.

It is noted that equation 3 gives a negative condensing flux as the vapour pressure decreases to the following value:

$$P_v^c = 0.579 P_{gas} \frac{M_{gas}}{M_v} \qquad (4)$$

In addition, the condensing flux becomes extremely small as vapour pressure approaches its background gas pressure. According to the analysis, this phenomenon saturates at a gas pressure of about 5 torr. A further increase in background gas pressure does not change condensation characteristics significantly. The analysis shows that the vapour pressure drops to the pressure value equal to equation 4 at about 0.2 seconds.

Table 1. Comparison of key design parameters for Z-Pinch and HYLIFE-II concepts

	Z-Pinch	HYLIFE-II
Target yield, MJ	3000	353
Pulse rate, Hz	**0.1**	6.4
X-ray energy (16 % of yield)	480 MJ[1]	56 MJ
Thick liquid chamber material	$(LiF)_2BeF_2$	$(LiF)_2BeF_2$
Amount of vapour generated	120 kg[1]	14 kg
Volume of vapour expansion	< 523 m^3 (spherical chamber with radius= 5 m)	280 m^3
X-ray + debris energy	951 MJ scaled with HYLIFE-II[1]	112 MJ

[1] caled from HIF

SUMMARY

Experiments have been performed to study the vapour condensation characteristics relevant to Z-Pinch conditions, in which a buffer gas of non-condensable argon is applied in a thick liquid chamber for shock mitigation. The results of the experiments, together with a simple analytical estimation, verify that the presence of argon gas does impact the condensation rate, while flibe vapour condensation slows down by about 60% when argon gas pressure increases from zero to 20 torr. These initial results show that there appears to be a large design window for Z-pinch vapour clearing even in the presence of an argon gas pressure of 20 torr.

ACKNOWLEDGEMENT

This work was supported by the SNL Z-Pinch IFE Programme under Contract Number 316984/RFQ 6790.

REFERENCES

[1] W.R. MEIER, R.W. MOIR, M.A. ABDOU, Chamber technology concepts for inertial fusion energy, three recent examples, UCRL-JC-125147, March 1997.
[2] C.L. OLSON, Z-Pinch Inertial Fusion Energy, in the Landolt-Boernstein Handbook on Energy Technologies, Vol. VIII/3, Springer-Verlag (2004).
[3] P. CALDERONI, A. YING, T. SKETCHLEY, M.A. ABDOU, Fusion Technology, 39 N.2 (2001) 711.
[4] P. CALDERONI, UCLA PhD Thesis, 2004.
[5] L. PONG, G.A. MOSES, Vapor condensation in the presence of a noncondensable gas, Phys. Fluids Vol. 29 No. 6, 1796 (1986).

LIST OF PARTICIPANTS

Foldes, I.	KFKI - Research Institute for Particle and Nuclear Physics, P.O. Box 49, H-1525 Budapest, Hungary foldes@rmki.kfki.hu
Hoffmann, D.	GSI - Darmstadt, Planckstr. 10, D-6429 Darmstadt, Germany d.hoffmann@gsi.de
Izawa, Y.	Institute of Laser Engineering, Osaka University, 2-6 Yamada-oka, Suita, Osaka 565-0871, Japan izawa@ile.osaka-u.ac.jp
Kalal, M.	Faculty of Nuclear Sciences and Physical Engineering, Czech Technical University in Prague, Brehova 7, 115 19 Prague 1, Czech Republic kalal@fjfi.cvut.cz
Kasuya, K.	Department of Energy Sciences, Tokyo Institute of Technology, 4259 Nagatsuta, Midori-ku, Yokohama, Kanagawa, G3-35, 226-8502, Japan kkasuya@es.titech.ac.jp
Kato, H.	Faculty of Engineering, Gifu University, 1-1 Yanagido, Gifu 501-1193, Japan i3135009@guedu.cc.gifu-u.ac.jp
Kawashima, T.	Institute of Laser Engineering, Osaka University, 2-6 Yamada-oka, Suita, Osaka 565-0871, Japan kawasima@ile.osaka-u.ac.jp
Khaydarov, R.	Institute of Applied Physics, National University of Uzbekistan, 700206, Yunis-Obod, 14-39-26, Tashkent, Uzbekistan rkhaydarov@nuuz.uzsci.net; ragab@iaph.tkt.uz
Kong, H.J.	Dept. of Physics, KAIST, Gusong-dong, Yusong-gu, Daejon, Republic of Korea 305-701 hjkong@kaist.ac.kr

Koresheva, E.R. P.N.Lebedev Physical Institute,
53 Leninskiy Prospect, 119991 Moscow, Russian Federation
koresh@sci.lebedev.ru

Lee, B.-J. Korea Basic Science Institute (KBSI),
52 Yeoeun-dong, Yuseong-gu, Daejon, 305-333,
Republic of Korea,
bjlee@kbsi.re.kr

Lee, S.-K. Korea Advanced Institute of Science and Technology (KAIST),
Kusong-dong, Yusong-gu, Daejon,
Republic of Korea 305-701
lsk@kaist.ac.kr

Lim, C. Korea Atomic Energy Research Institute (KAERI),
150, Dukjin-dong, Yuseong-ku, Daejon,
Republic of Korea
chlim@kaeri.re.kr

Mank, G. International Atomic Energy Agency,
POB 100, A-1400 Vienna, Austria
g.mank@iaea.org

Matsumoto, O. Institute of Laser Engineering,
Osaka University,
2-6, Yamada-oka, Suita, Osaka, 565-0871, Japan
omatsumo@ile.osaka-u.ac.jp

Meier, W.R. Fusion Energy Program, Lawrence Livermore National Lab,
P.O. Box 808, L-641, Livermore, CA 94551,
United States of America
meier5@llnl.gov

Nakai, S. Kochi National College of Technology,
Monobe 200-1, Nankoku-city, Koichi 783-8508, Japan
pnakai@jm.kochi-ct.ac.jp

Norimatsu, T. Institute of Laser Engineering,
Osaka University,
2-6 Yamada-oka, Suita, Osaka 565-0871, Japan
norimats@ile.osaka-u.ac.jp

Perlado, J.M. DENIM UPM Escuela Tecnica Superior Ingenieros Industriales,
Jose Guterrez Abascal, 2 Madrid 28006, Spain
mperlado@din.upm.es

Rudraiah, N. National Research Institute for Applied Mathematics (NRIAM),
492/G,
7th Cross, 7th Block (West) Jayanagar, Bangalore – 560070,
India
rudraiahn@hotmail.com

Sharkov, B.Y.	ITEP – B Cheremunshkinshaya 25, 117218 Moscow, Russian Federation Boris.Sharkov@itep.ru
Skoric, M.M.	VINCA Institute of Nuclear Sciences, P.O. Box 522, 11001 Belgrade, Serbia and Montenegro mskoric@vin.bg.ac.yu
Tillack, M.S.	University of California San Diego, La Jolla, California, United States of America
Tomioka, H.	Faculty of Engineering, Gifu University, 1-1 Yanagido, Gifu 501-1194, Japan Hiromasa_Tomioka@hotmail.com
Wolowski, J.	Head of Laser-Produced Plasma Department, Institute of Plasma Physics and Laser Microfusion, Hery St. 23, P.O. Box 49, 00-908 Warsaw, Poland wolowski@ifpilm.waw.pl
Yamahira, Y.	Faculty of Engineering, Gifu University, 1-1 Yanagido, Gifu 501-1193, Japan i3135038@guedu.cc.gifu-u.ac.jp
Ying, A.	UCLA, Engineering IV, Room 44-114, Los Angeles, CA 90095-1597, United States of America ying@fusion.ucla.edu
Yoo, B.	Korea Atomic Energy Research Institute (KAERI), 150, Dukjin-dong, Yuseong-ku, Daejon, Republic of Korea bdyoo@kaeri.re.kr
Yoshida, H.	Faculty of Engineering, Gifu University, 1-1 Yanagido, Gifu 501-1193, Japan hiroki@cc.gifu-u.ac.jp